Feb 2022
PhD Dissertation

Study on mechanisms of coherent control of electromagnetically induced absorption and transparency depending on neighboring hyperfine lines, multiphoton mixings, and polarizations in coupling-probe experiment using D2 lines of Rb atoms.

Graduate School of Chosun University

Department of Photonic Engineering

Zeeshan Ali Safdar Jadoon

Study on mechanisms of coherent control of electromagnetically induced absorption and transparency depending on neighboring hyperfine lines, multiphoton mixings, and polarizations in coupling-probe experiment using D2 lines of Rb atoms.

루비듐 원자의 D2 전이선을 이용한 커플링-프로브 실험에서 이웃전이선, 다광자 혼합 효과, 편광에 따른 전자기 유도 흡수 및 투과 형성의 결맞음 조절 원리 규명에 대한 연구

February 25, 2022

Graduate School of Chosun University

Department of Photonic Engineering

Zeeshan Ali Safdar Jadoon

Study on mechanisms of coherent control of electromagnetically induced absorption and transparency depending on neighboring hyperfine lines, multiphoton mixings, and polarizations in coupling-probe experiment using D2 lines of Rb atoms.

Advisor: Jin-Tae, Kim

A dissertation submitted in partial fulfillment of the requirements
for the Degree of Doctor of Philosophy

October, 2021

Graduate School of Chosun University

Department of Photonic Engineering

Zeeshan Ali Safdar Jadoon

This is to certify that the PhD thesis of **Zeeshan Ali Safdar Jadoon** has successfully met the dissertion requirements of Chosun University.

Chairman (Chosun University): Prof. Jong-Rak Park	
Member (Chosun University): Prof. Jin-Tae Kim	
Member (Chosun University): Prof. Hyun Su Kim	
Member (Chosun University): Prof. Tae-Jung Ahn	
Member (Chonnam University): Prof. Heung-Ryoul Noh	

December, 2021

Graduate School of Chosun University

Department of Photonic Engineering

Abstract

Study on mechanisms of coherent control of electromagnetically induced absorption and transparency depending on neighboring hyperfine lines, multiphoton mixings, and polarizations in coupling-probe experiment using D2 lines of Rb atoms.

Zeeshan Ali Safdar Jadoon

Advisor: Prof. Jin-Tae Kim

Department of Photonic Engineering

Graduate School of Chosun University

This thesis studies the coherent response of a degenerate two-level atomic system (DTLS). Specifically, we focus on electromagnetically induced absorption (EIA) and electromagnetically induced transparency (EIT) resonances with sub-natural linewidth associated with the coherent interaction of coupling and probe light fields in a coupling-probe spectroscopy configuration. The main results concern the experimental measurement and theoretical absorption calculation of rubidium (Rb) D2 transition lines confined in an atomic vapor cell at room temperature (20°C).

First, we present experimental and theoretical verification of the higher-order multiphoton oscillation frequency mixing dependence on the choice of quantum axis selected as the propagation direction of co-propagating coupling and probe laser beams and coupling powers. We confirm distinct spectral differences between 3PI and 5PI calculations due to variations in the magnetic field and coupling power compared to the experiment.

Second, we show that in unresolved atomic systems such as ^{85,87}Rb, neighboring hyperfine states play an inevitable role in enhancement or reduction of the coherent effects due to Doppler broadening, which causes the transition between EIA and EIT. We observe the EIA phenomenon in the open DTLS with the weak coupling power for the first time. In addition, we confirm that the observed absorption spectra at the open DTLS with the intense coupling beam are not the actual EIA but are an effect of the high power. Optical Bloch equations (OBE) in the challenging case of ^{85}Rb D2 transition lines that involve the Doppler broadening effects are solved with and without considering neighboring hyperfine states near the DTLS.

Third, we demonstrate theoretical and experimental verification of a simple method to coherently control the EIA and EIT resonances in unresolved ^{85,87}Rb atomic systems by controlling the polarization of coupling and probe laser fields in coupling-probe spectroscopy configuration. Observed EIAs at both closed and open transitions of ^{87}Rb and ^{85}Rb D2 lines atomic systems can transform to EITs and vice versa by controlling the polarization of coupling and probe beams in the low coupling-probe power regime. The transformations are determined to be the effect of neighboring hyperfine levels by comparing the measured and theoretically calculated spectra considering Doppler broadening effects due to neighboring hyperfine states in OBEs.

Single external cavity diode laser combined with two acousto-optic modulators produces the experiments' coupling and probe laser beams. Hence, the scanning resolution of AOM determines the spectral resolution of the coherent EIA and EIT spectra, which gives an accurate match between the theory and experiment.

Index Terms: DTLS, EIA, EIT, D2 lines, rubidium atoms, coupling-probe spectroscopy, Doppler broadening

초록

루비듐 원자의 D2 전이선을 이용한 커플링-프로브 실험에서 이웃전이선, 다광자 혼합 효과, 편광에 따른 전자기 유도 흡수 및 투과 형성의 결맞음 조절 원리 규명에 대한 연구

즈산 알리 사프다 자드온

지도교수: 김진태 교수

광기술공학과

조선대학교 대학원

본 논문에서는 축퇴된 이준위 원자 시스템에서 결맞음 반응을 연구한다. 특별히 커플링-분광학 구도에서 커플링 및 프로브 빔의 결맞음 상호 작용으로 인한 자연 선폭 이하의 분해능을 가진 전자기 유도 흡수와 전자기 유도 투과에 대해 초점을 둔다. 주요한 연구결과들은 상온(20°C)에서 원자 증기 셀에 있는 루비듐 D2 전이선들의 실험 측정 및 이론 계산 결과에 관심을 가진다.

첫째, 같은 방향으로 진행하는 커플링 및 프로브 빔들의 방향으로 양자 축을 선택 시 5차 이상의 고차 다광자 진동 주파수 혼합이 있음을 이론적, 실험적인 증명을 보여준다.

둘째로 ^{85,87}Rb 와 같은 분해되지 않은 원자 시스템에서 도플러 확장에 기인한 이웃 전이선들이 결맞음 효과들의 감소 혹은 증대에 분명한 역할을 하며, EIA 와 EIT 사이의 변환을 야기시킨다. 열린 DTLS에서 약한 커플링 파워에 EIA 현상을 처음으로 관찰하였다. 뿐만 아니라 강한 커플링 빔을 가지고 열린 DTLS에서 관찰된 흡수 스펙트라는 실제 EIA 가 아니고, 강한 파워 효과임을 확인하였다. 도플러 확장 효과를 포함하는 ^{85}Rb D2전이선의 도전할만한 경우로 광블로흐 방정식이 DTLS 근처에 있는 이웃초미세 구조를 고려하고, 고려하지 않은 경우에 대한 해를 구했다.

셋째로, 커플링-프로브 분광학 구도에서 커플링 및 프로브 빔의 편광을 조절함에 의해 분해되지 않은 ^{85,87}Rb 원자 시스템에서 EIA 와 EIT를 결맞게 조절할 수 있는 단순한 방법을 이론적 및 실험적으로 보였다. ^{87}Rb 과 ^{85}Rb D2의 원자 전이선에서 약한 커플링-프로브 영역에서 커플링 및 프로브 빔의 편광을 조절하여 닫힌 혹은 열린계에서 관찰된 EIA는 EIT로 변환이 가능하고 반대로 EIT는 EIA로 변환되게 할 수 있다. 그러한 변환들은 광학 블로흐 방정식에서 이웃 초미세 구조 상태를 삽입하여 도플러 확장 효과를 고려한 측정된 신호와 이론적으로 계산된 스펙트라를 비교하여 이웃 초미세 구조의 영향인 것으로 확정되어졌다.

단일 외부 공진기형 다이오드 레이저와 두개의 AOM을 결합하여 실험에서 커플링, 프로브 빔을 생성하였다. 그래서 EIA와 EIT의 스펙트럴 분해능은 AOM 스캔 분해능으로 결정되며 이론과 실험을 매우 정확하게 비교를 줄 수 있게 하였다.

Index Terms: DTLS, EIA, EIT, D2 lines, rubidium atoms, coupling-probe spectroscopy, Doppler broadening

Acronyms

AOM	Acoustic Optic Modulator
ATS	Autler-Towns Splitting
BS	Beam Splitter
DTLS	Degenerate Two-Level System
EIA	Electromagnetically Induced Absorption
EIT	Electromagnetically Induced Transparency
HWP	Half-Wave Plate
kHz	Kilo Hertz
LMF	Longitudinal Magnetic Field
MHz	Mega Hertz
NDF	Neutral Density Filter
OBE	Optical Bloch Equations
OI	Optical Isolator
PBS	Polarizing Beam Splitter
PD	Photo Diode
QWP	Quater-Wave Plate
Rb	Rubidium
RWA	Rotating Wave Approximation
SAS	Saturation Absorption Spectroscopy
TOC	Transfer of Coherence
TOP	Transfer of Population
W	Window
3PI	Three-Photon Interactions
5PI	Five-Photon Interactions

Contents

List of Figures

Chapter 1
Introduction

Coherent light-matter interaction is of great interest to the scientific community across a wide range of disciplines. On the atomic scale, quantum coherence between the coupled atomic states continues to be the focus of substantial research due to the variety of novel properties they exhibit. These resonant atomic systems are well known to modify the absorption and dispersion of light field propagation, which have been shown to manifest exciting phenomena such as electromagnetically induced absorption (EIA) [1, 2] and electromagnetically induced transparency (EIT) [3, 4]. Even though many studies devoted to the EIA and EIT resonances in a coherent atomic media enormously advanced our understanding, a clear quantitative understanding of the phenomena was not revealed through systematic experimental or theoretical studies considering a broad range of physical factors. For example, theoretically predicted sign(type) of coherent EIA or EIT resonance was successfully observed experimentally in several investigations. However, in many other cases, experimental spectra revealed the different sign of EIA or EIT resonance that was subsequently explained theoretically.

Moreover, qualitative theoretical predictions adopted by different researchers differed significantly. Thus, the origins of EIA and EIT resonances and mechanisms to coherently control these resonances in realistic atomic systems remain still unclear. Understanding these phenomena requires detailed studies where experimental measurements can be compared to the theoretical calculations based on realistic test systems.

This thesis presents a systematic approach to address such questions. The main results concern the experimental study on D2 lines of ^{85}Rb and ^{87}Rb atoms confined in a reference vapor cell at room temperature (20°C). Coupling-probe spectroscopy configuration is utilized to probe essential spectroscopic features. Physical observables such as probe absorption, three-photon interaction (3PI), five-photon interaction (5PI), Doppler broadening, and effects due to neighboring hyperfine states are studied theoretically as a function of physical parameters such as external magnetic field, coupling and probe power ratio, polarization, and atomic level characteristics to obtain the coherent control of these resonances in the realistic test systems.

1.1 Motivation

Both EIA and EIT are sub-natural width resonances that can alter the response of resonant absorption in amplitude and phase to produce large dispersion, which attracts great attention for applications in lasing without inversion [5], high-resolution spectroscopy [6], precision magnetometry [7–9], enhancement of refractive index [10], optical modulation [11], slow and fast light generation [12], optical switching [13], and quantum information science [14–19]. EIA can be invoked by constructive quantum interference of multiple excitation pathways in a resonant atomic media, while EIT results from destructive quantum interference between different excitation pathways in a resonant atomic media.

In order to exploit EIA or EIT resonances in a realistic atomic system, coherence between atomic states is often created using two laser fields and their relative frequencies with a strong coupling and weak probe in a coupling-probe configuration. Where ultra-narrow features at the line center of the probe absorption spectra are characterized by a sharp dip (EIA) or a peak (EIT) when coupling and probe fields have equal frequencies. These resonances can also be observed in a Hanle configuration where two orthogonal circular polarization components of a single linearly polarized laser field are subjected to the applied magnetic field along the wave vector, creating level-crossing resonances by shifting the energies of the degenerate magnetic sublevels of a ground state.

One of the primary methods to study the response of the atomic media, which in most experiments is an atomic vapor, is to measure the probe absorption spectra in the weak limit of the probe field. Therefore, an experiment using a coupling-probe configuration instead of Hanle type experimental configuration is more suitable because the power ratios between coupling and probe fields can be obtained in addition to a wide scanning frequency range. Furthermore, the coupling and probe fields generated using a single laser source combined with two acoustic-optic modulators can limit the decoherence rate because of transit time relaxation between the ground state Zeeman sublevels.

Usually, DTLS are theoretically considered to explain EIA and EIT resonances because DTLS can provide the possibility to analyze different level schemes (Λ, V, and N) by appropriate choice of angular momenta of atomic levels and the polarization of coupling and probe fields. The choice of quantum axis selection rule remains arbitrary in the case of orthogonal linear polarizations of coupling and probe fields. Either the coupling or probe field can be employed parallel to the direction of a quantum axis. However, the quantum axis selection rule is well defined by applying an external magnetic field in a longitudinal direction resulting in the mixture of left and right circular polarization components of initially orthogonal linear polarizations of coupling and probe fields, both exciting the same hyperfine magnetic sublevels.

Due to coherent multiphoton interactions between coupling and probe fields acting on the same hyperfine magnetic sublevels, different oscillation frequency mixings effects can be observed. However, coherent multiphoton interactions greater than three-photon interactions (3PIs) between coupling and probe fields acting on the same hyperfine magnetic sublevels are not considered to date. Nevertheless, precise coherent spectra due to the contribution of higher-order multiphoton interactions at high-intensity coupling and probe fields acting on the same hyperfine transitions motivate to investigate the coherent multiphoton oscillations greater than 3PIs. Further, selecting the quantum axis in the direction of an applied longitudinal magnetic field simplifies the OBEs calculation.

Additional motivation arises to investigate mechanisms of transformation between EIA and EIT resonances that are still unclear. Although theoretical calculations based on a pure DTLS have proven to model many experimental results accurately, pure DTLS are seldom found in real atomic systems. Specifically, in the case of ^{85}Rb and ^{87}Rb atomic systems, the separation between individual hyperfine F levels is shorter than the Doppler width; hence these systems are unresolved under the Doppler broadening effects.

Solving the OBEs by considering the Doppler broadening effects, including all neighboring hyperfine levels, has proven to be particularly challenging. Therefore, it is worth studying the Doppler broadening effects at hyperfine D2 transitions of ^{85}Rb and ^{87}Rb atoms by including all neighboring hyperfine levels near the resonant DTLS considering the transition openness, variation of coupling and probe power ratios, and polarization configurations. Subsequently, the transformation between EIA and EIT resonances considering atomic-level schemes, coupling-probe power ratios, and polarization configuration should be studied to obtain coherent control of these resonances in real atomic systems.

1.2 Organization of the thesis

The remaining thesis is organized as follows:

- **i) Chapter 2** presents an overview of the related published work. Main research questions and research objectives are presented systematically.
- **ii) Chapter 3** covers the basic theoretical model for idealized two-level, three-level, and four-level atomic systems, which forms the basis for theoretical models expanded in the later chapters to cover the additional complexities.
- **iii) Chapter 4** explores the higher-order multi-photon frequency mixing effects on the coherent EIA spectra. Detail overview of the experimental and theoretical results is presented.
- **iv) Chapter 5** extends the DTLS by including additional neighboring hyperfine states. The analysis compares a pure DTLS and all neighboring states near the DTLS with the experimental measurements.
- **v) Chapter 6** aims to address the role of neighboring hyperfine states to control the EIA and EIT resonances. Polarization configurations of the coupling and probe fields are analyzed to control the sign of the resonances effectively.

vi) **Chapter 7** highlights conclusions and briefly describes the limitations of this research work and future directions.

1.3 Publications Arising from these Works

1. Z. A. S. Jadoon, H.-R. Noh, and J. T. Kim, Multiphoton nonlinear frequency mixing effects on the coherent electromagnetically induced absorption spectra of ^{85}Rb atoms under a longitudinal magnetic field: Theory and experiment, Phys. Rev A **102**, 063714 (2020).

2. Z. A. S. Jadoon, H.-R. Noh, and J. T. Kim, (Accepted) Scientific Reports (2021).

3. Z. A. S. Jadoon, Aisar-ul Hassan, H.-R. Noh, and J. T. Kim, To be submitted in Optics Express Journal (2021).

Chapter 2

Literature Review

2.1 Overview

This chapter presents a systematic review of the subjects of this thesis in chronological order to establish a reasonable perspective of the coherent EIT and EIA phenomena in the existing literature. It provides an overview of theoretical and experimental developments and understanding of underlying physics for various manifestations. These include the effects of multiphoton interactions on the resonant EIA spectra, polarization configuration and power ratio between coupling and probe light fields, and the effect of an external magnetic field. Additionally, we highlight the role of neighboring hyperfine levels in the context of Doppler broadening and atomic level characteristics to control the transition between EIA and EIT resonances coherently.

2.2 Multiphoton Oscillation Frequency Mixing

In coupling-probe spectroscopy, the contribution of multiphoton nonlinear frequency mixing effects between coupling and probe laser fields are crucial in calculating coherent spectral profiles accurately [1, 20–37]. Furthermore, different oscillation frequency mixings effects can be observed due to coherent multiphoton interactions between coupling and probe fields acting on the same hyperfine magnetic sublevels. However, coherent multiphoton interactions greater than three-photon interactions (3PIs) between coupling and probe fields acting on the same hyperfine magnetic sublevels are not considered to date.

Coherent spectra from coupling-probe spectroscopy up to 3PIs resulting from four-wave mixing have been investigated extensively utilizing optical density matrix elements in a degenerate two-level system (DTLS) [1, 25–37]. In a simple two-level system with hyperfine or Zeeman reservoir states, ultranarrow antiholes are explained through inelastic collisions and 3PIs in coupling-probe spectroscopy [23]. Subsequently, 3PIs have been investigated theoretically in DTLS to explain the transfer of coherence (TOC) and populations resulting in EIA resonance [26, 27]. Similarly, coherent ultranarrow EIA spectra using a single laser with two acousto-optic modulators (AOMs) have been reported without theoretical analysis. To clarify the observed spectra in [1], 3PIs are utilized to investigate the dependence of polarization of optical fields, coupling-probe power, and magnetic field on the coherent spectra in DTLS [25]. In the case of the weak probe beam Rabi frequency of the probe beam is treated to first-order [1, 25–35].

However, in the case of strong coupling and probe laser fields, few works have been reported considering multiphoton interactions more than 3PIs [36, 37], where each optical density matrix element can be expanded by Fourier series taken to all orders in DTLS. Higher-order photon interactions given by $a_{1_{max}}$ $=F_g + F_e$ in Zeeman coherences with a single frequency in Table I in Ref. [36] for different transitions of magnetic sublevels between an intense σ^+-polarized control beam and a probe beam with either σ^- or π polarization with comparable intensity to the coupling beam is considered. However, authors in [36] could not observe higher-order nonlinear frequency mixings effects such as five-photon interactions (5PIs) with only a single oscillating frequency at higher coupling-probe intensities because both the coupling and probe beams act on different hyperfine transitions instead of the same hyperfine transitions. Authors in Ref. [37] follow similar mathematical formulation given by Eqs. (4)-(8) as in Ref. [36] Eqs. (12)-(16) representing optical Bloch equations (OBEs).

The choice of quantum axis selection rule remains arbitrary in the case of orthogonal linear polarizations of coupling and probe fields. One can employ either the coupling or probe field parallel to the direction of a quantum axis. However, the quantum axis selection rule is well defined by applying an external magnetic field in a longitudinal direction resulting in the mixture of left and right circular polarization components of initially orthogonal linear polarizations of coupling and probe fields, both exciting the same hyperfine magnetic sublevels. Selecting the appropriate quantum axis [22, 32, 36, 38] as the polarization direction of the coupling or probe beam, or in the case of weak coupling beams, 3PIs can be applied to solve OBEs.

Selecting the appropriate quantum axis avoids complex calculations, and experimental spectra with 3PI can be interpreted intuitively in a coupling-probe experiment. 3PIs in a DTLS without an external magnetic field have been reported by Chen *et al.* [22]. Rehman *et al.* [28] observed ultranarrow EIA spectral features owing to population and coherence transfer for the parallel and orthogonal linear polarization configurations utilizing 3PIs, investigated without phenomenological constants and an external magnetic field with the appropriate quantum axis as the polarization direction of the coupling beam.

In addition to intense coupling power in DTLS, external magnetic fields render the calculation of coupling-probe coherent spectra with more than 3PI even more complicated. Therefore, it is convenient to select the quantum axis as the direction of an external longitudinal magnetic field (LMF) as OBEs calculation can be simplified considering symmetric off-diagonal density matrix elements. Previously both transverse and longitudinal magnetic fields were simultaneously applied [24, 38, 39], only transverse [40–43], and only longitudinal magnetic fields were applied to the propagation direction of the co-propagating coupling, and probe lasers [20, 31, 35, 44, 45].

Transverse magnetic field effects in the DTLS have been theoretically investigated by Margalit *et al.* [24]. The authors in Ref. [24] could not realize the higher-order multiphoton frequency mixing effects due to 5PI but realized 3PI effects for the TOC in EIA. They could not realize any difference utilizing 3PIs in OBEs as adopted in their reference (Ref. [35]) even after setting the quantization axis in an arbitrary direction. Similarly, the authors in Ref. [35] realized 3PI effects for the TOC in EIA and could not realize the higher-order multiphoton frequency mixing effects such as 5PI.

In the cases mentioned above, no clear theoretical explanation exists for coherent spectra involving strong coupling powers with 5PIs resulting from six-wave mixing between coupling and probe frequencies.

2.3 Role of Neighboring Hyperfine States

Interest in the coherent phenomenon intensified in the 1990s with the prediction and observation of EIA and EIT resonances [1, 3, 4]. Since the initial reports on EIA and EIT, numerous studies have been conducted on the transitions between EITs and EIAs and the mechanisms of the transitions due to quantum coherence and interference between coupled atomic states both in coupling-probe and Hanle-type experiments [26, 46–60]. However, the mechanisms of transitions between EIAs and EITs depending on powers, polarization configurations of coupling and probe beams, the openness of the transitions, and neighboring effects with Doppler broadening are still unclear [26, 46–60].

The mechanisms of EIA transitions from EITs depending on coupling and probe powers in the case of the $F_e = F_g - 1$ open system of the ^{85}Rb D2 line have not been elucidated, and such EIAs at weak coupling and probe powers have not been observed to date.

Three necessary EIA conditions for EIAs by Lezama [2] for a degenerate two-level system (DTLS) were established based on first investigations of EIA resonance [1] using coupling and probe lasers: (i) the ground state must be degenerate; (ii) $F_e = F_g + 1$; (iii) the $F_g \rightarrow F_e$ transition must be closed. However, contributions to absorption or transmission coherence strength from neighboring states embedded in Doppler broadening profiles, power ratios between the coupling and probe beams, polarization configurations, the openness of the excited state were not considered.

There are many reports on transition between EITs and EIAs [26, 46–48, 50–58, 60] and between EIAs and EITs [49, 51, 52, 59] which are observed and calculated in partially resolved [26, 46–48, 50–53, 55–58, 60, 61] or completely unresolved [59][Our new Ref.] alkali-metal atomic systems.

The transformations between EITs to EIAs, which result from intense coupling and probe powers above saturation limit, are barely enhanced absorptions, observed and calculated by several groups [26, 46, 47, 50, 53–55, 57]. Authors in the Refs. [46, 47] observed EIAs at $F_g \rightarrow F_e = F_g + 1$ open transitions of D1 lines of 85Rb and 87Rb atoms for the first time in Hanle experimental configuration. Goren *et al.* [26] explained such EIAs as a result of a high degree of openness associated with higher excited state degeneracy at $F_e = F_g + 1$ open transitions that lead to the transfer of population (TOP) and hence the TOC resulting in EIA. However, Kim *et al.* [50] observed EIAs at all open transitions of D1 lines of 85Rb and 87Rb atoms in the Hanle experiment at intense coupling and probe powers violating genuine theoretical EIA conditions [2].

These anomalous EIAs are attributed to intense laser power interpreted with the perturbative treatment of probe calculated quantitatively with a crude theoretical model [53]. Similar transformations observed at open $F_g = 4 \rightarrow F_e = 3$ and 4 transitions of D2 lines of Cs in coupling-probe experimental configuration with an additional third laser [55] are attributed to intense coupling powers wherein they referred to Goren *et al.* [26] theoretical analysis [2].

Artificial shifting of the laser field frequency from the center of Doppler broadened spectra to escape the contributions of neighboring level transitions in the intense power regime is also analyzed by several groups [54, 57, 60]. For example, the transition of EIA and EIT is observed by artificially shifting the laser field frequency from the center of Doppler broadened spectra towards the blue end (towards the red end) at D1 and D2 lines of ^{85}Rb and ^{87}Rb atoms both in Hanle and coupling-probe experimental configurations [54]. Similarly, EIA resonances observed at $F_g \rightarrow F_e = F_g + 1$ open transitions of D1 lines of ^{85}Rb and ^{87}Rb atoms with intense coupling and probe laser fields were artificially blue-shifted in frequency from the center of the Doppler broadened spectra to escape the neighboring level transition [57]. However, they could not realize such EIAs in the fluorescence spectra utilizing extremely thin cell [58].

Grewal *et al.* [60] reported on the influence of closed neighboring hyperfine levels with dominant EIA features owing to the increased ellipticities of the polarizations of coupling and probe lasers at the $F_e \leq F_g$ open transitions of D2 lines of ^{87}Rb in the case of the Hanle configuration. However, they could not theoretically explain the absorption profiles because of the computational complexities involved when considering the Doppler effect. Furthermore, performing calculations of the absorption profiles for D2 transitions of ^{85}Rb has been proven to be a particularly challenging task because of neighboring effects due to Doppler profiles, wherein the total absorption of D2 transition lines with the inclusion of the Doppler effect should be calculated with the inclusion of all hyperfine levels of the ground and excited states.

2.4 Transition between EIA and EIT resonances

Polarization configurations of coupling and probe laser fields can modify the optical response of the atomic system, affecting coherent profiles of absorption and transparency, which results in EIA [1, 2, 25] or EIT [3, 4, 62]. Thus, the excitation pathways connected between the magnetic sublevels due to polarization configurations of the two fields control the optical response of the atomic system, which has important applications in the quantum information process. However, the role of neighboring states to control EIT/EIA resonances concerning the polarization of coupling and probe fields at D2 lines of ^{85}Rb and ^{87}Rb atomic systems that are unresolved under Doppler broadening remains theoretically unexplained to date.

Although various techniques developed utilizing Hanle [53, 54, 57, 59–61, 63–65], Bi-Hanle [51, 66–70] and coupling-Probe configurations [40, 42, 50, 54, 71, 72] have been studied to control the transformation between EIA and EIT resonances. Several previous studies are performed without invoking the inevitable neighboring state effects in real atomic systems both in Hanle and coupling-probe configurations [40, 42, 50, 51, 53, 64, 66–72]. Where different laser field configurations and physical factors have been studied for mechanisms of EIA/EIT and their transformations, such as exciting an adjacent transition in V-type [67] or Λ-type excitation schemes [40, 42, 51, 69], copropagating [40, 42, 66, 68, 70, 72] and counterpropagating configurations of the laser fields [51, 67, 69, 72], due to external magnetic field [40, 42, 64], the intensity of laser field/s [50, 53, 57, 59, 67, 68, 71], spatially separated laser fields [66, 67, 70], and ellipticities of the laser field/s [40, 42, 51, 64–70, 72].

The influence of neighboring states has also been previously studied to control the EIA/EIT transformations [54, 59–61, 63][Our new Ref.]. However, the previous studies are limited to broad laser linewidth [61], pure degenerate two-level systems (DTLS) [63], intense laser field [59], artificial detuning [54, 57, 60], excluding Doppler broadening effects [60], and considering only single-polarization cases [54, 59, 61][Our new Ref]. Thus qualitatively explain the observed spectra; however, lack in clear quantitative theoretical explanation for effective control of EIA/EIT transformation by considering all neighboring hyperfine levels with the inclusion of Doppler broadening effects concerning different polarization cases for both ^{87}Rb and ^{85}Rb D2 lines.

Influence of closed $F_g = 3 \rightarrow F_e = 2$ and $F_g = 4 \rightarrow F_e = 5$ hyperfine D2 transition of Cs are observed in Hanle configuration considering linear and circular orthogonal polarizations both in low and high laser power regime [61]. A multilevel theoretical model considering Doppler broadening effects and broad laser linewidth predicts the transformation of EIA into EIT and EITs into EIAs due to the neighboring closed $F_g = 3 \rightarrow F_e = 2$ and $F_g = 4 \rightarrow F_e = 5$ hyperfine transitions, respectively. However, the transformation between the resonances as a function of polarization was not observed and calculated.

Ram et al. [63] studied the ellipticity effects on EIA(EIT) resonances at $F_g = 2 \rightarrow F_e = 3$ and $F_g = 1 \rightarrow F_e = 2$ of D2 line of ^{87}Rb in Hanle experiment both with longitudinal and transverse magnetic field scans. Influence of the nearby closed $F_g = 1 \rightarrow F_e = 0$ hyperfine level transition on the open $F_g = 1 \rightarrow F_e = 2$ transition is theoretically analyzed by comparing pure DTLSs calculations. They also reported transformation of EIA into EIT at a high intensity of coupling field with circular orthogonal polarizations of coupling and probe beams as a function of transverse magnetic field scan in Hanle experiment [68]. Shift in atomic population due to coupling and probe cycles associated with the different Zeeman sublevels in a degenerate two-level system (DTLS) is attributed to explain such EIT peak at the center of the spectra. Closed transitions of ^{85}Rb and ^{87}Rb D2 lines were also investigated as a function of high laser power and temperature of the atomic vapor cell in Hanle configuration to show the transformation from EIAs to EITs [59].

Grewal et al. [60] also observed the transformation from EITs to EIAs at $F_g = 2 \rightarrow F_e = 1$ and 2 open transitions by changing ellipticity of intense light field considering transverse and longitudinal magnetic field scanning in the Hanle configuration. However, they could not calculate the influence of $F_g = 2 \rightarrow F_e = 3$ closed transition by considering the Doppler effect due to computational complexity.

2.5 Outlook

Even though many studies devoted to the EIA and EIT resonances in a coherent atomic media enormously advanced our understanding, however, clear quantitative understanding of the phenomena was not revealed through systematic experimental or theoretical studies considering a broad range of physical factors. For example, theoretically predicted sign of coherent EIA or EIT resonance was successfully observed experimentally in many investigations. However, in many other cases, experimental spectra revealed the different sign of (EIA or EIT) resonance that was subsequently explained theoretically. Moreover, qualitative theoretical predictions adopted by different researchers differed significantly. Thus, the origins of EIA and EIT resonances and mechanisms to coherently control these resonances in real atomic systems remain still unclear. Understanding these phenomena requires detailed studies comparing experimental measurements to theoretical calculations based on realistic test systems. This thesis presents a systematic approach to address such questions. The main results concern the experimental study on D2 lines of ^{85}Rb and ^{87}Rb atoms confined in a reference vapor cell at room temperature (20°C). We utilize coupling-probe spectroscopy configuration to probe the essential spectroscopic features. Physical observables such as probe absorption, 3PI, 5PI, Doppler broadening, and effects due to neighboring hyperfine states are studied theoretically as a function of physical parameters such as external magnetic field, coupling and probe power ratio, polarization, and atomic level characteristics to obtain the coherent control of these resonances in the realistic test systems.

Chapter 3

Fundamental Theoretical Model

3.1 Overview

This chapter introduces a fundamental theoretical model for atom-light interactions that forms the basis of the rest of this work. We will introduce physical principles of atom-light dynamics with application to a basic atomic level schemes. The development of this model by atomic and molecular physics groups at Chosun University and Chonnam National University over the recent years has led to numerous research works [21, 28, 32, 33, 73], and this chapter presents a summary of those. We will expand this model in Chap. 4 to cover the additional complexities of degeneracy and higher-order frequency mixing. Further in Chap. 5, we will include neighboring hyperfine lines near the DTLS. Hence, it is essential to understand the underlying theory of the fundamental atomic level scheme models.

3.2 Two-Level Atomic System

Here we will discuss the atomic system with only two levels, which is the simplest atomic scheme. This case is of great importance because many complex systems can be approximated as two-level systems. In laser and atomic spectroscopy, one of the most fundamental problems is probe beam modification by a coexisting intense coupling beam traversing in an atomic medium [74]. When the coupling and probe beams propagate in the opposite directions, the spectrum obtained using saturated absorption spectroscopy (SAS) directly relates to the imaginary part of the susceptibility. In contrast, modification of the group index is related to the gradient of the real part. SAS (or absorption spectroscopy with bi-frequency) yielding the imaginary part of the susceptibility is the simplest coupling–probe laser spectroscopy that can provide sub-Doppler resolution in a Doppler broadened atomic vapor cell. Thus, we will focus mainly on the imaginary part of susceptibility.

A typical two-level scheme for a two-level atomic system is shown in Fig. 3.1. The ground $|g\rangle$ and excited states $|e\rangle$ are coupled by counterpropagating coupling and probe beams. Where Ω_c (Ω_p) are Rabi frequencies and ω_c (ω_p) are optical frequency of coupling (probe) fields, respectively. The atomic resonance frequency is given as ω_0, the spontaneous decay rate of the excited state is Γ, we assume cycling transition, so there is no decay out of ground state. The decay rate of the first excited state in the case of Rb is $\Gamma \approx 2\pi \times 6$ MHz. The decay rate of optical coherence is defined as γ_t, in the absence of collisional dephasing that is $\gamma_t = \Gamma/2$. Optical frequencies in the rest frame of an atom with velocity v are, $\omega_c = \omega + kv$ and $\omega_p = \omega - kv$, where $k(= 2\pi/\lambda)$ is the wave vector $\lambda(\approx 780\,\text{nm})$ is the wavelength and ω is the laser frequency.

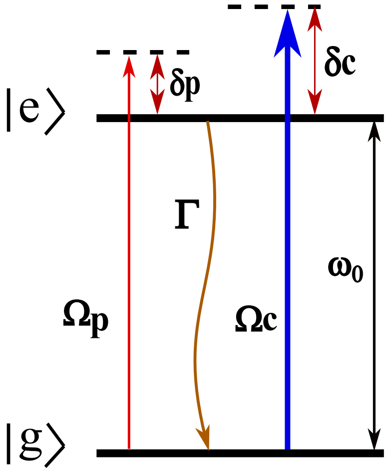

Figure 3.1: Schematic energy-level diagram of the two-level atomic system. The ground $|g\rangle$ and excited states $|e\rangle$ are coupled by counterpropagating coupling and probe beams with angular frequencies ω_c and ω_p, and Rabi frequencies Ω_c and Ω_p, respectively. The detuning of coupling (probe) beam is $\delta_{c(p)} = \omega_{c(p)} - \omega_0$. Spontaneous decay of the excited state is Γ.

The interaction between a two-level system and two optical fields, as shown in Fig. 3.1, is given by

$$H = H_0 + H_i, \tag{3.2.1}$$

where H_0 is the bare atomic Hamiltonian of the system given by

$$H_0 = \hbar \begin{pmatrix} \omega_0 & 0 \\ 0 & 0 \end{pmatrix}. \tag{3.2.2}$$

The Hamiltonian in the dipole approximation due to optical fields is given as

$$H_i = -\hat{\mu}.\varepsilon, \tag{3.2.3}$$

where dipole operator $\hat{\mu} = e\hat{r}$ only has off-diagonal elements, the diagonal terms are $\langle 1|\,\hat{\mu}\,|1\rangle = \langle 2|\,\hat{\mu}\,|2\rangle = 0$ due to the parity of states. The electromagnetic field, ε, for the monochromatic light field can be expressed as

$$\varepsilon = \hat{e}\varepsilon_0 cos(\omega_p t) = \tfrac{\hat{e}\varepsilon_0}{2}(e^{it\omega_p} + e^{-it\omega_p}), \tag{3.2.4}$$

where $\hat{e}$ describes the polarization of the light field. For simplicity, we assume the dipole moment is aligned with the light field, then the components of interaction Hamiltonian considering both probe and coupling fields can be expressed as

$$H_{eg} = H_{ge}^{*} = \tfrac{d_{ge}\varepsilon_0}{2}[(e^{-it\omega_p} + e^{it\omega_p}) + (e^{-it\omega_c} + e^{it\omega_c})]. \tag{3.2.5}$$

The interaction Hamiltonian can therefore be written as

$$H_i = \hbar \begin{pmatrix} 0 & \frac{1}{2}\left(\Omega_c e^{-it\omega_c} + \Omega_p e^{-it\omega_p}\right) \\ \frac{1}{2}\left(\Omega_c e^{it\omega_c} + \Omega_p e^{it\omega_p}\right) & 0 \end{pmatrix}. \tag{3.2.6}$$

The total Hamiltonian of the system without rotation can be rewritten as

$$H = \hbar \begin{pmatrix} \omega_0 & \frac{1}{2}\left(\Omega_c e^{-it\omega_c} + \Omega_p e^{-it\omega_p}\right) \\ \frac{1}{2}\left(\Omega_c e^{it\omega_c} + \Omega_p e^{it\omega_p}\right) & 0 \end{pmatrix}. \tag{3.2.7}$$

Modified hamiltonian in rotating frame $H_{eff} = HUU^{\dagger} - \frac{idUU^{\dagger}}{dt}$ with frequency

ω_c is given as

$$H_{eff} = \hbar \begin{pmatrix} \omega_0 - \omega_c & \frac{\Omega_c}{2} + \frac{1}{2}\Omega_p e^{it\omega_c - it\omega_p} \\ \frac{\Omega_c}{2} + \frac{1}{2}\Omega_p e^{it\omega_p - it\omega_c} & 0 \end{pmatrix}, \tag{3.2.8}$$

where Rotating wave transformation (RWA) matrix U is

$$U = \begin{pmatrix} e^{-it\omega_c} & 0 \\ 0 & 1 \end{pmatrix}. \tag{3.2.9}$$

For simplicity in calculations, effective detunings are defined as $\delta_{p(c)} = \omega_{p(c)} - \omega_0$ and $\delta_d = \delta_p - \delta_c$. Thus effective hamiltonian after rotating wave approximation is

$$H_{eff} = \hbar \begin{pmatrix} -\delta_c & \frac{\Omega_c}{2} + \frac{\Omega_p}{2} e^{-it\delta_d} \\ \frac{\Omega_c}{2} + \frac{\Omega_p}{2} e^{it\delta_d} & 0 \end{pmatrix}. \tag{3.2.10}$$

3.2.1 Time evolution

The time evolution of the two-level system can be calculated from the time dependent Schrödinger equation, which for the density matrix is expressed as

$$\dot{\rho} = -\frac{i}{\hbar}\left[H_{eff}, \rho\right], \tag{3.2.11}$$

which is equivalent to solving Liouville-von Neuman equation. It can be noted that decay in the system e.g due to spontaneous emission are not accounted in Eq. (3.2.11). Therefore, decay is added phenomenologically as a statistical process given by density matrix $\dot{\rho}_{\mathrm{sp}}$, given as

$$\dot{\rho}_{\mathrm{sp}} = \begin{pmatrix} -\Gamma\rho_{ee} & -\gamma_t\rho_{eg} \\ -\gamma_t\rho_{ge} & \Gamma\rho_{ee} \end{pmatrix} \tag{3.2.12}$$

Adding decay term given by Eq. (3.2.12) in the Eq. (3.2.11) results in Linblad master equation, and is expressed as

$$\dot{\rho} = -\frac{i}{\hbar}\left[H_{eff}, \rho\right] + \dot{\rho}_{\mathrm{sp}}, \tag{3.2.13}$$

The density matrix elements are expanded in time to obtain first order susceptibility in $\omega_p(\omega_c)$ expressed as:

$$\begin{aligned} \rho_{eg} &= z_1 + z_2 e^{-it\delta_d} + z_3 e^{it\delta_d}, \\ \rho_{ee} &= q + u e^{-it\delta_d} + u^* e^{it\delta_d}, \\ \rho_{gg} &= p - u e^{-it\delta_d} - u^* e^{it\delta_d}, \end{aligned} \tag{3.2.14}$$

while ρ_{eg}=ρ^*_{ge}. Total population is conserved i.e. $p + q = 1$ as the cycling transition is assumed. Inserting the matrix elements given by Eq. (3.2.14) into the density matrix equation presented by Eq. (3.2.13), following coupled equations for the Fourier components of the density matrix elements are obtained:

$$\dot{z}_1 = i\Delta_1 z_1 + i\Omega_p u^* + \tfrac{i\Omega_c}{2}\left(q - p\right), \tag{3.2.15}$$

$$\dot{z}_2 = i\Delta_2 z_2 + i\Omega_c u^* + \tfrac{i\Omega_p}{2}\left(q - p\right), \tag{3.2.16}$$

$$\dot{z}_3 = i\Delta_3 z_3 + i\Omega_c u^*, \tag{3.2.17}$$

$$\dot{u} = i\Delta_4 u - \tfrac{i\Omega_p}{2} z_1^* + \tfrac{i\Omega_c}{2} z_2 + \tfrac{i\Omega_c}{2} z_3^*, \tag{3.2.18}$$

$$\dot{q} = -\Gamma q - \Omega_p \mathrm{Im}(z_2) - \Omega_c \mathrm{Im}(z_1), \tag{3.2.19}$$

where effective detunings are defined as

$$\begin{aligned}\Delta_1 &= i\gamma_t + \delta_c, \\ \Delta_2 &= i\gamma_t + \delta_c + \delta_d, \\ \Delta_3 &= i\gamma_t + \delta_c - \delta_d, \\ \Delta_4 &= i\Gamma + \delta_d.\end{aligned} \tag{3.2.20}$$

Steady state solution of Eq. (3.2.16) yeilds the susceptibility resposible for probe absorption expressed as

$$z_2 = \frac{i\Omega_p}{2\Delta_2} + \frac{i\Omega_p}{2\Delta_2}(p-q-1) - \frac{i\Omega_c}{\Delta_2}u. \tag{3.2.21}$$

In absence of the coupling laser beam background probe beam is represented by the first term on the right hand side of Eq. (3.2.21), second term represents the hole-burning term obtained by subtracting background term, and the coherence due to coupling beam is given by the last term. Solving Eqs. (3.2.15)-(3.2.19) in steady state regime, population difference $p-q$ and u can be obtained as

$$p-q = \frac{\delta_c^2+\gamma_t^2}{\delta_c^2+\gamma_t^2+\gamma_t\ \Omega_c^2/\Gamma} \tag{3.2.22}$$

$$\begin{gathered}u = \frac{(\delta_d+2\mathrm{i}\gamma_t)(\delta_c+\delta_d\text{-}\mathrm{i}\gamma_t)\Omega_p\Omega_c}{4(\delta_c\text{-}\ i\gamma_t)} \times (p-q) \\ \times \left[(\delta_d\text{-}\ i\Gamma)(\delta_c+\ \delta_d+\ i\gamma_t)(\delta_c\text{-}\ \delta_d\text{-}\ i\gamma_t) + (\delta_d+\ i\gamma_t)\Omega_c^2\right]^{-1}\end{gathered} \tag{3.2.23}$$

3.2.2 Electric Susceptibility

Complex electric susceptibility χ describes how the medium polarises in response to an applied laser field. The individual electric dipole moments of the atoms are related to macroscopic polarization of the medium. The average dipole moment for an ensemble is obtained as

$$P = N\langle\hat{\mu}\rangle = N\mu_{eg}\left[\rho_{eg}e^{-it\omega_p} + \rho_{ge}e^{it\omega_p}\right], \tag{3.2.24}$$

where N is the atomic density. Complex linear susceptibility is related to polarization by

$$P = (\varepsilon - \varepsilon_0)E = \varepsilon_0\chi E \tag{3.2.25}$$

$$P = \tfrac{\varepsilon_0 E_0}{2}\left[\chi e^{-it\omega_p} + \chi^* e^{it\omega_p}\right], \tag{3.2.26}$$

assuming E_0 is real. Combing Eqs. (3.2.24) and (3.2.26) and taking the dot product with μ_{eg}, yields

$$N\mu_{eg}^2\left[\tilde{\rho_{eg}}e^{-it\omega_p} + \tilde{\rho_{ge}}e^{it\omega_p}\right] = -\tfrac{1}{2}\varepsilon_0\hbar\Omega_p\left[\chi e^{-it\omega_p} + \chi^* e^{it\omega_p}\right]. \tag{3.2.27}$$

Relationship between the coherence term in the density matrix given in Eq. (3.2.16) and susceptibility can be found by

$$\chi = -\tfrac{2N\mu_{eg}^2}{\varepsilon_0\hbar\Omega_p}z_2. \tag{3.2.28}$$

In the weak probe limit i.e. $\Omega_p << \Gamma$ and assuming all the population remains in the ground state (ρ_{gg}-$\rho_{ee} \approx 1$), we can obtain the susceptibility as a function of laser detuning. Considering Eq. (3.2.16), the susceptibility can be decomposed into three parts:

$$\chi = \chi_0 + \chi_1 + \chi_2, \tag{3.2.29}$$

where χ_0 is the background term in absence of coupling laser, χ_1 resulting from the hole burning term $(p - q - 1)$, and χ_1 is the coherence term resulting from u.

3.2.3 Doppler Effect

Until here, only stationary atoms are considered, however at room temperature, the atoms have thermal velocity v, which has a typical value of 250 m/s. Therefore the frequency of the absorbed light by the atom is Doppler shifted relative to the velocity of the moving atom, given as

$$\delta_D = -\mathbf{k}.\mathbf{v} = -kv_z, \tag{3.2.30}$$

where **k** is the wave-vector of the incoming monochromatic light field taken along z-axis. It can be noted that there is a shift in frequency only when there is a velocity component in the axis of the beam v_z. However, atomic velocities are distributed in all directions, so the range of velocities are resonantly interacting with the light field. A Maxwellian distribution is assumed along the axis of the light field for the atomic density of a given velocity class $N(v)$ expressed as

$$N(v) = \frac{N_0}{v_{mp}} e^{-(\frac{v}{v_{mp}})^2} \tag{3.2.31}$$

with the most probable speed v_{mp} $(= \sqrt{2k_b T/m})$, m is the mass of the atoms and T is the absolute temperature of the cell. The z subscript is dropped since we are dealing only with one dimension. For a blue detuned laser, atoms moving away are Doppler shifted back onto resonance and thus absorb the light, and similar is the case with atoms moving into the red detuned laser beam. Thus, wherever δ+kv=0, the resonance condition is fulfilled, the result is an inhomogeneously broadened absorption spectral line. Which in the case of hot atoms is larger than the natural linewidth, placing a limit on the spectral resolution. Considering the case of ^{85}Rb atoms, the Doppler width is $\Gamma_D \approx 2\pi\times$ 500 MHz at room temperature ($\sim$ 20°C) and D2 hyperfine lines are separated by $\sim 2\pi\times$ 100 MHz that is less than the Doppler width, and can not be ordinarily resolved. Hence to obtain the sub-Doppler resolution second laser field is added. However, later in Chap. 5 and 6, we will show that Doppler broadening is still effective in vapor cells. Addition of Doppler broadening terms leads to following modifications in detunings $\delta_{p(c)} = \delta - (+)kv$ with $\delta = \omega - \omega_0$ and $\delta_d \equiv \delta_p - \delta_c = -2kv$. Thus susceptibility averaged over a Maxwellian distribution is given by

$$\chi = -\frac{3\lambda^2}{2\pi}\cdot\frac{N_{\mathrm{at}}}{\Omega_p}\cdot\int_{-\infty}^{\infty}\frac{\mathrm{d}v}{\sqrt{\pi}v_{mp}}e^{-\left(v/v_{mp}\right)^2}z_2, \tag{3.2.32}$$

where N_{at} is the atomic number density in the vapor cell.

Inegrating Eq. (3.2.32), the background susceptibility is given by

$$\chi_0 = iC_0\exp\left[-\left(\frac{\delta+\gamma_t}{kv_{mp}}\right)^2\right]\mathrm{Erfc}\left[-i\left(\frac{\delta+\gamma_t}{kv_{mp}}\right)^2\right]. \tag{3.2.33}$$

The backgroud susceptibility can be approximated in the Doppler-broadened limit $(kv_{mp} >> \gamma_t)$ given as

$$\chi_0 = C_0e^{-(\delta/kv_{mp})^2}\left[-\mathrm{Erfc}+\left(\frac{\delta+\gamma_t}{kv_{mp}}+i\right)\right], \tag{3.2.34}$$

where

$$C_0 = \frac{3\lambda^3}{8\pi^{3/2}}\cdot\frac{\Gamma N_{at}}{kv_{mp}}$$

In the same Doppler-broadend limit χ_1 and χ_2 are evaluated as

$$\chi_1 = C_0e^{-(\delta/kv_{mp})^2}\frac{s_0\gamma_t}{Q(2\delta+i\gamma_t(1+Q))}, \tag{3.2.35}$$

and

$$\chi_2 = iC_0e^{-(\delta/kv_{mp})^2}\frac{s_0(1-Q)\Gamma\gamma_t}{2Q}\times\frac{(\delta+i(1+Q)\gamma_t)(2\delta+i(1+3Q)\gamma_t)}{(\delta+iQ\gamma_t)(2\delta+i(1+Q)\gamma_t)Z}, \tag{3.2.36}$$

where s_0 is the on-resonance saturation parameter expressed as

$$s_0 = \frac{\Omega_c^2}{\Gamma\gamma_t},$$

with

$$Q = \sqrt{1+s_0},$$

and

$$Z = (2\delta + i(1+Q)\gamma_t) \times (2\delta + i(1+3Q)\gamma_t) + i\Gamma(2\delta + i(1+Q)^2\gamma_t), \qquad (3.2.37)$$

The susceptibility χ_2 due to coherence term presented in Eq. (3.2.36) can be decomposed utilizing partial fraction method, and the term $2\delta + i(1+Q)$ cancels out χ_1 in Eq. (3.2.35). Using Eqs. (3.2.33-3.2.36) in the Eq. (3.2.32), the total susceptibility can be expressed as

$$\chi = C_0 e^{-(\delta/kv_{mp})^2}\left[-\mathrm{Erfc} + \left(\frac{\delta+\gamma_t}{kv_{mp}} + i\right)\right] + C_0 e^{-(\delta/kv_{mp})^2} \times \frac{s_0\gamma_t}{Q} \times \frac{Y}{Z}, \qquad (3.2.38)$$

where Y is expressed as

$$Y = (2\delta + i(1+3Q)\gamma_t) + \frac{i(3-Q)\Gamma}{2} - \frac{(1+Q)\Gamma\gamma_t}{1(\delta + iQ\gamma_t)}, \qquad (3.2.39)$$

A laser field propagating through an isotropic medium with refractive index n and thickness l is attenuated and phase shifted so the output field is given by

$$E_{out} = E_{in}e^{inkz} = E_{in}e^{-n_{\mathrm{Im}}kz}e^{in_{\mathrm{Re}}kz}, \qquad (3.2.40)$$

where $n_{I,R}$ are the imaginary and real parts of the refractive index, and k is the wavenumber. The measurable quantity can then be expressed as

$$I_{out} = |E_{out}|^2 = I_{in}e^{inkz} = E_{in}e^{-in_{\mathrm{Re}}kz}e^{n_{\mathrm{Im}}kz}, \qquad (3.2.41)$$

with $\alpha = 2n_{Im}k$ is the absorption coefficient given by Beer-Lambert's law. Hence, the absorption coefficient, $\alpha = k\mathrm{Im}[\chi]$ can be explicitly expressed as

$$\alpha = kC_0 e^{-(\delta/kv_{mp})^2}(1 - f(\delta)), \qquad (3.2.42)$$

where

$$f(\delta) = -\mathrm{Im}\left[\frac{s_0\gamma_t}{Q}\frac{Y}{Z}\right]. \qquad (3.2.43)$$

Neglecting coherence terms i.e. considering only hole burning term in Eq. (3.2.42) leads to

$$\alpha_H = kC_0 e^{-(\delta/kv_{mp})^2}(1 - f_H(\delta)), \tag{3.2.44}$$

where

$$f_H(\delta) = \frac{s_0\gamma_t^2(1+Q)}{Q(4\delta^2+(1+Q)^2\gamma_t^2)}, \tag{3.2.45}$$

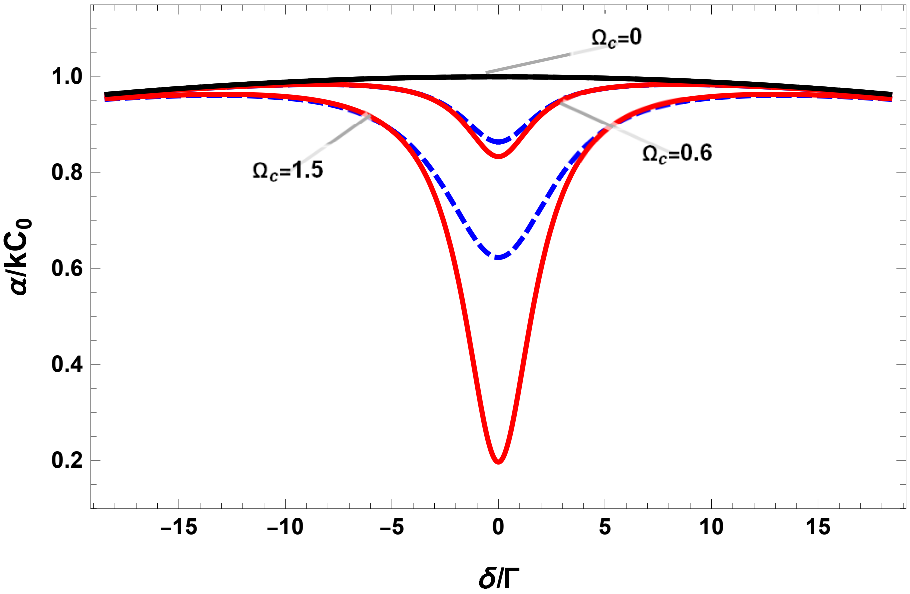

Figure 3.2: Calculated absorption coefficients for $\Omega_c = 0, 0.6$, and 1.5 Γ with fixed probe $\Omega_p = 0.01\Gamma$. Doppler width is $kv_{mp} = 50\Gamma$ as adopted in Fig. 2 of [74]. Blue dashed curves present total absorption spectra (Eq. (3.2.42)) and solid red curves present hole-burning spectra (Eq. (3.2.44)). Whereas normalized background absorption is given for $\Omega_c = 0$.

Equation (3.2.38) presents the complex susceptibility for an idealized closed two-level atomic system in a Doppler-broadened limit. Coherent absorption, hole burning, and background spectra are calculated utilizing the analytical solution for the susceptibility. Figure 3.2 shows the calculated results of Eqs. (3.2.42) and (3.2.44). Fixed $\Omega_p = 0.01\Gamma$ with three different values of $\Omega_c = 0, 0.6\Gamma$ and 1.5 γ are utilized. The black curve shows the normalized background absorption coefficients without a coupling field, i.e., $\Omega_c = 0$. While Blue dashed curves represent total absorption spectra given in Eq. (3.2.42) and solid red curves represent hole-burning spectra given by Eq. (3.2.44).

3.3 Degenerate Atomic Levels

The coherent response of a simple two-level atomic system presented in Sec. 3.2 is an idealized case, measured by a weak probe field with a variable frequency offset and driven by a coexisting strong coupling laser field. Nevertheless, predictions based on the idealized two-level model have proven to be accurate for many experimental observations. However, in the real atoms, levels are degenerate, and the transitions strongly depend on the vectorial nature of the resonant light field. Thus, even in the case of alkali metal atoms with a relatively simple atomic structure due to a single valence electron. There are many allowed transitions between the hyperfine energy levels of the ground state transitions D1 $(5S_{1/2} \rightarrow 5P_{1/2})$ and D2 $(5S_{1/2} \rightarrow 5P_{3/2})$ lines. Hence, resonant light can modify the response of a degenerate atomic system when Zeeman sub-levels are coupled via an optical field.

3.3.1 Three-Level System (EIT)

In the optical domain, the coherent response of a degenerate atomic system is well-realized to demonstrate sub-natural width EIA and EIT resonances attracting considerable attention in the study of multilevel atomic configurations. EIT results from destructive quantum interference between different excitation pathways in a resonant atomic media (mainly Λ, V, and Ξ-type systems), while EIA can be invoked by constructive quantum interference between multiple excitation pathways in a resonant atomic media (mainly N-type systems). Usually, DTLS is theoretically considered to explain EIT and EIA resonances because DTLS can provide the possibility to analyze different level schemes (Λ, V, and N) by appropriate choice of angular momenta of atomic levels and the polarization of coupling and probe fields. For example, a degenerate atomic system with the ground state of total angular momentum $J = 1$ connected to an excited state $J = 0$ by coupling and probe light fields with orthogonal circular polarizations (σ^+ and σ^-) can exhibit EIT phenomenon.

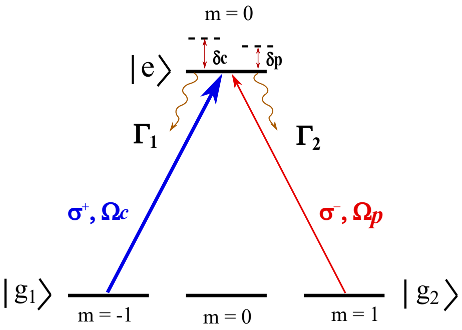

Figure 3.3: Schematic energy-level diagram of the three-level atomic system. The probe field interacts with the transition$F_g = 1 \rightarrow F_e = 0$ of ground and excited state whereas the transition $F_g = -1 \rightarrow F_e = 0$ is coupled by coupling light field. The Rabi frequencies of coupling (probe) fields are Ω_c (Ω_p), respectively. The spontaneous decay rate of the excited states is Γ.

Figure 3.3 shows two ground state levels $m = \pm 1$ coupled to one upper state $m = 0$ level taking form of Λ-type system, with σ^+ the coupling field resonant on $F_g = -1 \rightarrow F_e = 0$ transition and σ^- probe field resonant on $F_g = 1 \rightarrow F_e = 0$ transition. The Rabi frequencies of co-propagating coupling and probe optical fields are Ω_c and Ω_p, respectively. The atomic resonance frequency is given as ω_0, the spontaneous decay rate of the excited state is Γ. The decay rate of optical coherence is defined as γ_t, in the absence of collisional dephasing that is $\gamma_t = \Gamma/2$. Total Hamiltonian of the system without RWA can be expressed as

$$H = \hbar \begin{pmatrix} \omega_0 & \frac{1}{2}\Omega_c e^{it\omega_c} & \frac{1}{2}\Omega_p e^{it\omega_p} \\ \frac{1}{2}\Omega_c e^{-it\omega_c} & 0 & 0 \\ \frac{1}{2}\Omega_p e^{-it\omega_p} & 0 & 0 \end{pmatrix} \tag{3.3.1}$$

Ground state with $m = 0$ is neglected because there is no transition for this state. The effective Hamiltonian of the system after RWA at coupling frequency ω_c is given as

$$H_{RWA} = \hbar \begin{pmatrix} -\delta_c & \frac{\Omega_c}{2} & \frac{1}{2}\Omega_p e^{it\delta_d} \\ \frac{\Omega_c}{2} & 0 & 0 \\ \frac{1}{2}\Omega_p e^{-it\delta_d} & 0 & 0 \end{pmatrix} \tag{3.3.2}$$

where $\delta_c = \omega_c - \omega_0$ is the detuning of coupling field from resonance and $\delta_d = \omega_p - \omega_c$ is the frequency difference of the coupling and probe fields. Additional unitary transformation with a frequency difference δ_d can be applied to remove the remaining time dependence without dropping any terms expressed as

$$H_{eff} = \hbar \begin{pmatrix} -\delta_c & \frac{\Omega_c}{2} & \frac{\Omega_p}{2} \\ \frac{\Omega_c}{2} & 0 & 0 \\ \frac{\Omega_p}{2} & 0 & \delta_d \end{pmatrix} \tag{3.3.3}$$

We can solve the system under steady-state condition utilizing density matrix equation, given by

$$\dot{\rho} = -\frac{i}{\hbar}\left[H_{eff}, \rho\right] + \dot{\rho}_{\mathrm{sp}}, \tag{3.3.4}$$

where, $\dot{\rho}_{\mathrm{sp}}$ accounts for decay due to spontaneous emission calculated by

$$\dot{\rho}_{\mathrm{sp}} = \sum_j \frac{\Gamma_j}{2}\left(\sigma_j \dagger \sigma_j \rho + \rho \sigma_j \dagger \sigma_j - 2\sigma_j \rho \sigma_j^{\dagger}\right), \tag{3.3.5}$$

where $\sigma_j \dagger = |g\rangle \langle e|$ and Γ_j is the decay rate of the $e, g_1, g_2 \in \{|0\rangle, |-1\rangle, |1\rangle\}$. Using Eq. 3.3.4 and solving coherence terms given by off-diagonal elements of the density matrix result in following equations of interest

$$\dot{\sigma}_{\mathrm{eg}_2} = -\left(\gamma_{\mathrm{eg}_2} - i\delta_p\right)\sigma_{\mathrm{eg}_2} - \frac{i\Omega_c}{2}\sigma_{g_1 g_2} + \frac{i\Omega_p}{2}\left(\sigma_{\mathrm{ee}} - \sigma_{g_2 g_2}\right) \tag{3.3.6}$$

$$\dot{\sigma}_{\mathrm{g}_1\mathrm{g}_2} = -\left(\gamma_{g_1 g_2} - i\left(\delta_p - \delta_c\right)\right)\sigma_{g_1 g_2} - \frac{i\Omega_c}{2}\sigma_{\mathrm{eg}_2} + \frac{i\Omega_p}{2}\sigma_{g_1 e} \tag{3.3.7}$$

$$\dot{\sigma}_{\mathrm{eg}_1} = -\left(\gamma_{\mathrm{eg}_1} + i\delta_c\right)\sigma_{eg_1} + \frac{i\Omega_c}{2}\left(\sigma_{g_1g_1} - \sigma_{\mathrm{ee}}\right) + \frac{i\Omega_p}{2}\sigma_{g_2g_2} \tag{3.3.8}$$

Using Eqs. 3.3.6-3.3.8, absorption and dispersion coefficients can be calculated for σ_{eg_2} given by Eq. 3.3.6 in a weak probe limit and assuming majority of population remains in the ground state $|g_2\rangle$ given as

$$\sigma_{\mathrm{eg}_2} \simeq -\frac{\frac{i\Omega_p}{2}}{\left(\gamma_{\mathrm{eg}_2} - i\delta_p\right) + \frac{\Omega_c^2}{4\left(\gamma_{g_1g_2} - i\left(\delta_p - \delta_c\right)\right)}} \tag{3.3.9}$$

The susceptibility (χ) of a three-level system is calculated using Eq. 3.3.9. The absorption coefficient can be found using the imaginary part of the susceptibility (χ_I) and dispersion using the real part (χ_R). Plots of these coefficients are presented in Fig. 3.4 with a sharp transparency window and positive slope of the dispersion.

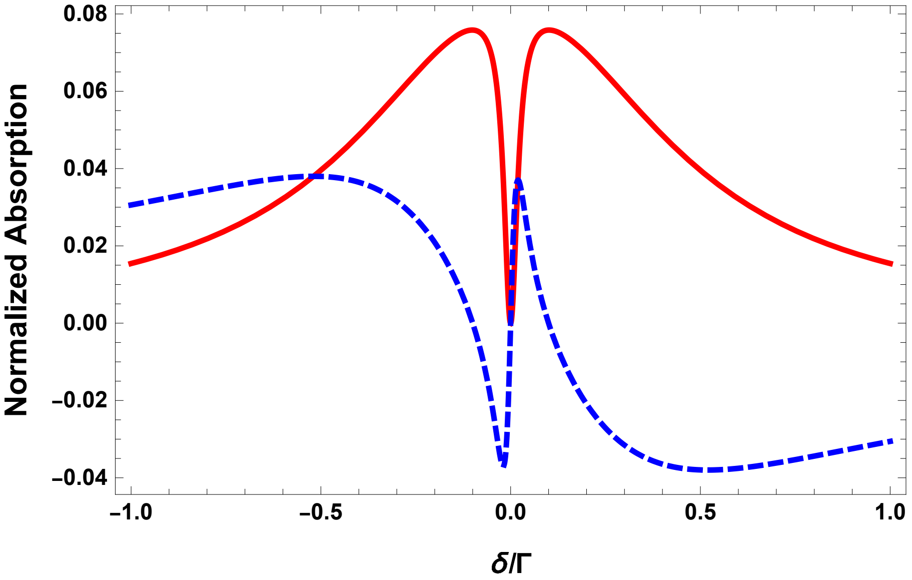

Figure 3.4: Calculated absorption coefficients for $\Omega_c = 0.2\Gamma$, and probe $\Omega_p = 0.01\Gamma$. Blue dashed curves present dispersion spectra and solid red curves present absorption spectra.

3.3.2 Four-Level System (EIA)

Theoretically, EIA has been well explained as a result of TOC utilizing a simple N-type atomic system with four states by Taichenachev *et al.* [75]. They presented an analytical expression for N-type configuration with degenerate excited and ground levels for a weak probe field as a function of the coupling field. A spontaneous cascade of coherence between four states in a N-type configuration demonstrated EIA resonance, which is neglected in simple three-level theoretical models (Λ, V, and Ξ-type systems).

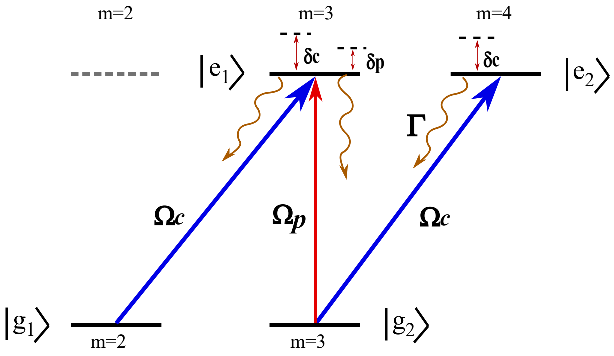

Figure 3.5: Schematic energy-level diagram of the four-level atomic system. The probe field interacts with the transition $|3\rangle \rightarrow |2\rangle$ of ground and excited state whereas the transitions $|1\rangle \rightarrow |2\rangle$ and $|3\rangle \rightarrow |4\rangle$ are coupled by coupling light field. The Rabi frequencies of coupling (probe) fields are Ω_c (Ω_p), respectively. The spontaneous decay rate of the excited states is Γ.

Figure 3.5 shows considered N-type scheme for a four-level atomic system. Just a fraction i.e. $m_g = 2,3 \rightarrow m_e = 3,4$ of a complete DTLS $F_g = 3 \rightarrow F_e = 4$ transition of ^{85}Rb D2 line can be utlized to explain the EIA phenomenon. The probe field interacts with the transition namely $|g_2\rangle \rightarrow |e_1\rangle$ of ground and excited state whereas the transitions $|g_1\rangle \rightarrow |e_1\rangle$ and $|g_2\rangle \rightarrow |e_2\rangle$ are coupled by coupling light field. The Rabi frequencies of coupling (probe) fields are Ω_c (Ω_p), respectively. The spontaneous decay rate of the excited state is Γ, state $|e_1\rangle$ decays to both ground states $|g_1\rangle$ and $|g_2\rangle$, while state $|e_2\rangle$ only decays to state $|g_2\rangle$.

Total Hamiltonian of a four-level system after RWA is given as

$$H_{eff} = \hbar \begin{pmatrix} \delta_c & A\frac{\Omega_c}{2} & 0 & 0 \\ A\frac{\Omega_c}{2} & 0 & B\frac{\Omega_p}{2} & 0 \\ 0 & B\frac{\Omega_p}{2} & \delta_p & \frac{\Omega_c}{2} \\ 0 & 0 & \frac{\Omega_c}{2} & \delta_p - \delta_c \end{pmatrix} \tag{3.3.10}$$

where A and B are real numbers ($A^2 + B^2 = 1$) governing the relative transition amplitudes as given by [75]. Using Eq. 3.3.4 and solving coherence terms given by off-diagonal elements of the density matrix result in the following equation of interest responsible for probe absorption

$$\sigma_{e_1 g_2} = (\Gamma/2 - i\delta_p)^{-1} - iB\Omega_p \left(\sigma_{g_2 g_2} - \sigma_{e_1 e_1}\right) - iA\Omega_c \sigma_{g_1 g_2} + i\Omega_c \sigma_{e_1 e_2} \tag{3.3.11}$$

Eq. 3.3.11 can be approximated by assuming a weak probe limit, i.e., $\Omega_c < \Gamma$ and considering the probe field amplitude in the first order of Ω_p. Thus Eq. 3.3.11 can be replaced as

$$\sigma_{e_1 g_2} = (\Gamma/2 - i\delta_p)^{-1} - \left(iB\Omega_p \sigma_{g_2 g_2} + iA\Omega_c \sigma_{g_1 g_2}\right) \tag{3.3.12}$$

Steady-state solution for $\sigma^{(1)}_{e_1 g_2}$ using perturbation theory is given as

$$\sigma^{(1)}_{e_1 g_2} = -\frac{iB\Omega_p \sigma^{(0)}_{g_2 g_2}}{\frac{\Gamma}{2} - i\delta_p} \left[1 + \frac{A\Omega_c^2}{B^2\Omega_c^2 + \frac{1}{2} i\Gamma\left(\delta_c - \delta_p\right) - \delta_c\left(\delta_c - \delta_p\right)} \right] \tag{3.3.13}$$

where zero and first-order perturbation solutions are presented by (0) and (1) superscripts, respectively, for small Ω_p/Ω_c parameter.

In Eq. 3.3.13, linear absorption of the probe is given by the first term in the square bracket, and contribution of the ground level coherence $\sigma^{(1)}_{g_1 g_2}$ is represented by the second term which results in the increased absorption in the narrow detuning range $\delta = \delta_c - \delta_p$. Figure 3.6 shows the EIA spectra (red solid curves) due to TOC from upper states to the two lower states by spontaneous emission.

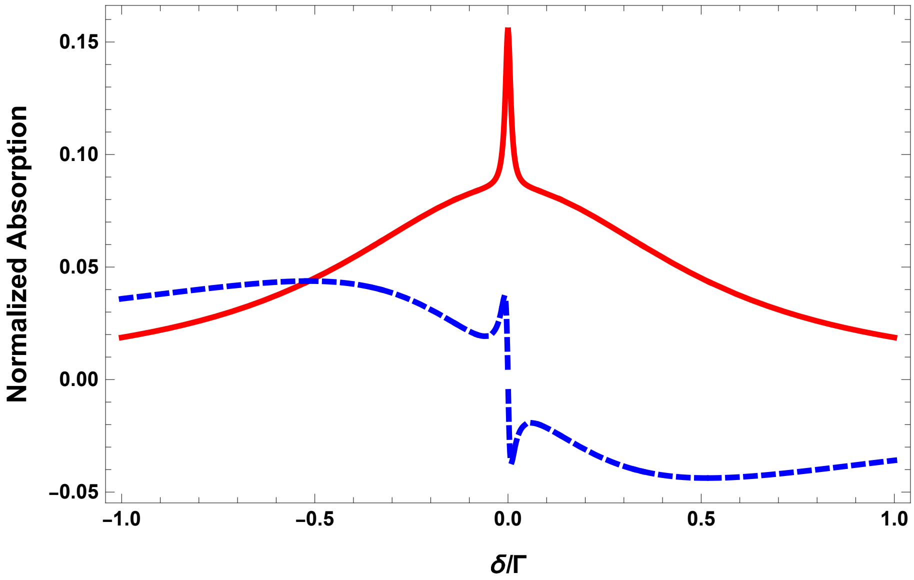

Figure 3.6: Calculated absorption coefficients for $\Omega_c = 0.2\Gamma$, and probe $\Omega_p = 0.01\Gamma$. Blue dashed curves present dispersion spectra and solid red curves present absorption spectra as a function of normalized detuning $\delta/\Gamma = (\delta_c - \delta_p)/\Gamma$, with $\delta_c = 0$

Analytical and numerical modeling approaches based on idealized models have significantly contributed to understanding the involved atom-light interaction processes. Even so, a coherent atom-light interaction picture under realistic experimental conditions is incomplete. Complete understanding of the processes involved requires all dependent parameters to be considered, including level structures, ground and excited level relaxation rates, light intensities and polarization, atomic density, and Doppler broadening effects.

3.4 Atomic Structure

This work develops a theoretical model based on OBEs that qualitatively explain the coherent EIA and EIT resonances of rubidium vapor measured experimentally at D2 lines using coupling-probe spectroscopy. Alkali metal atoms are frequently studied in atomic physics due to their high-oscillator strength at D lines and are ideal species to yield significant absorption in cells of modest length as they have sufficient room temperature vapor pressure. In addition, the D lines in these atoms appear at wavelengths where reliable and inexpensive diode laser sources are available.

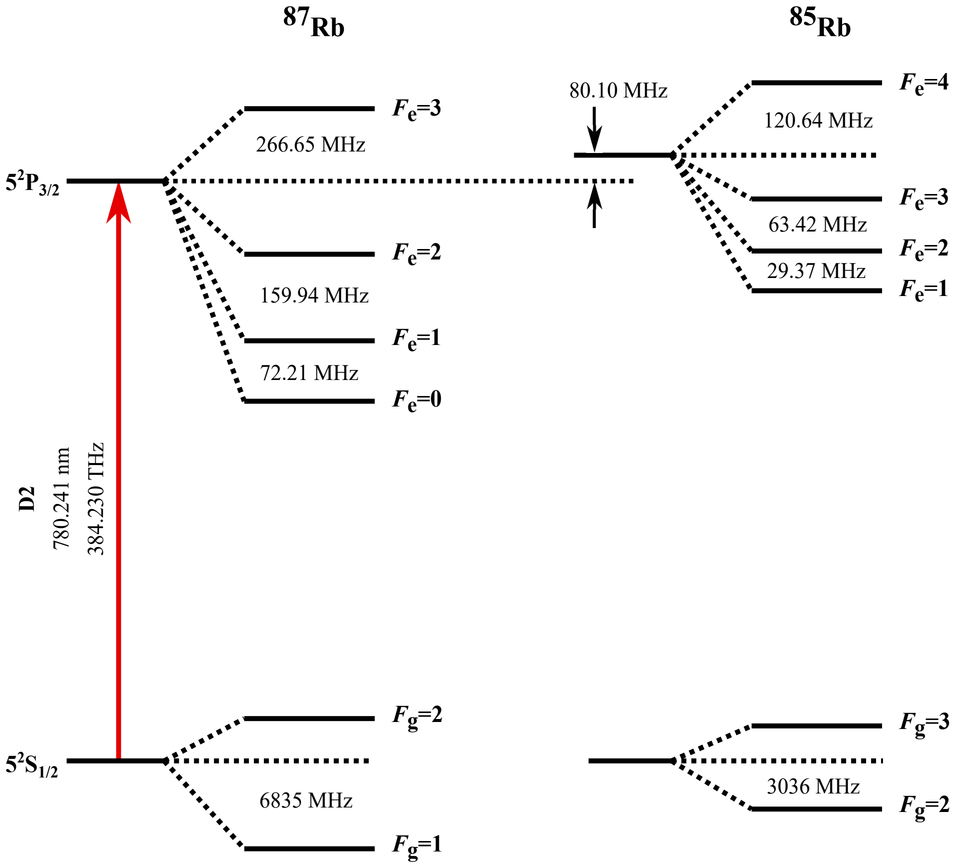

Figure 3.7: A schematic energy level diagram showing the hyperfine structure and intervals of Rb for the D2 spectroscopic lines (not to scale). The $P_{3/2}$ states are offset by 80.1 MHz due to the isotope shift.

In order to precisely model the absorption spectrum, the relative transition frequencies of the hyperfine-resolved energy levels are required for both Rb isotopes, as shown in the figure 3.7. In the absence of hyperfine splitting, the energy level intervals for the atomic transitions are set to be relative to the center of mass for the D2 ($5s^2S_{1/2} \rightarrow 5p^2P_{1/2}$) transition. Even with a relatively simple atomic structure due to a single valence electron, there are many allowed transitions between the hyperfine energy levels of the alkali-metal atoms. The dipole matrix elements for each transition between ground and excited state characterize the strength of the interaction between an atom and a near-resonant light field given by

$$\left\langle F_g, m_{F_g} \right| -\overrightarrow{d}.E_0\hat{\varepsilon}_q \left| F_e, m_{F_e} \right\rangle \tag{3.4.1}$$

To calculate the dipole matrix elements we can write the matrix elements as a product of Wigner $3-j$ and $6-j$ symbols

$$\left\langle F_g, m_{F_g} \right| -\overrightarrow{d}.E_0\hat{\varepsilon}_q \left| F_e, m_{F_e} \right\rangle = \hbar\Omega C^{F_e,m_{F_e}}_{F_g,m_{F_g}} \tag{3.4.2}$$

where,

$$\begin{aligned} C^{F_e,m_{F_e}}_{F_g,m_{F_g}} &= (-1)^{2F_e+I+2J_g+L_e+S-m_{F_e}} \\ &\times \sqrt{(2L_e+1)(2F_g+1)(2F_e+1)(2J_g+1)(2J_e+1)} \\ &\times \begin{Bmatrix} L_e & 1 & L_g \\ J_g & S & J_e \end{Bmatrix} \begin{Bmatrix} J_e & 1 & J_g \\ F_g & I & F_e \end{Bmatrix} \begin{pmatrix} F_e & 1 & F_g \\ m_{F_e} & q & m_{F_g} \end{pmatrix} \end{aligned} \tag{3.4.3}$$

In Eq. 3.4.3, $6-j$ symbols are enclosed in curly brackets and $3-j$ are enclosed in round brakets. Symbols F, I, J, L, S, and m_f are the angular quantum numbers, and q (=-1, 0, and 1) is the integer change in m_F due to σ^-, π , and σ^+ transitions. Nuclear spin (I) has the value $\frac{3}{2}$ and $\frac{5}{2}$ for ^{87}Rb and ^{85}Rb, respectively. The electron spin, given by S has the value of $\frac{1}{2}$.

3.5 Outlook

Developing ideal models for simple atomic systems that accurately reproduce experimental spectra has been key to a great deal of research. These models have been a valuable tool in extracting critical physical parameters and can predict novel effects. However, there remains a need for a degenerate multilevel model applicable to a range of experimental parameters and numerically simulate the essential dynamics of atom-light interactions in realistic atomic systems. One of the primary motivations for this work was to extend this model to the subtleties and extra complications introduced by the unresolved real atoms in a vapor cell. This principle method is extended to degenerate hyperfine levels with higher-order oscillation frequency mixing in Chap. 4 and adding the neighboring hyperfine transitions in Chap. 5 and 6.

Chapter 4

Multiphoton Interactions

4.1 Overview

In this chapter, multiphoton nonlinear frequency mixing effects on coherent electromagnetically induced absorption spectra of ^{85}Rb atoms using two orthogonal linear polarizations of strong coupling and weak probe beams are investigated theoretically and experimentally concerning an applied longitudinal magnetic field and coupling powers. Herein, we confirm for the first time that at least five-photon interactions in solving density matrix equations for the $F_g = 3 \rightarrow F_e = 4$ transition of ^{85}Rb atoms are required to explain experimentally observed coherent electromagnetically induced absorption spectra when a quantum axis is selected as the propagation direction of co-propagating coupling and probe laser beams. Distinct calculated spectral differences due to magnetic field variations and coupling power between three- and five-photon interactions are confirmed. The obtained asymmetrical spectral shapes match very well with those calculated from five-photon interactions considering the off-resonant $F_g = 3 \rightarrow F_e = 2, 3$ transitions. Genuine, coherent spectral shapes are observed with a single laser combined with two acousto-optic modulators, wherein the spectral resolution is limited because of the decoherence rate between Zeeman sublevels in the ground state from transit-time relaxation.

4.2 Theory for 3PI and 5PI in DTLS under LMF

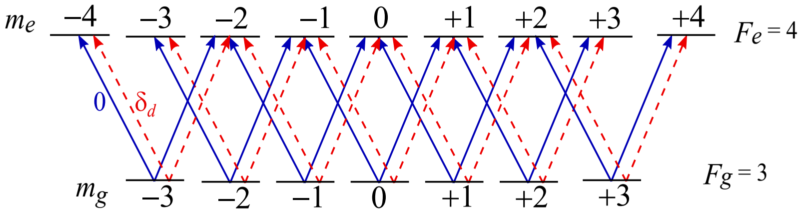

Figure 4.1: Transition schemes with two circularly polarized coupling and probe beams for energy level of the $5S_{1/2}(F_g = 3) - 5P_{3/2}(F_e = 4)$ transition of ^{85}Rb atoms.

The energy level diagram for the $5S_{1/2}(F_g=3)-5P_{3/2}(F_e=4)$ transition of ^{85}Rb atoms is shown in Fig. 4.1. The co-propagating coupling and probe beams are linearly polarized in directions perpendicular to each other. The detuning of the probe (coupling) beam in the rest frame of an atom moving with velocity v is expressed as $\delta_1=\delta_p-kv$ ($\delta_2=\delta_c-kv$), where δ_p (δ_c) is the detuning of the probe (coupling) beam, and k $(=2\pi/\lambda)$ and λ are the wavevector and wavelength of the laser beams, respectively. To implement an applied magnetic field in the calculation, we select the propagation direction of the laser beams as a quantization axis. The density matrix equation in the rotating frame of frequency of the coupling beam is expressed as

$$\dot{\rho}=-\frac{i}{\hbar}[H_0+H_i,\rho]+\dot{\rho}_{\mathrm{sp}}, \tag{4.2.1}$$

where ρ is the density operator. The atomic Hamiltonian H_0 is expressed as

$$\begin{aligned} H_0 \quad = \quad & \sum_{m=-4}^{4}\hbar\left(-\delta_2+g_e\mu_B Bm\right)\left|F_e=4,m\right\rangle\left\langle F_e=4,m\right| \\ & +\sum_{m=-3}^{3}\hbar g_g\mu_B Bm\left|F_g=3,m\right\rangle\left\langle F_g=3,m\right|, \end{aligned} \tag{4.2.2}$$

where μ_B is the Bohr magneton; B is the LMF; and $g_e(=1/2)$ and $g_g(=1/3)$ are the Landé g-factors of the states $5P_{3/2}(F_e=4)$ and $5S_{1/2}(F_g=3)$, respectively. In Eq. (4.2.1), the interaction Hamiltonian V is expressed as

$$\begin{aligned} H_i \quad = \quad & \sum_{q=\pm1}\sum_{m=-3}^{3}\frac{\hbar}{2}\left(a_q e^{-i\delta_d t}\Omega_p+b_q\Omega_c\right)C_m^{m+q} \\ & \times\left|F_e=4,m+q\right\rangle\left\langle F_g=3,m\right|+\text{h.c.}, \end{aligned} \tag{4.2.3}$$

where Ω_p (Ω_c) and $a_{\pm}=\mp1/\sqrt{2}$ ($b_{\pm}=i/\sqrt{2}$) are the Rabi frequency and the coefficient of the electric field of the probe (coupling) beam in the spherical bases, respectively. In Eq. (4.2.3), h.c. denotes the Hermitian conjugate, $C_{m_g}^{m_e}$ is the normalized transition strength between the states $\left|F_e=4,m_e\right\rangle$ and $\left|F_g=3,m_g\right\rangle$ [21], and $\delta_d (\equiv \delta_1 - \delta_2 = \delta_p - \delta_c)$ the difference in the detunings of the probe and coupling beams. Thus, “0” (“δ_d”) in Fig. 1(a) denotes the relative detuning of the coupling (probe) beam with respect to the frequency of the coupling beam. In Eq. (4.2.1), $\dot{\rho}_{\mathrm{sp}}$ represents the spontaneous emission term, whose matrix elements are shown in Eq. (3) in [32]. The finite interaction time between atoms and laser beams is considered in the calculation by employing a transit relaxation constant [33].

Because two different frequencies of the electric fields appear simultaneously for the available transitions, as shown in Fig. 4.1, the density matrix elements can be decomposed into many Fourier components. In the 5PI (3PI) calculation, the 5PI (3PI) for the optical coherences and four (two) photon interactions for the populations and Zeeman coherences are considered. Hence, in the 5PI calculation, the density matrix elements of the optical coherence, Zeeman coherences, and populations are explicitly expressed as

$$\begin{aligned}
\rho_{e_{m\pm\varepsilon},g_m} &= \rho^{(1)}_{e_{m\pm\varepsilon},g_m} + \rho^{(2)}_{e_{m\pm\varepsilon},g_m} e^{-i\delta_d t} + \rho^{(3)}_{e_{m\pm\varepsilon},g_m} e^{i\delta_d t} \\
&\quad + \rho^{(4)}_{e_{m\pm\varepsilon},g_m} e^{-2i\delta_d t} + \rho^{(5)}_{e_{m\pm\varepsilon},g_m} e^{2i\delta_d t} + \rho^{(6)}_{e_{m\pm\varepsilon},g_m} e^{-3i\delta_d t}, \\
\rho_{e_{m\pm\mu},e_m} &= \rho^{(1)}_{e_{m\pm\mu},e_m} + \rho^{(2)}_{e_{m\pm\mu},e_m} e^{-i\delta_d t} + \rho^{(3)}_{e_{m\pm\mu},e_m} e^{i\delta_d t} \\
&\quad + \rho^{(4)}_{e_{m\pm\mu},e_m} e^{-2i\delta_d t} + \rho^{(5)}_{e_{m\pm\mu},e_m} e^{2i\delta_d t}, \\
\rho_{g_{m\pm\nu},g_m} &= \rho^{(1)}_{g_{m\pm\nu},g_m} + \rho^{(2)}_{g_{m\pm\nu},g_m} e^{-i\delta_d t} + \rho^{(3)}_{g_{m\pm\nu},g_m} e^{i\delta_d t} \\
&\quad + \rho^{(4)}_{g_{m\pm\nu},g_m} e^{-2i\delta_d t} + \rho^{(5)}_{g_{m\pm\nu},g_m} e^{2i\delta_d t}, \\
\rho_{\alpha,\beta} &= \rho^{*}_{\beta,\alpha},
\end{aligned} \tag{4.2.4}$$

where $\varepsilon = 1, 3$, and 5; $\mu = 0, 2$, and 4, and $\nu = 0, 2$, and 4, for all the relevant values of m. We use the simplified notations for the matrix elements in Eq. (4.2.4), as follows:

$$\begin{aligned}
\rho_{e_{m'},g_m} &= \left\langle F_e = 4, m' \right| \rho \left| F_g = 3, m \right\rangle, \\
\rho_{e_{m'},e_m} &= \left\langle F_e = 4, m' \right| \rho \left| F_e = 4, m \right\rangle, \\
\rho_{g_{m'},g_m} &= \left\langle F_g = 3, m' \right| \rho \left| F_g = 3, m \right\rangle.
\end{aligned} \tag{4.2.5}$$

Notably, the elements $\rho^{(2)}_{e_{m\pm1},g_m}$ in Eq. (4.2.4) contribute to the probe absorption. This is because the matrix elements of $\rho^{(2)}_{e_{m\pm1},g_m}e^{-i\delta_d t}$ contribute to the dipole moment oscillating at the frequency of the probe field and are responsible for the probe absorption as in Eq. (4.2.7) below.

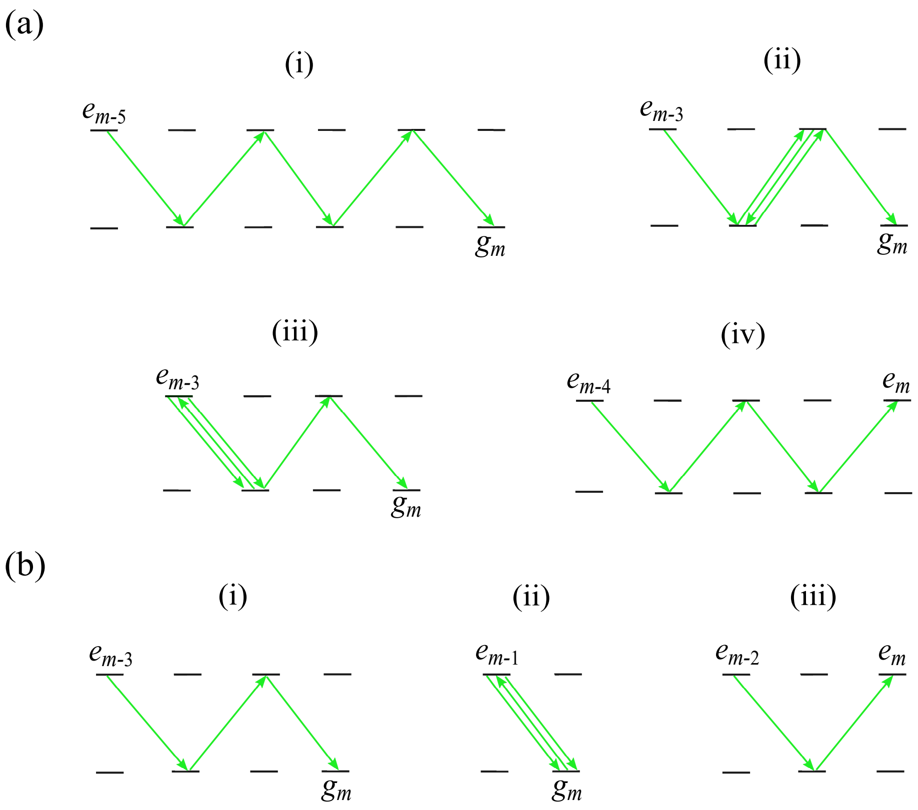

Figure 4.2: Typical possible routes connecting the states by coupling and probe photons: a(i) 5PI between $|e_{m-5}\rangle$ and $|g_m\rangle$, a(ii) between $|e_{m-3}\rangle$ and $|g_m\rangle$, a(iii) between $|e_{m-3}\rangle$ and $|g_m\rangle$, and a(iv) between $|e_{m-4}\rangle$ and $|e_m\rangle$, b(i) 3PI between $|e_{m-3}\rangle$ and $|g_m\rangle$, b(ii) between between $|e_{m-1}\rangle$ and $|g_m\rangle$, b(iii) between $|e_{m-2}\rangle$ and $|e_m\rangle$. The green arrows denote the transitions by the mixed coupling and probe beams simultaneously to avoid confusion..

Figure 4.2 (a) shows typical connection configurations among various possible configurations for 5PI between the magnetic sublevels of the excited and ground states by the coupling and probe photons. Fig. 4.2 a(i) shows the 5PI between the sublevels $|e_{m-5}\rangle$ and $|g_m\rangle$. In each emission (absorption) process, the contribution to the net oscillation frequencies are given by $\{0,-\delta_d\}$ ($\{0,\delta_d\}$).

Therefore, the resultant oscillation frequencies via the 5PI in Fig. 4.2 a(i) are given by

$$\begin{aligned}&\{0,-\delta_d\}\oplus\{0,\delta_d\}\oplus\{0,-\delta_d\}\oplus\{0,\delta_d\}\oplus\{0,-\delta_d\}\\ \rightarrow\quad &\{0,-\delta_d,\delta_d,-2\delta_d,2\delta_d,-3\delta_d\}.\end{aligned}$$

Figures 4.2 a(ii) and a(iii) show two typical 5PI between the sublevels $|e_{m-3}\rangle$ and $|g_m\rangle$. The resultant oscillation frequencies for these connections are the same as those for the connection between the sublevels $|e_{m-5}\rangle$ and $|g_m\rangle$. Although there exist another connections between the sublevels $|e_{m-3}\rangle$ and $|g_m\rangle$, the oscillation frequencies remain unchanged. Therefore, we can conclude that the oscillation frequencies for the optical coherences $\rho_{e_{m\pm\varepsilon},g_m}$ within the 5PI are given by $\{0,-\delta_d,\delta_d,-2\delta_d,2\delta_d,-3\delta_d\}$. Figure 4.2 a(iv) shows the four photon interactions between the sublevels $|e_{m-4}\rangle$ and $|e_m\rangle$, and the oscillation frequencies are given by

$$\begin{aligned}&\{0,-\delta_d\}\oplus\{0,\delta_d\}\oplus\{0,-\delta_d\}\oplus\{0,\delta_d\}\\ \rightarrow\quad &\{0,-\delta_d,\delta_d,-2\delta_d,2\delta_d\}.\end{aligned}$$

In an analogous method, we can construct the decompositions of the other density matrix elements in Eq. (4.2.4). Because we can select non-zero components of the density matrix elements, the density matrix equations in Eq. (4.2.1) can be numerically solved rapidly and efficiently. In this sense, we can state that our method solving density matrix equations is distinct from the perturbative approach as discussed in Ref. [76], where how subsequent orders of ρ are coupled and the density matrix ρ to a given order $\rho^{(n)}$ can thus be expressed in terms of the elements $\rho^{(n-1)}$ of the next-lowest order to solve the optical Bloch equations.

In the 3PI calculation, the optical and Zeeman coherences (and populations) in Eq. (4.2.4) are truncated at $\rho^{(4)}$ and $\rho^{(3)}$, respectively, and are explicitly expressed as

$$\begin{aligned}
\rho_{e_{m\pm\varepsilon},g_m} &= \rho^{(1)}_{e_{m\pm\varepsilon},g_m} + \rho^{(2)}_{e_{m\pm\varepsilon},g_m} e^{-i\delta_d t} + \rho^{(3)}_{e_{m\pm\varepsilon},g_m} e^{i\delta_d t} \\
&\quad + \rho^{(4)}_{e_{m\pm\varepsilon},g_m} e^{-2i\delta_d t}, \\
\rho_{e_{m\pm\mu},e_m} &= \rho^{(1)}_{e_{m\pm\mu},e_m} + \rho^{(2)}_{e_{m\pm\mu},e_m} e^{-i\delta_d t} + \rho^{(3)}_{e_{m\pm\mu},e_m} e^{i\delta_d t}, \\
\rho_{g_{m\pm\nu},g_m} &= \rho^{(1)}_{g_{m\pm\nu},g_m} + \rho^{(2)}_{g_{m\pm\nu},g_m} e^{-i\delta_d t} + \rho^{(3)}_{g_{m\pm\nu},g_m} e^{i\delta_d t},
\end{aligned} \tag{4.2.6}$$

where $\varepsilon = 1, 3$, and 5; $\mu = 0, 2$, and 4, and $\nu = 0, 2$, and 4. Figure 4.2 (b) shows how typical oscillation frequencies for 3PI are generated. In an analogous method for 5PI, the resultant oscillation frequencies via the 3PI for the optical coherence with $\Delta m = 3$ ($\Delta m = 1$) in Fig. 4.2 b(i) [b(ii)] are given by $\{0, -\delta_d\} \oplus \{0, \delta_d\} \oplus \{0, -\delta_d\} \rightarrow \{0, -\delta_d, \delta_d, -2\delta_d\}$. In Fig. 1 c(iii), the frequencies of the Zeeman coherence are given by $\{0, -\delta_d\} \oplus \{0, \delta_d\} \rightarrow \{0, -\delta_d, \delta_d\}$. Comparing Eqs. (4.2.4) and (4.2.6), The terms of $\rho^{(5)}_{e_{m\pm\varepsilon},g_m}$ and $\rho^{(6)}_{e_{m\pm\varepsilon},g_m}$ neglected in the 3PI calculation are considered in the 5PI calculation. This kind of inclusion of more terms for the density matrix elements increases the precision of the calculation.

After inserting Eqs. (4.2.2), (4.2.3), and (4.2.4) into Eq. (4.2.1), we obtain coupled differential equations for the matrix elements, which are then solved numerically as functions of δ_p, δ_c, and v. Finally, the absorption coefficient of the probe beam is expressed as

$$\begin{aligned}
\alpha = &-\frac{3\lambda^2}{2\pi}\frac{N_{\mathrm{at}}}{\Omega_p}\int_{-\infty}^{\infty}\frac{\mathrm{d}v}{\sqrt{\pi}u}e^{-(v/u)^2} \\
&\times \mathrm{Im}\left[\sum_{q=\pm1}\sum_{m=-3}^{3} a_q^* C_m^{m+q} \rho^{(2)}_{e_{m+q},g_m}\right],
\end{aligned} \tag{4.2.7}$$

where N_{at} is the atomic vapor density in the cell, and u is the most probable speed in the cell.

Here, we describe the effect of the quantization axis on the accuracy of the calculation. When the direction of the coupling field is selected as the quantization axis, only the optical coherences ρ_{e_m,g_m} between the sublevels with $\Delta m = 0$

do not vanish, and all the other optical coherences vanish. Thus, when the probe field is very weak, because the optical coherences with $\Delta m \neq 0$ is not significant, the calculation can be very accurate although only 3PI processes are considered.

However, when the direction of the laser field is selected as the quantization axis, all the optical coherences with $\Delta m = \pm 1, \pm 3, \pm 5, \ldots$ do not vanish. Therefore, higher photon interactions are required to obtain sufficient accuracy in the calculation, such as 5PI processes. Because it is convenient to select the direction of the magnetic field as the quantization axis in the presence of a longitudinal magnetic field, at least a 5PI calculation is needed to obtain accurate calculated results of the EIA spectra.

4.3 Experimental Setup

The schematic of the experimental setup is shown in Fig. 4.3. A laser beam for the $5S_{1/2} \rightarrow 5P_{3/2}$ transition of ^{85}Rb atoms at 780 nm is generated using a tunable external cavity diode laser (DLPro, Toptica Inc.) with a typical output power of 100 mW in a single-mode regime. A window (W) is used to extract 4% of the total output power of the laser beam for a frequency locking to the $F_g = 3 \rightarrow F_e = 4$ resonance line of ^{85}Rb atoms for saturated absorption spectroscopy. The polarizing beam splitter-1 (PBS-1) passes an intense p-polarized coupling beam and reflects a weak counter-propagating s-polarized probe beam reflected through a neutral density filter (NDF) from a mirror into photodiode-1 (PD-1) to detect the saturated absorption signals. A quarter-wave plate (QWP) is utilized to change the incoming p-polarized coupling beam to an s-polarized probe beam. The NDF controls the power ratio between the coupling and probe beams.

EIA spectra are obtained using a single laser beam combined with two AOMs with a central frequency of 80 MHz in a double-pass scheme, as shown in Fig. 2. The intense main beam transmitting the W is separated into a weak p-polarized probe beam directed to a half-wave plate (HWP) in front of PBS-5 and an intense s-polarized coupling beam directed to AOM-1 using PBS-2 and an HWP after the W. The coupling beam double passes the AOM-1. The reflected coupling

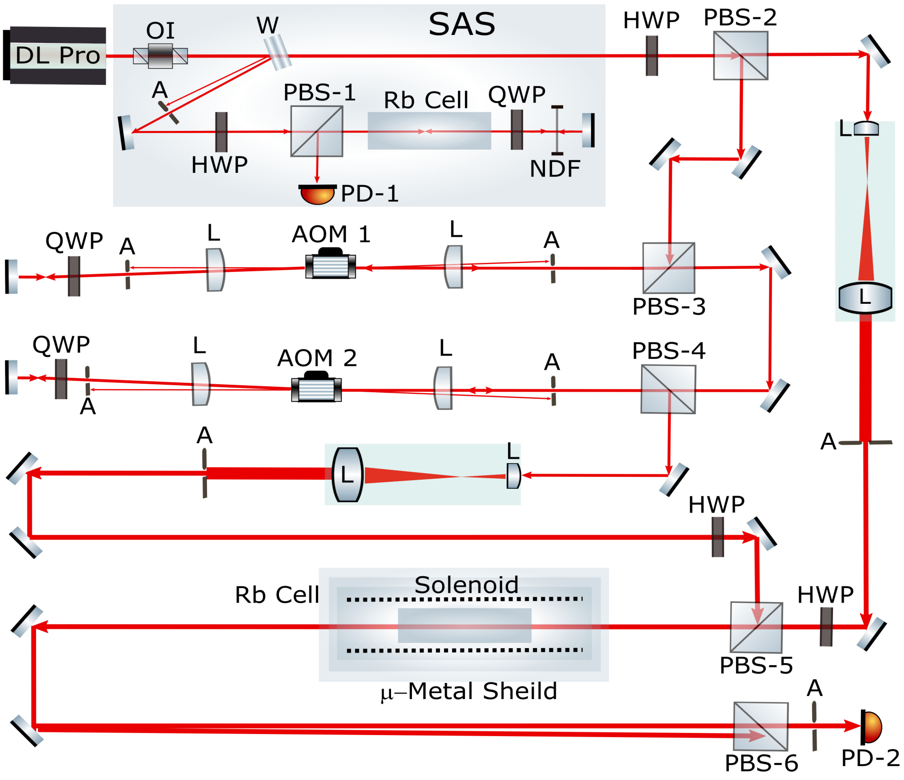

Figure 4.3: Schematic experimental setup using a single laser combined with two AOMs. Component symbols: OI, optical isolator; W, window; SAS, saturation absorption spectroscopy; HWP, half-Wave plate; PBS, polarizing beam splitter; A, aperture, QWP, quarter-wave plate; NDF, neutral density filter; L, lens; PD, photodiode; AOM, acousto-optic modulator.

beam transmits PBS-3, and the procedure performed in AOM-1 is similarly implemented in AOM-2. Subsequently, the coupling beam from AOM-2 is expanded by 5× to combine at PBS-5 with the weak probe beam expanded after PBS-2 to obtain a uniform intensity across a 4-mm-diameter beam. PBS-5 is used to overlap the co-propagating probe and coupling beams with the orthogonal-linear polarizations upon a vapor cell containing ^{85}Rb atoms at room temperature.

An external LMF is applied to the vapor cell with a solenoid surrounding vapor cell shielded with five layers of μ-metal sheets to remove the effect of stray and earth's magnetic fields inside the cell. Probe absorption is detected at the PD-2 when PBS-6 is used to separate the s-polarized coupling beam, and an intersection angle of ~ 0.1 mrad is maintained for possible leakage due to polarization rotations introduced by the applied external magnetic field.

4.4 Results and Discussions

This section compares the observed coherent spectra with the calculated spectra to elucidate the observed coherent spectral characteristics from 5PI, discernible from those of 3PI concerning the coupling powers and LMF.

4.4.1 Spectral features depending on coupling powers without LMF

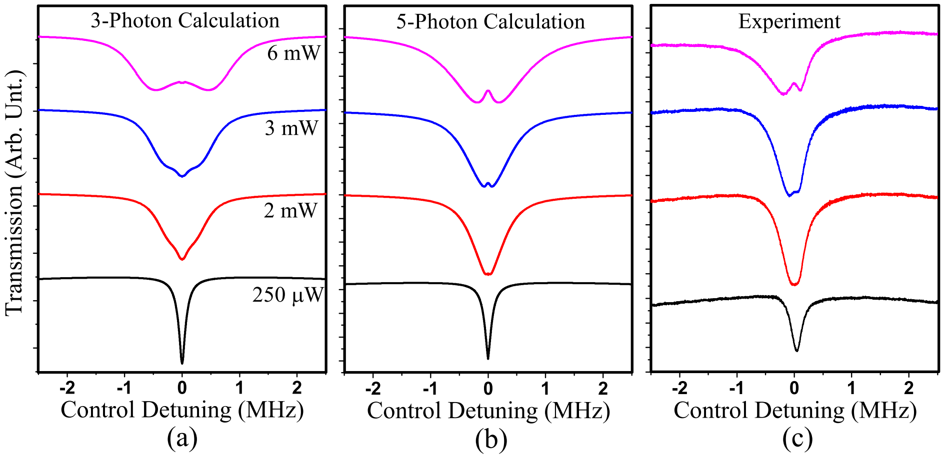

Figure 4.4: EIA spectra without magnetic field by varying coupling power (250 μW to 6 mW) with fixing probe power at 15 μW. (a) Calculation using 3PI, (b) 5PI, and (c) experimental measurements.

Dependences of coupling powers on the EIA spectra with a weak linearly polarized probe beam perpendicular to the coupling beam resonant with the $F_g = 3 \rightarrow F_e = 4$ transition of ^{85}Rb atoms at room temperature without a magnetic field (i.e., $B = 0$) are investigated. Numerical spectral calculations utilizing the 3PI and 5PI and experimentally measured EIA spectra by varying the coupling field powers (0.25 to 6 mW) with a fixed probe of 15 μW and a laser beam diameter of 4 mm are shown in Fig. 3.

The spectral calculations utilizing the 3PI and 5PI are shown in Fig. 4.4 (a) and Fig. 4.4 (b), respectively, and the experimental measurement in Fig. 4.4 (c) show a similar spectral feature as those from 3PI and 5PI in the weak coupling power of 0.25 mW. For strong coupling powers above 2 mW, discernible spectral feature differences are observed in the central region of the spectra between the 3PI and 5PI. The 3PI calculation is characterized by an ultranarrow dip embedded in a narrow dip at the central region. The amplitude of the ultranarrow dip decreases with the increase in the coupling power, and the sign of the dip inverts after ∼4 mW (not shown in Fig. 4.4 (a)). With the increase in the coupling power, the narrow dip splits into two broad dip features, as shown in the coupling power of 6 mW. The central EIA signal for atoms moving at a constant velocity becomes split due to Autler-Towns (ATS) splitting from the strong coupling power. After performing an average over Maxwell-Boltzmann velocity distribution in the calculation, two separated EIA signals as shown in Fig. 4.4 (b) are created, and therefore a central EIT-like transmission peak emerges [28]. However, ATS is unclear due to the ultranarrow dip feature in the lower coupling powers at the center of the spectra. Broad ATS features beside the central ultranarrow dip are resolved with the linewidth of 479 kHz at 5 mW (not shown in Fig 4.4 (a)) and 480 kHz at 6 mW, as shown in Fig. 4.4 (a).

Unlike the 3PI calculation, the 5PI calculation is characterized by a narrow and ultranarrow peak embedded in a narrow dip owing to ATS at the central region developing from 2.5 up to 6 mW power increase. Broad ATS features besides the central ultranarrow peak further develop in the separations with linewidths of 62 and 147 kHz at 3 and 6 mW of coupling powers, respectively, as shown in Fig. 4.4 (b), whereas such ATS is not observed at lower powers.

The experimental coherent spectra show that ATS develops weakly at the central region at 2.5 mW but increases with the coupling power up to 6 mW, similar to the 5PI calculation. The amplitudes of the broad ATS feature beside the central ultranarrow and asymmetric peak further develop in the separations with linewidths of 83 and 178 kHz at 3 and 6 mW of coupling powers, respectively, as shown in Fig. 4.4 (c). The experimentally observed spectra show spectral behaviors similar to those from the 5PI calculation, as shown in Fig. 4.4 (b), with ATS at higher powers. The asymmetric spectra is due to the off-resonant $F_g = 3 \rightarrow F_e = 2$ and $F_g = 3 \rightarrow F_e = 3$ transitions of ^{85}Rb atoms. The detailed explanations for the origin of the asymmetric spectra are given in section 4.4.5.

From these analyses, 5PI calculations instead of 3PI calculations at higher coupling powers provide reliable results for predicting experimental EIA spectra with the quantum axis as the propagation direction of laser fields without a magnetic field. It should be noted that the coherence between the magnetic sublevels connected via coupling and probe beams increases when the laser beam's intensities are weak. As the laser beam's intensities increase, the coherence reaches a maximum when the effective Rabi frequency is comparable to the linewidth of the transition under consideration and then decreases [77].

4.4.2 Spectral features depending on coupling powers with LMF of 0.3 G

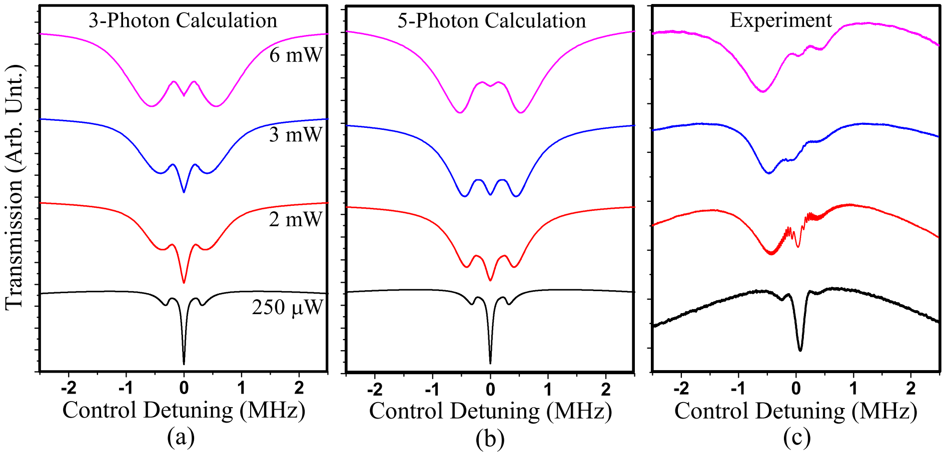

Figure 4.5: EIA spectra with 0.3 G magnetic field by varying coupling power (250 μW to 6 mW) and fixing probe power at 15 μW. (a) Calculation using 3PI, (b) 5PI, and (c) experimental measurements.

A static magnetic field is applied in the direction of laser propagations in the coupling-probe system such that in the spectral simulation, a quantum axis can be selected as the direction of the applied LMF to simplify the system for solving OBEs.

Unlike the case without an applied magnetic field, the spectra split into two Zeeman sidebands beside the central spectrum. The sidebands' splittings due to the Zeeman effect match well with the observed ones, which can be used as frequency calibration. Unlike the case without an applied magnetic field described in Section 4.4.1, spectral mixing effects are observed on the coherent spectra owing to Zeeman splitting and ATS due to strong coupling powers. Hence, the calculated and observed spectral features exhibit ATS even at lower powers, unlike the spectra without an applied field. At higher coupling powers, the spectra with the ATS effect mix more significantly with the spectra from the Zeeman effect. Spectral differences between the 3PI and 5PI results from the central part of the spectra are shown in Figs. 4.5 (a) and 4.5 (b).

Numerical spectral calculations utilizing the 3PI and 5PI are shown in Figs. 4.5 (a) and 4.5 (b), respectively, and the experimental measurement in Fig. 4.5 (c) show a similar spectral feature in the weak coupling power of 0.25 mW. In the calculated EIA spectra utilizing the 3PI, the amplitude of the ultranarrow dip at the central region of the spectra decreases slowly compared with the amplitude of ultranarrow dip obtained from the 5PI with the increases in the coupling powers. The spectral profiles of the 3PI calculation differ from those of the 5PI calculation. The linewidth is 147 kHz at 3 mW and increases to 153 kHz at 6 mW of coupling power, as shown in Fig. 4.5 (a). The amplitudes of the dips decrease with the increases in the coupling power up to 6 mW. In the calculated EIA spectra utilizing the 5PI, the linewidths are 157 and 143 kHz at 3 and 6 mW of coupling powers, respectively, as shown in Fig. 4.5 (b).

Figure 4.5 (c) shows the experimentally measured EIA spectra by varying the coupling field powers (0.25 to 6 mW) with a fixed probe of 15 μW and an applied LMF of 0.3 G. Because of the applied LMF, the spectral feature with the increased linewidth of EIA spectra owing to ATS and the magnetic field differs significantly from that with the linewidths in the case without an LMF. The spectral asymmetry of the observed spectra is more significant than that without a magnetic field; this is attributable to the off-resonant transitions of ^{85}Rb atoms (See the explanations in the section 4.4.5 below). The linewidths are 192 and 174 kHz at 3 and 6 mW, respectively, comparable to the calculated linewidths utilizing the 5PI. The 5PI calculation instead of the 3PI calculation provides better matches with the observed spectra.

4.4.3 Spectral features depending on coupling powers with LMF of 1 G

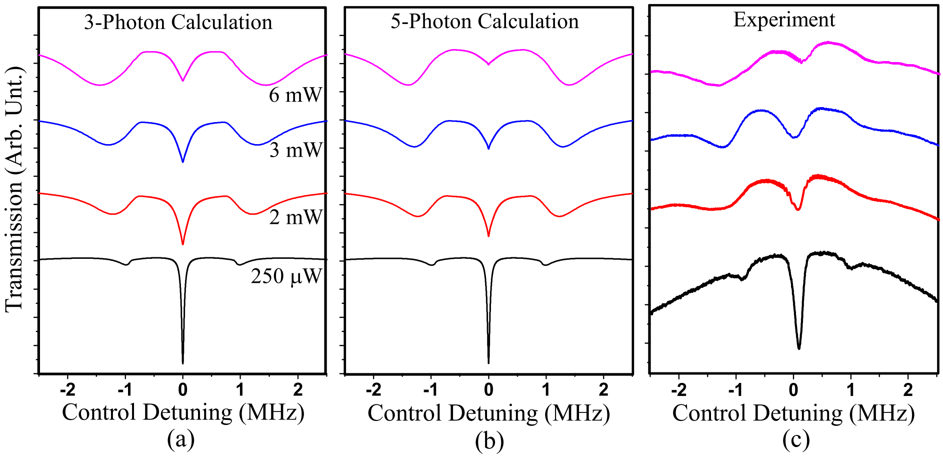

Figure 4.6: EIA spectra with 1 G magnetic field by varying coupling intensity (250 μW to 6 mW) and fixing probe at 15 μW. (a) Calculation using 3PI, (b) 5PI, and (c) experimental measurements.

At a higher magnetic field of 1 G, the 3PI and 5PI calculations differ less for each power, although the central amplitudes between the 3PI and 5PI indicate slight differences at higher powers, as discussed in Section 4.4.2. For other weaker magnetic field cases, the central peaks of the 5PI are smaller than those of the 3PI. However, the decrease in the amplitude of the central peak is slighter than the decrease in the amplitude in lower magnetic fields with the increasing coupling power. The slight differences between the 3PI and 5PI calculations at a higher magnetic field may result from the significant Zeeman shifts of the energies of the degenerate sublevels. In this case, each transition shown in Fig. 4.1 becomes non-resonant and diminishes the coherent effects, and accordingly, the effect of higher-photon interactions becomes insignificant.

Figure 4.6 shows EIA spectra with 1 G magnetic field by varying coupling intensity (250 μW to 6 mW) and fixing probe at 15 μW. The central EIA dip at $B = 1$ G for the measured signal with 250 μW has a 162 kHz linewidth, whereas a narrow linewidth is obtained in the calculations, i.e., 51 and 55 kHz using the 3PI and 5PI, shown in Fig. 4.6 (a) and (b) respectively. The separation of EIA sidebands is proportional to the applied magnetic field magnitude, i.e., approximately 1 MHz per 1 G. No significant trend difference is observed between the measurements and calculations except the broad linewidth and lower amplitude of the observed experimental EIA signal. The broad linewidth of the experimental measurement is due to the sustained angle of 0.3 mrad between the probe and coupling fields to eliminate the coupling beam leakage on the detector, whereas a missing ultranarrow region below 80 kHz resulted in a lower amplitude of the measured EIA signal. The central EIA signals decrease concerning the increases in the magnetic field, thereby reducing N-type connections between the magnetic sublevels owing to the Zeeman splittings.

4.4.4 Spectral features depending on LMF with fixed coupling power of 3 mW

In this subsection, magnetic field dependencies on EIA spectra are investigated at an intermediate coupling power of 3 mW. Numerical spectral calculations utilizing the 3PI and 5PI as well as experimental measurements by varying the magnetic field (0 to 0.9 G) with a fixed probe (15 μW) and coupling power (3 mW) at the evident ATS limit of the coupling powers are shown in Figs. 4.7 (a), 4.7 (b), and 4.7 (c), respectively. An applied magnetic field separates the EIA lines owing to the Zeeman effect, as shown in Fig. 4.7; consequently, distinct spectral differences owing to the magnetic field and ATS due to strong coupling powers

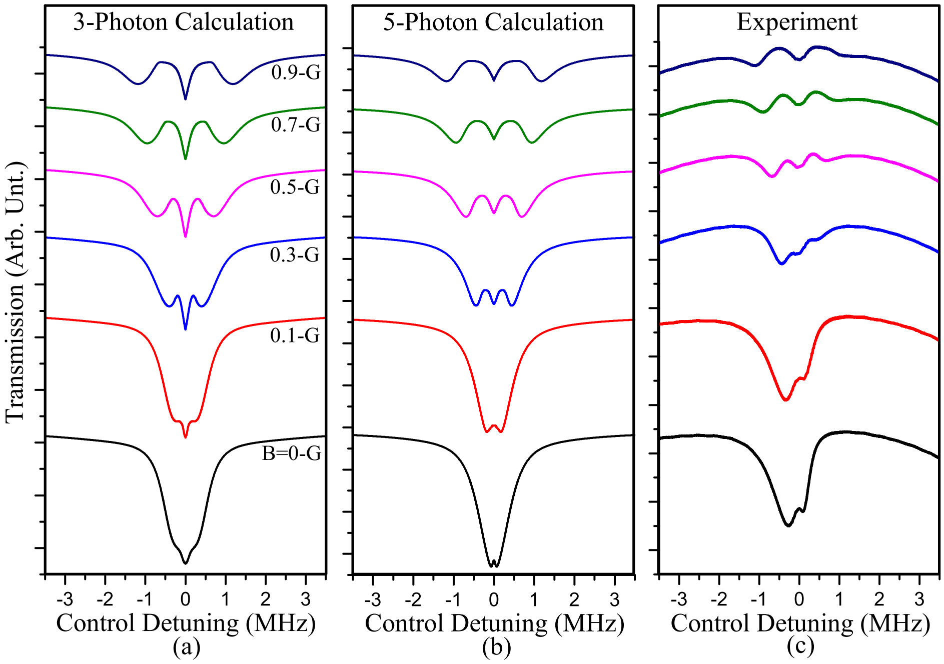

Figure 4.7: EIA spectra by varying magnetic field (0 to 1 G) with fixed probe and coupling power of 15 μW and 3 mW, respectively. (a) Calculation using 3PI, (b) 5PI, and (c) experimental measurements.

between the 3PI and 5PI calculations in the central region of the spectra are observed. Hence, spectral features owing to multiphoton frequency mixing effects are discernible through spectral comparisons between the calculated and observed spectra.

Major spectral trend differences in the central region of the spectra from utilizing the 3PI and 5PI calculations are evident at lower magnetic fields, as discussed in Sections 4.4.2 and 4.4.3. Unlike the case without an applied magnetic field described in Section 4.4.1. Spectral mixing effects are observed on the coherent spectra due to the strong coupling power due to the Zeeman splittings and ATS. At higher coupling powers and the ATS limit, the spectra from the ATS effect are mixed with the spectra from the Zeeman effect. Spectral differences between the 3PI and 5PI resulting from the central part of the spectra are shown in Figs. 4.7 (a) and (b). At lower magnetic fields of $B = 0$, 0.1, and 0.3 G, the spectral differences are evident because the ultranarrow signals at the central portion of the spectra have opposite signs with dips and peaks owing to coherent effects between the 3PI and 5PI, respectively. EIA spectral energy separations from the Zeeman effect due to magnetic fields of 0.1 to 0.9 G are larger than ATS due to the coupling power.

The spectral profiles from the 3PI calculation differ from those of the 5PI calculation with the increase in the magnetic field. In the calculated EIA spectra from the 3PI, the amplitudes of the ultranarrow central dip for the 3PI calculation increase and reach the maximum and then decrease with the increase in the magnetic field. The minimum of the central dip in the 3PI is more profound than those of the sidebands at lower magnetic fields.

The ultranarrow central peak for the 5PI calculation below 0.3 G increases in amplitude and changes to an ultranarrow central dip above 0.1 G. The amplitude of the dip reaches the maximum and then decreases with the increase in the magnetic field. Unlike the 3PI case, a peak is observed below 0.3 G in the 5PI calculation, and the minimum central dip above 0.1 G is slightly smaller than the sidebands.

The experimental results are similar to those of the 5PI calculation compared to the 3PI calculation for points wherein the starting point of the central EIA dip is above 0.1 G, and the linewidth and ending point of the central peak is below 0.3 G.

The minimum central dip in the observed case is shallower than those at the sidebands, similar to the 5PI calculation. As afore-described, the experimental spectra are similar to the spectra from the 5PI calculation. The background signal at the right side is higher than that at the left side for the experimental spectra, resulting in an asymmetric signal.

4.4.5 Physcial nature of asymmetric spectral features

To study the origin of large asymmetric spectral features shown in Fig. 4.8 (i) with the probe power of 15 μW, the coupling power of 6 mW, and $B = 0.3$ G, two different calculations with 5PI process have been done: first case is the calculation

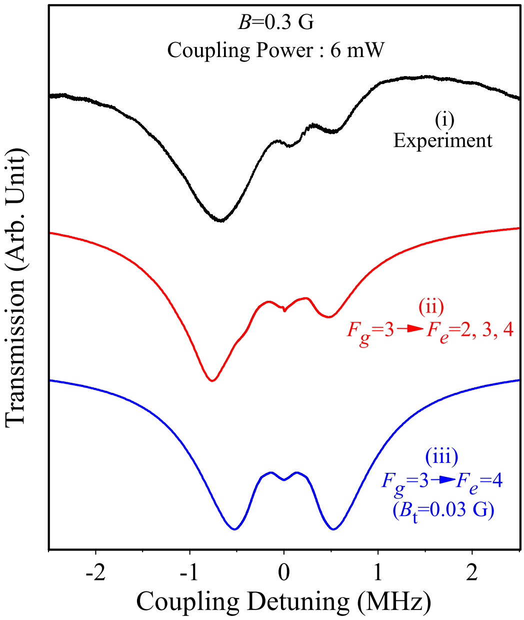

Figure 4.8: EIA spectra with 0.3 G of magnetic field at coupling power of 6 mW and probe power of 15 μW from (i) experimental measurement, (ii) calculation with considering the off-resonant $F_g = 3 \rightarrow F_e = 2,3$ transitions without the transverse magnetic field of 30 mG with 5PI, and (iii) calculation without considering the off-resonant $F_g = 3 \rightarrow F_e = 2,3$ transitions with the transverse magnetic field of 30 mG with 5PI.

as shown in Fig. 4.8 (ii) when the off-resonant $F_g = 3 \rightarrow F_e = 2$ and $F_g = 3 \rightarrow F_e = 3$ transitions are included as well as the resonant $F_g = 3 \rightarrow F_e = 4$ transition described in detail above. Second case is the calculation as shown in Fig. 4.8 (iii) when a transverse magnetic field of 30 mG included to investigate the effects on asymmetrical spectra of any stray transverse magnetic field when only the resonant $F_g = 3 \rightarrow F_e = 4$ transition is considered.

From the asymmetric behavior of the result shown in Fig. 4.8 (ii) without the transverse magnetic field of 30 mG we can readily interpret that the asymmetric spectrum results from the off-resonant transitions because when the transverse magnetic field of 30 mG is included, asymmetric spectrum is not produced as shown in Fig. 4.8 (iii). Therefore, we can conclude that the asymmetric spectral feature found in the experiment results mainly from the effect of the off-resonant transitions. The calculation described in this subsection is preliminary only to investigate the origin of the experimentally observed asymmetric spectra.

4.5 Outlook

Multiphoton frequency mixing effects on coherent EIA spectra of ^{85}Rb atoms are investigated theoretically and experimentally based on an applied LMF and coupling powers with two orthogonal linear polarizations of co-propagating strong coupling and weak probe beams. Coherent EIA spectra between 3PI and 5PI calculations due to magnetic field magnitude variations and ATS due to intense coupling powers are distinguishable. The experiment is performed using a single laser combined with two AOMs to reveal the distinct, coherent EIA spectra from the 5PI, wherein the linewidth is limited owing to the decoherence rate between Zeeman sublevels in the ground state from the transit-time relaxation.

We confirm for the first time that at least 5PI are required for solving density matrix equations for the $F_g = 3 \rightarrow F_e = 4$ transition of ^{85}Rb atoms in the case where a quantum axis is selected as the propagation field direction to elucidate experimentally observed coherent EIA spectra from nonlinear multiphoton mixing effects.

We realize that observed asymmetrical spectra originate mainly from off-resonant transitions ($F_g = 3 \rightarrow F_e = 2, 3$) instead of a transverse stray magnetic field coming from an imperfect LMF. 3PI calculations are sufficient to explain the observed coherent spectra with fewer pathways connected between the sublevels at large magnetic fields or weak coupling powers. Although there are no significant differences between the experimental and calculated 5PI results, the studies of the detailed effects of higher photon interactions exceeding 5PI on the EIA spectra and more detailed analyses on origins of asymmetrical spectral behaviors are the topic of next chapters.

Chapter 5

Mechanisms of EIA and EIT Transformation

5.1 Overview

In this chapter, optical Bloch equations are solved with and without neighboring hyperfine states near the degenerate two-level system (DTLS) in the challenging case of ^{85}Rb D2 transition that involves the Doppler broadening effect. The calculated spectra agree well with the experimental results obtained using the coupling-probe scheme with orthogonal linear polarizations of the coupling and probe fields. The mechanisms of electromagnetically induced absorption (electromagnetically induced transparency) for the open $F_g = 3 \rightarrow F_e = 2$ and 3 transitions (open $F_g = 2 \rightarrow F_e = 2$ and 3 transitions) are determined to be the effect of the strong closed $F_g = 3 \rightarrow F_e = 4$ transition line (strong closed $F_g = 2 \rightarrow F_e = 1$ transition line) based on the comparisons of the calculated absorption profiles of a DTLS without neighboring states and those of all levels with neighboring states depending on the coupling and probe power ratios. The crucial factors established based on comparisons of the calculated absorption profiles of DTLS with and without neighboring states, which enhance or reduce coherence effects and result in transformation between electromagnetically induced absorption and electromagnetically induced transparency, are the power ratios between coupling and probe beams, openness of the excited state, and effects of the neighboring states due to the Doppler broadening in a real atomic system.

5.2 Theoretical Model

This section describes a method of calculating the EIA spectra while considering the neighboring effect. As the details of the calculation have been reported previously [21, 28, 32, 33, 73], we briefly present the method of calculation. The energy-level diagram of D2 transition line of ^{85}Rb atoms is presented in Fig. 5.1

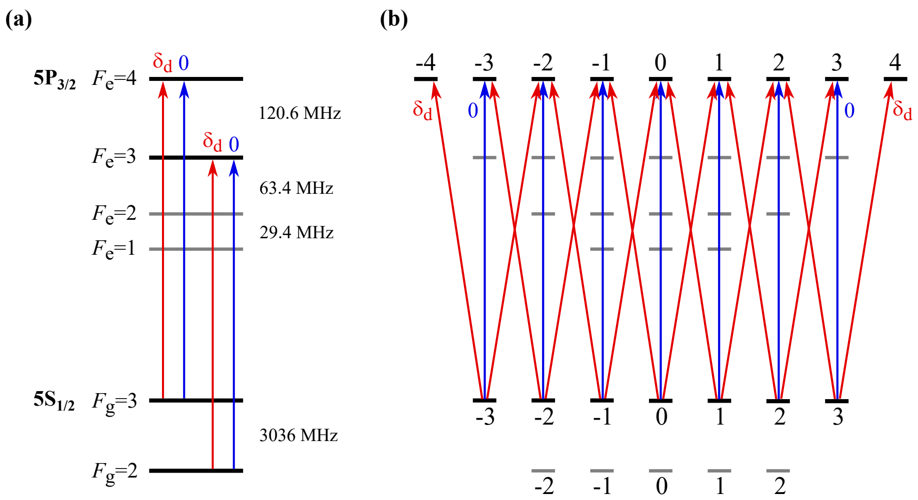

Figure 5.1: (a) Energy-level diagram of D2 transition lines of a ^{85}Rb atom, wherein the red and blue lines indicate transitions by the probe and coupling beams, respectively. (b) Transition scheme with two linearly polarized coupling and probe beams in the case of $F_g = 3 \rightarrow F_e = 4$ transition, where “0” (blue lines) and “δ_d” (red lines) imply the transitions excited by the coupling and probe beams, respectively. The excitations for the $F_g = 3 \rightarrow F_e = 2$ and 3 transitions are not shown to avoid confusion.

(a). The coupling and probe beams that are linearly polarized with orthogonal directions propagate in the same directions. The Rabi frequency and effective detuning of the coupling (probe) beam are denoted by Ω_c (Ω_p) and δ_c (δ_p), respectively. The effective detunings are given by $\delta_c = d_c - kv$ and $\delta_p = d_p - kv$, where d_c (d_p) denotes the frequency detuning of the coupling (probe) beam, $k(= 2\pi/\lambda)$ is the wave vector, λ is the resonance wavelength of the lasers, and v is the atomic velocity. Here, d_c and d_p are the detunings relative to the resonance transition line under consideration.

Because the energy separation between the hyperfine states in $5S_{1/2}$ ground state is approximately six times the Doppler linewidth of the atoms, we can calculate the EIA spectra for the $F_g = 3 \rightarrow F_e = 2, 3$, and 4 transitions and $F_g = 2 \rightarrow F_e = 1, 2$, and 3 transitions separately. In the description of the calculation method, the $F_g = 3 \rightarrow F_e = 2, 3$, and 4 transitions are assumed. In a frame rotating with the coupling beam’s frequency, the density matrix describing the internal dynamics of the atoms is given by

$$\dot{\rho} = -\frac{i}{\hbar}\left[H_0 + H_i, \rho\right] + \dot{\rho}_{\text{relax}}, \tag{5.2.1}$$

where ρ is the density operator and H_0 (H_i) is the atomic (interaction) Hamiltonian.

In Eq. (3.2.1), the atomic Hamiltonian is given by

$$\begin{aligned} H_0 \ = \ & -\sum_{m=-4}^{4} \hbar\delta_c \left|F_e = 4, m\right\rangle \left\langle F_e = 4, m\right| \\ & -\sum_{m=-3}^{3} \hbar\left(\delta_c + \Delta_{43}\right) \left|F_e = 3, m\right\rangle \left\langle F_e = 3, m\right| \\ & -\sum_{m=-2}^{2} \hbar\left(\delta_c + \Delta_{42}\right) \left|F_e = 2, m\right\rangle \left\langle F_e = 2, m\right|, \end{aligned} \tag{5.2.2}$$

where Δ_{4j} is the frequency spacing between the hyperfine states $\left|F_e = 4\right\rangle$ and $\left|F_e = j\right\rangle$ ($j = 2$ and 3). In Eq. (5.2.1), the interaction Hamiltonian is given by

$$\begin{aligned} H_i \ = \ & \frac{\hbar}{2}\Omega_p e^{-i\delta_d t} \sum_{q=-1}^{1} \sum_{F_e=2}^{4} \sum_{m=-3}^{3} a_q C_{3,m}^{F_e,m+q} \left|F_e, m+q\right\rangle \left\langle F_g, m\right| \\ & + \frac{\hbar}{2}\Omega_c \sum_{F_e=2}^{4} \sum_{m=-3}^{3} C_{3,m}^{F_e,m} \left|F_e, m\right\rangle \left\langle F_g, m\right| + \text{h.c.}, \end{aligned} \tag{5.2.3}$$

where $F_g = 3$, $a_{\pm 1} = \mp 1/\sqrt{2}$, $a_0 = 0$, and h.c. denotes Hermitian conjugate. In Eq. (5.2.3), $C_{F_g,m_g}^{F_e,m_e}$ is the normalized transition strength between states $\left|F_e, m_e\right\rangle$ and $\left|F_g, m_g\right\rangle$ [21] and $\delta_d (\equiv \delta_p - \delta_c = d_p - d_c)$ is the difference in the detunings of the probe and coupling beams. In Eq. (5.2.1), $\dot{\rho}_{\text{relax}}$ represents the terms related to the relaxation mechanism such as spontaneous emission and transit time decay [32, 33].

As reported previously in [21, 28, 32, 33, 73], the density matrix elements are decomposed into various oscillation components. In the orthogonal linear polarization configuration, the coupling and probe beams excite the transitions with

$\Delta m = 0$ and $\Delta m = \pm 1$, respectively, where Δm is the difference in the magnetic quantum numbers between the sublevels under consideration. In Fig. 5.1 (b), “0” and “δ_d” imply the transitions excited by the coupling and probe beams, respectively. As stated earlier, δ_d is the effective frequency of the probe beam relative to the frequency of the coupling beam. The method of determining the oscillation frequencies of the density matrix elements for the orthogonal linear polarization configuration has been described in detail in Chap. 4 section 4.4.2. Herein, only an explicit expansion of the density matrix elements that are responsible for the probe absorption is given by

$$\rho_{e^{Fe}_{m\pm1},g_m} = \rho^{(1)}_{e^{Fe}_{m\pm1},g_m} e^{-i\delta_d t} + \rho^{(2)}_{e^{Fe}_{m\pm1},g_m} e^{i\delta_d t},$$

where the simplified notation for the density matrix elements is given by

$$\rho_{e^{Fe}_{me},g_{mg}} \equiv \langle F_e, m_e| \rho \left| F_g = 3, m_g \right\rangle .$$

We have considered all the density matrix elements between the sublevels that are connected via photons numbers not greater than three. The absorption coefficient of the probe beam is thus given by

$$\begin{aligned} \alpha &= -\frac{3\lambda^2}{2\pi}\frac{N_{\mathrm{at}}}{\Omega_p}\int_{-\infty}^{\infty}\frac{\mathrm{d}v}{\sqrt{\pi}v_{\mathrm{mp}}}e^{-\left(v/v_{\mathrm{mp}}\right)^2} \\ &\quad \times \mathrm{Im}\left[\sum_{F_e=2}^{4}\sum_{q=-1}^{1}\sum_{m=-3}^{3} a_q^* C_{3,m}^{F_e,m+q}\rho^{(1)}_{e^{Fe}_{m+q},g_m}\right], \end{aligned} \tag{5.2.4}$$

where N_{at} is the atomic number density in the cell and v_{mp} is the most probable speed in the cell.

5.3 Experimental Setup

The coupling and probe beams are generated using a single laser (DLPro, Toptica Inc.) combined with two AOMs in a single-pass configuration, as shown in Fig.

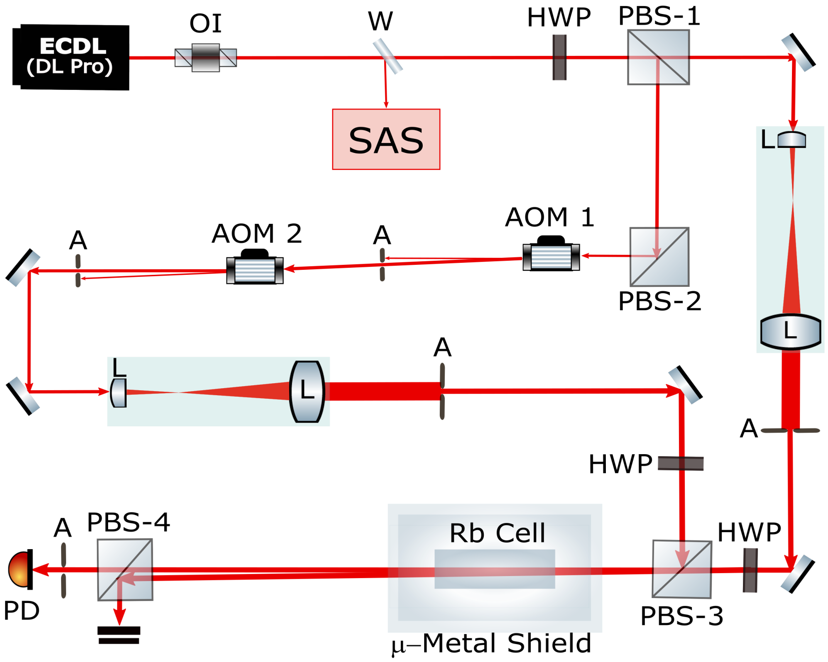

Figure 5.2: Experimental setup. Component symbols: OI: optical isolator; W: window; SAS: saturation absorption spectroscopy; HWP: half-wave plate; PBS: polarizing beam splitter; A: aperture; QWP: quarter-wave plate; L: lens; PD: photodiode; AOM: acousto-optic modulator.

5.2. A combination of HWP and PBS-1 controls the ratio between the coupling and probe beam's intensities and polarizations. A weak-probe-beam power of 15 μW and a coupling beam with a scanning frequency of 5 MHz at a low coupling power of 50 μW and strong coupling power of 4 mW were used. The coupling and probe beams were expanded five times to obtain a uniform intensity across a 4-mm diameter. The coupling beam with the scanning detuning (Δ) from AOM-2 is combined with the weak probe at PBS-3 and co-propagates with orthogonal linear polarizations while maintaining an angle of intersection of approximately 0.1 mrad through the vapor cell shielded with five layers of μ-metal sheets. PBS-4 eliminates the coupling beam before detecting the probe intensity at PD. The desired $5S_{1/2} \rightarrow 5P_{3/2}$ transition of ^{85}Rb D2 hyperfine line is locked using a saturation absorption spectroscopy (SAS) setup. The experiments are performed with ^{85}Rb atoms in a vapor cell at room temperature.

5.4 Results

This section compares the theoretical results while considering resonant and all neighboring transitions resulting in EIAs and EITs with the experimental results. We theoretically and experimentally investigate the resonance spectra for two spectrally unresolved groups of hyperfine transitions of ^{85}Rb D2 lines, i.e., $F_g = 3 \rightarrow F_e = 2,3$, and 4 and $F_g = 2 \rightarrow F_e = 1,2$, and 3, with a weak-probe-beam power of 15 μW and coupling beam with a scanning frequency of 5 MHz both at a low coupling power of 50 μW and strong coupling power of 4 mW, as shown in Fig. 5.3 and Fig. 5.4. For simplicity, we use simplified notations for the transitions; e.g., the $F_g = 3 \rightarrow F_e = 4$ transition is expressed as $3 \rightarrow 4'$ where unprimed (primed) integers represent the angular momentum quantum numbers in the ground (excited) states.

5.4.1 $F_\mathrm{g} = 3 \rightarrow F_\mathrm{e} = 2,3,$ and 4 Transitions

Figure 5.3 presents a comparison of the calculated spectra considering (a) a pure DTLS with transitions resonant at $3 \rightarrow 2'$, $3 \rightarrow 3'$, and $3 \rightarrow 4'$; (b) a transition resonant at $3 \rightarrow 2'$ with neighboring hyperfine transitions of $3 \rightarrow 3'$ and $4'$, a transition resonant at $3 \rightarrow 3'$ with neighboring hyperfine transitions of $3 \rightarrow 2'$ and $4'$, and a transition resonant at $3 \rightarrow 4'$ with neighboring hyperfine transitions of $3 \rightarrow 2'$ and $3'$; and (c) experimentally measured spectra with transitions resonant at $3 \rightarrow 2'$, $3 \rightarrow 3'$, and $3 \rightarrow 4'$ for two different weak (50 μW) and strong (4 mW) coupling powers as shown in the top and bottom traces, respectively.

First, we explain the cases of a weak coupling power as shown in the top trace of Fig. 5.3. In pure two-level calculations on the left side of the top trace, a closed $3 \rightarrow 4'$ transition satisfies all three necessary EIA conditions [2] and presents a relatively strong EIA amplitude with a linewidth of 57 kHz, as expected. For open transitions, $3 \rightarrow 3'$ and $3 \rightarrow 2'$, EIT spectra with small amplitudes and a linewidth resolution of 46 kHz and 41 kHz are obtained, respectively. Considering all the neighboring states near the resonant transitions of $3 \rightarrow 2'$, $3 \rightarrow 3'$, and $3 \rightarrow 4'$, as

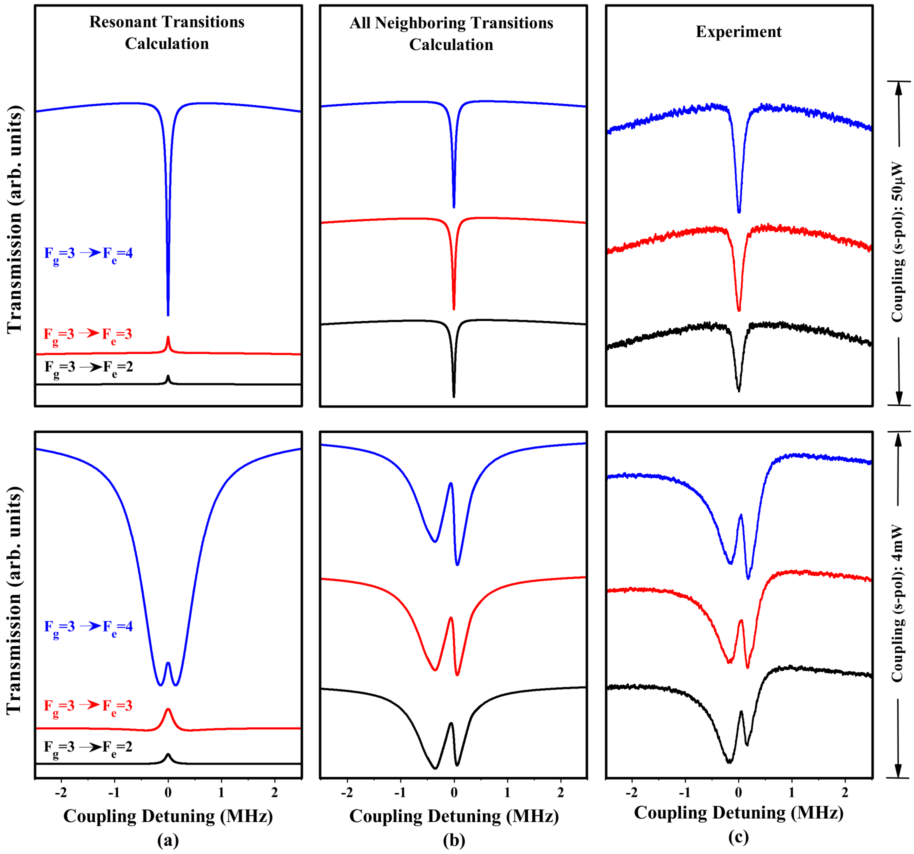

Figure 5.3: Comparison of calculated and measured spectra considering: (a) pure two-level resonant transitions, i.e., $2 \rightarrow 1'$, $2 \rightarrow 2'$ and $2 \rightarrow 3'$, (b) transition resonant at $2 \rightarrow 1'$ with neighboring hyperfine transitions of $2 \rightarrow 2'$ and $3'$, transition resonant at $2 \rightarrow 2'$ with neighboring transitions of $2 \rightarrow 1'$ and $3'$, transition resonant at $2 \rightarrow 3'$ with neighboring transitions of $2 \rightarrow 1'$ and $3'$, and (c) experimentally measured spectra for resonant transitions $2 \rightarrow 1'$, $2 \rightarrow 2'$ and $2 \rightarrow 3'$.

shown in the upper trace of Fig. 5.3 (b), all the resonant transitions show strong EIAs with similar amplitudes owing to a nearby closed $3 \rightarrow 4'$ transition, which exhibits strikingly similar trends in the spectra as the measured spectra. However, the observed spectra are wider than the calculated ones. Measured ultra-narrow EIA dips at low coupling power are resolved with linewidths of 163 kHz, 156 kHz, and 167 kHz, whereas the linewidths obtained using all the neighboring transitions calculation are 60 kHz, 60 kHz, and 58 kHz at the $3 \rightarrow 4', 3'$, and $2'$ transitions, respectively.

Second, we explain the case of a strong coupling power, as shown in the bottom trace of Fig. 5.3. In pure two-level calculations on the left side of the bottom trace, a closed $3 \rightarrow 4'$ transition satisfies all three necessary EIA conditions [2] and indicates a relatively strong EIA amplitude with a wide linewidth of 1.06 MHz and splits into two broad dips at the center of the spectra, resulting in the emergence of a narrow EIT-like peak with the 117 kHz linewidth resolution. These EIA spectra at a strong coupling power are attributed to the contributions of positive and negative atomic velocities in the case of orthogonal polarizations, resulting in two identical EIA spectra separated at the center after thermal averaging [28]. EIT spectra with small amplitudes and wide linewidths of 194 kHz and 122 kHz for open transitions $3 \rightarrow 3'$ and $3 \rightarrow 2'$, respectively, are obtained, as shown in lower traces of Fig. 5.3 (a).

Including all the other adjacent transitions, such asymmetric EIA is transformed into asymmetric line profiles owing to the strong neighboring effects, which differ at the red and blue detuning regions. Considering all the neighboring states near the resonant transitions of $3 \rightarrow 2'$, $3 \rightarrow 3'$, and $3 \rightarrow 4'$, as shown in the lower trace of Fig. 5.3 (b), owing to a nearby closed $3 \rightarrow 4'$ transition, all the resonant transitions exhibit strong EIAs with similar amplitudes, exhibiting strikingly similar trends in the spectra compared to the measured spectra for the closed $3 \rightarrow 4'$ transition. Asymmetric dips due to two separated EIAs at a strong power in the calculation (measurement) are broad, with linewidths of 870 kHz, 848 kHz, and 842 kHz (607 kHz, 606 kHz, and 603 kHz) in the red detuning and narrow with linewidths of 297 kHz, 292 kHz, and 287 kHz (439 kHz, 402 kHz, and 377 kHz) in the blue detuning at the $3 \rightarrow 4'$, $3'$, and $2'$ transitions, respectively. A down-shift in the relative strength of the amplitude is evident from the narrow blue detuned side at the $3 \rightarrow 4'$ transition to the broad red detuned side at the $3 \rightarrow 2'$ transition because of the frequency shifts toward those transitions.

The amplitude of the total spectra across the $3 \rightarrow 4'$, $3'$, and $2'$ transitions decreases with decrease in F_e. The theoretical model that considers all neighboring hyperfine states as shown in the lower trace of Fig. 5.3 (b) and experiment as illustrated in the lower trace of Fig. 5.3 (c) agree well in terms of contrast and asymmetry. However, there are deviations in linewidths of approximately 100 kHz in both power regimes, which could be attributed to the effect of the magnetic field, imperfect alignment of laser beams, and other effects that are not included in the calculation.

5.4.2 $F_\mathrm{g} = 2 \rightarrow F_\mathrm{e} = 1, 2,$ and 3 Transitions

We further analyze the spectrally unresolved group of hyperfine transitions $2 \rightarrow 1', 2'$, and $3'$ of ^{85}Rb D2 lines instead of $F_g = 3$. Figure 5.4 presents a comparison of the calculated and measured spectra considering (a) pure two-level resonant transitions, i.e., $2 \rightarrow 1'$, $2 \rightarrow 2'$ and $2 \rightarrow 3'$, (b) a transition resonant at $2 \rightarrow 1'$ with neighboring hyperfine transitions of $2 \rightarrow 2'$ and $3'$, a transition resonant at $2 \rightarrow 2'$ with neighboring hyperfine transitions of $2 \rightarrow 1'$ and $3'$, a transition resonant at $2 \rightarrow 3'$ with neighboring hyperfine transitions of $2 \rightarrow 1'$ and $2'$, and (c) experimentally measured spectra for the resonant transitions of $2 \rightarrow 1'$, $2 \rightarrow 2'$ and $2 \rightarrow 3'$ for both weak (50 μW) and strong (4 mW) coupling powers as shown in the top and bottom traces, respectively.

The calculation for a DTLS in the low-power regime reproduces ultra-narrow EIT resonances, as expected, at $2 \rightarrow 1'$, $2 \rightarrow 2'$, and $2 \rightarrow 3'$ transitions, as shown in the upper traces of Fig. 2. The obtained EIT spectra differ relatively with the dominant EIT amplitude at the $2 \rightarrow 1'$ transition, as shown in the upper traces of Fig. 5.4 (a). The obtained linewidth resolutions of the EIT spectra are 90 kHz, 60 kHz, and 130 kHz at the $2 \rightarrow 3'$, $2'$, and $1'$ hyperfine transitions, respectively.

The EIT spectra calculated while considering all the neighboring states near the resonant state are similar in amplitude and contrast owing to the strong EIT amplitude at the $2 \rightarrow 1'$ neighboring hyperfine transition, illustrated in the upper traces of Fig. 5.4 (b). The trend in the measured spectra, as shown in Fig. 5.4 (c), exhibits a striking similarity in amplitude and a contrast that matches well with the calculation, as shown in Fig. 5.4 (b), while considering neighboring states. The resolved linewidth in the low coupling power regime is approximately 114 kHz across the $2 \rightarrow 3', 2'$, and $1'$ transitions using all the neighboring calculations,

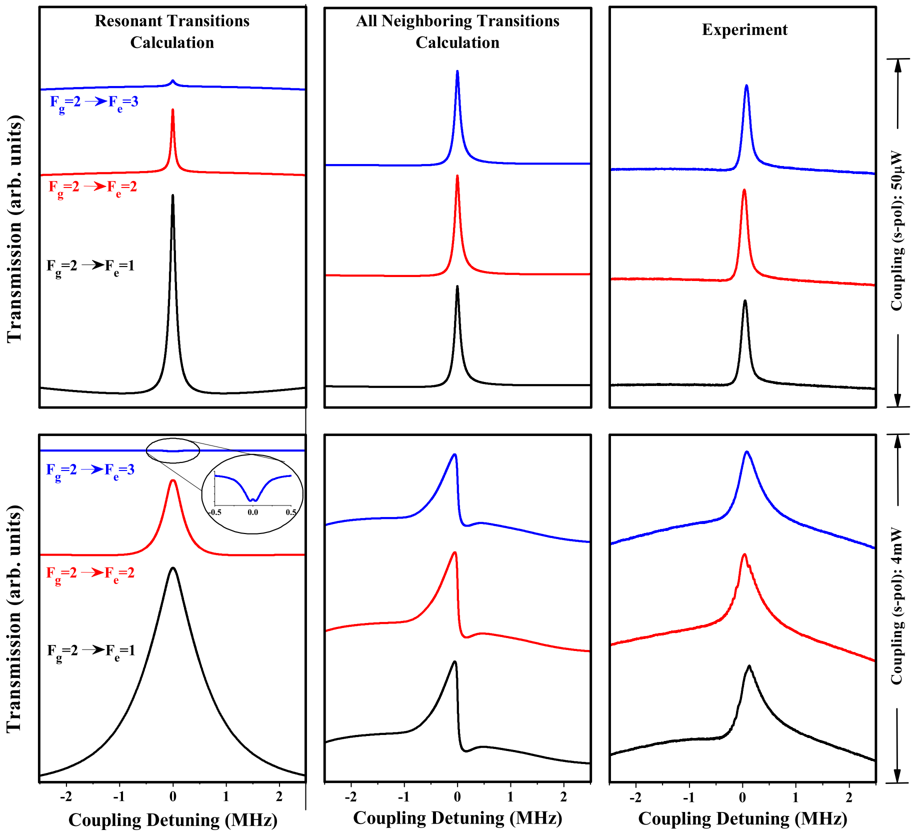

(a) (b) (c)

Figure 5.4: Comparison of calculated and measured spectra considering: (a) pure two-level resonant transitions, i.e., $3 \rightarrow 2'$, $3 \rightarrow 3'$ and $3 \rightarrow 4'$, (b) a transition resonant at $3 \rightarrow 2'$ with neighboring hyperfine transitions of $3 \rightarrow 3'$ and $4'$, transition resonant at $3 \rightarrow 3'$ with neighboring transitions of $3 \rightarrow 2'$ and $4'$, transition resonant at $3 \rightarrow 4'$ with neighboring transitions of $3 \rightarrow 2'$ and $3'$, and (c) experimentally measured spectra for resonant transitions $3 \rightarrow 2'$, $3 \rightarrow 3'$ and $3 \rightarrow 4'$.

as shown in Fig. 5.4 (b); the resolved linewidths in the experiment, as presented in Fig. 5.4 (c), are 157 kHz, 158 kHz, and 163 kHz at the $2 \rightarrow 3', 2'$, and $1'$ transitions, respectively.

In the intense coupling power regime, as shown in the lower traces of Fig. 5.4, the calculation that considers the resonant states shows an increase in amplitudes and linewidths of the obtained spectra at the $2 \rightarrow 1'$ and $2 \rightarrow 2'$ hyperfine transitions. However, in violation of condition (iii) of Lezama's necessary EIA conditions, a weak-amplitude EIA with a linewidth resolution of 285 kHz is obtained at the $2 \rightarrow 3'$ hyperfine transition, as highlighted in the inset image of in the lower traces of Fig. 5.4 (a).

Asymmetric EIT spectra of relatively similar amplitudes and linewidth resolutions are obtained owing to the contributions of all the neighboring hyperfine states with the resonant transition, as shown in the lower traces of Fig. 5.4 (b), which matches well with the trend of the measured spectra, shown in the lower traces of Fig. 5.4 (c). However, the experimentally measured spectra at higher powers could not reflect the fine contrast compared to the calculation with all the neighboring transitions shown in the lower traces of Fig. 5.4 (b). The resolved linewidths are 388 kHz, 407 kHz, and 435 kHz (441 kHz, 418 kHz, and 479 kHz) when using all the neighboring calculations (experiment).

The sign-inverting anomalies present at open transitions $3 \rightarrow 3'$ and $3 \rightarrow 2'$ in the previous cases, as shown in Figs. 5.3 (b) and 5.3 (c), are not relevant to the $2 \rightarrow 1', 2'$, and $3'$ group of spectrally resolved transitions as the EIT resonances at the $2 \rightarrow 3', 2'$, and $1'$ transitions are expected. Instead, anomalies in the relative strength of the amplitudes and linewidths at $2 \rightarrow 3', 2'$, and $1'$ are evident in the calculation on considering all the neighboring transitions and in the experiment, as shown in the lower traces of Figs. 5.4 (b) and 5.4 (c), respectively.

From both cases of $F_g = 2$ and 3, we observe that the power ratios between the coupling and probe beams, the excited state's openness, and the effects of neighboring states due to Doppler broadening are crucial factors in enhancing or reducing coherence effects for transformation between EIA and EIT.

5.5 Outlook

In this chapter, we solved the optical Bloch equations with and without neighboring hyperfine states for all hyperfine transitions of the ^{85}Rb D2 lines both in weak- and strong-coupling-power regimes while considering the Doppler effect in an ordinary vapor cell, wherein the calculated spectra matched well with the observed spectra. Theoretical models based on time-dependent density matrix equations of a degenerate (a) two-level (resonant transitions) and (b) multilevel system including all neighboring hyperfine transitions are considered for calculating coherence effects such as EIT and EIA using thermal averaging over the Doppler profile. EITs without neighboring effects in the case of open $3 \rightarrow 2'$ and $3'$, i.e., a DTLS that violates Lezama's EIA conditions, transforms into genuine and symmetric EIAs owing to a strong $3 \rightarrow 4'$ EIA line with Doppler broadening in the weak coupling and probe power regime. Previously, these EIAs at open transitions have not been explained theoretically and observed experimentally in the case of ^{85}Rb D2 lines, while asymmetric and split EIAs are observed from calculated weak EITs in a DTLS in a weak probe and strong-coupling-power regime. The reported [49, 50, 53, 55, 57–59] EIA resonances without clear quantitative explanations for open systems of D1 lines of ^{85}Rb and ^{87}Rb that violate conditions (ii) and (iii) of Lezama's EIA conditions are merely enhanced absorption phenomena governed by a strong coupling power. These are different from the EIAs observed and explained in the same transition configuration of $F_e = F_g - 1$ and F_g observed in this work using weak coupling-probe powers.

The EITs without neighboring effects in the DTLS in the case of $2 \rightarrow 1'$ ($2 \rightarrow 2'$) remain in the EITs owing to the $2 \rightarrow 2'$ ($2 \rightarrow 1'$) EIT line with the Doppler broadening in the weak probe and strong-coupling-power regime, while weak EIAs at $2 \rightarrow 3'$ in the weak probe and strong-coupling-power regime, which violates Lezama's EIA conditions because of openness, transform into EITs. Lezama's EIA conditions in the cycling case of $3 \rightarrow 4'$ with $F_g < F_e$ are also confirmed in intense coupling and weak probe regimes. With the comparisons of the calculated absorption profiles between a DTLS without neighboring states and all levels with neighboring states, the power ratio between the probe and coupling beams, openness of the excited state, and effects of neighboring states due to Doppler broadening are crucial factors for enhancing or reducing coherence effects for transformations between EIA and EIT.

Chapter 6

Control of EIA and EIT Transformations

6.1 Overview

In this chapter, we demonstrate the effective control of the inescapable dominance of neighboring hyperfine state transitions at ^{87,85}Rb atomic systems that are unresolved under Doppler broadening. Polarization configuration of coupling and probe fields results in the observation of complementary electromagnetically induced absorption (EIA) and electromagnetically induced transparency (EIT) resonances irrespective of closed or open degenerate systems. The dominance of open $F_g = 2 \rightarrow F_e = 2$ ($F_g = 3 \rightarrow F_e = 2$) D2 transitions in the case of linear parallel polarization of coupling and probe fields in low power regime results in the observation of EITs at neighboring closed $F_g = 2 \rightarrow F_e = 3$ ($F_g = 3 \rightarrow F_e = 4$) transitions that are, otherwise dominant transitions considering linear orthogonal and both parallel and orthogonal circular polarization cases resulting in EIAs at open $F_g = 2 \rightarrow F_e = 1$ and 2 ($F_g = 3 \rightarrow F_e = 2$ and 3) D2 transitions of ^{87}Rb (^{85}Rb), respectively. Theoretical calculations considering Doppler broadening effects with neighboring hyperfine states in Optical Bloch equations explain the experimental spectra well. We also calculate the limiting coefficients of ellipticity and energy level separation to determine the type of (EIT/EIA) resonance at ^{87,85}Rb D2 lines.

6.2 Theoretical calculation

Theoretical model developed in Chap. 5 Sec. 5.2 is extended to consider the coefficients of electric field components of coupling and probe beam specific to the polarization configuration. Hence, the interaction Hamiltonian presented in Eq. 5.2.3 Sec. 5.2 for $F_g = 3 \rightarrow F_e = 2, 3,$ and 4 of ^{85}Rb D2 transition is updated for

$F_g = 2 \rightarrow F_e = 1, 2$, and 3 of ^{87}Rb D2 transition given as

$$\begin{aligned} H_i &= \frac{\hbar}{2}\Omega_p e^{-i\delta_d t} \sum_{q=-1}^{1} \sum_{F_e=1}^{3} \sum_{m=-2}^{2} a_q C_{3,m}^{F_e,m+q} \left|F_e, m+q\right\rangle \left\langle F_g, m\right| \\ &\quad + \frac{\hbar}{2}\Omega_c \sum_{F_e=1}^{3} \sum_{m=-2}^{2} b_q C_{3,m}^{F_e,m} \left|F_e, m\right\rangle \left\langle F_g, m\right| + \text{h.c.}, \end{aligned} \tag{6.2.1}$$

where $F_g = 2$, $a_{\pm 1} = \mp 1/\sqrt{2}$, $a_0 = 0$, and $b_{\pm 1} = \mp 1/\sqrt{2}$, $a_0 = 0$ are the coefficient of the electric field of the probe (coupling) beam in the spherical bases, respectively and h.c. denotes Hermitian conjugate.

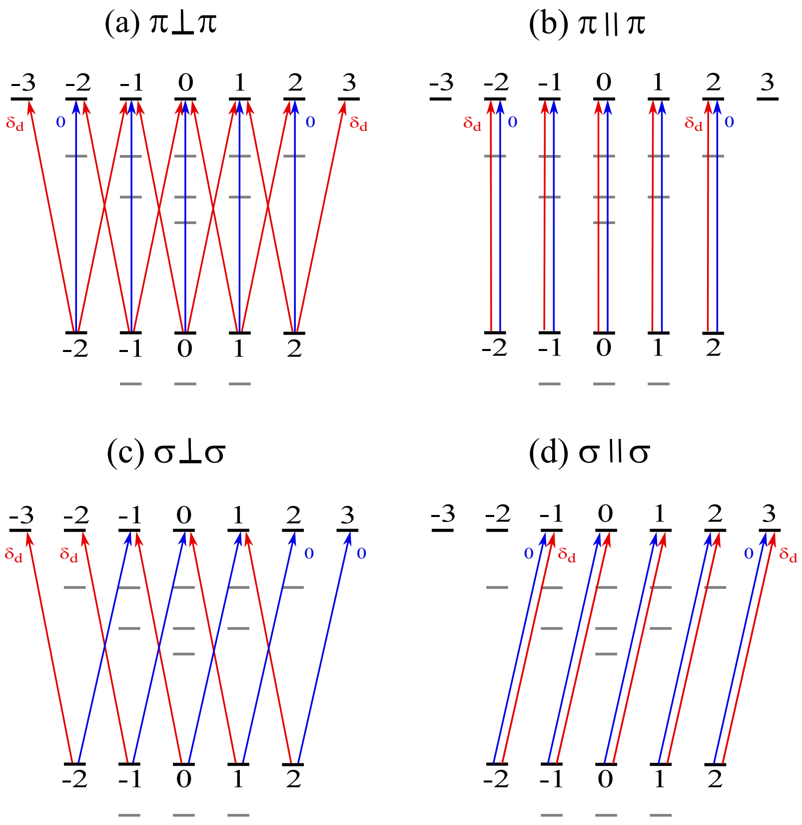

Figure 6.1: Level schemes considered in case of $F_g = 2 \rightarrow F_e = 3$ transition with two coupling and probe beams in (a) linear orthogonal ($\pi \perp \pi$), (b) Linear parallel ($\pi \| \pi$), (c) circular orthogonal ($\sigma \perp \sigma$), and (d) circular parallel ($\sigma \| \sigma$) polarization configuration, where "0" (blue lines) and "δ_d" (red lines) imply the transitions excited by the coupling and probe beams, respectively. The excitations for the $F_g = 2 \rightarrow F_e = 1$ and 2 transitions are not shown to avoid confusion.

Figure 6.1 shows the level schemes considered for the four polarization cases, where (a) linear orthogonal ($\pi\perp\pi$), (b) Linear parallel ($\pi\|\pi$), (c) circular orthogonal ($\sigma\perp\sigma$), and (d) circular parallel ($\sigma\|\sigma$) polarization configuration, where "0" (blue lines) and "δ_d" (red lines) imply the transitions excited by the coupling and probe beams, respectively. Considering the circular orthogonal polarization of coupling and probe beams ($\sigma\perp\sigma$) as shown in Fig. 6.1(c), coefficient of the electric field a_q (b_q) in Eq. 6.2.1 can be calculated as

$$\begin{aligned} a_+ &= -\frac{1}{2}(1+\sin 2\varepsilon)-\frac{i}{2}(\cos 2\varepsilon), \\ b_- &= +\frac{1}{2}(1-\sin 2\varepsilon)+\frac{i}{2}(\cos 2\varepsilon) \end{aligned}$$

where ε is the angle between the incident field vector and the optic axis of QWP.

6.3 Experimental Setup

A schematic diagram of the experimental setup is shown in Fig. 6.2. Coupling and probe beam is generated using a single tunable external cavity diode laser (DLPro, Toptica Inc.). Saturation absorption spectroscopy (SAS) setup is utilized to lock the desired $5S_{1/2} \rightarrow 5P_{3/2}$ transition of ^{87}Rb and ^{85}Rb D2 hyperfine line. A half-wave plate (HWP) and a polarizing beam splitter (PBS-1) are combined to separate and maintain 50 μW-15 μW power ratio between the coupling and probe beam intensities, respectively.

Effective scanning detuning (Δ) of the coupling beam is obtained by transmitting it through two acoustic optic modulators (AOMs) in a single-pass configuration. Both coupling and probe beams are expanded by five times to obtain a uniform intensity across a 4-mm diameter. Desired polarization configuration of coupling and probe beams is controlled by a combination of HWP and quarter-wave plates (QWP), and a beam splitter (BS) is used to overlap the co-propagating coupling and probe beams upon a vapor cell. An intersection angle of ~ 0.1 mrad is maintained to separate the probe beam at the photodetector (PD).

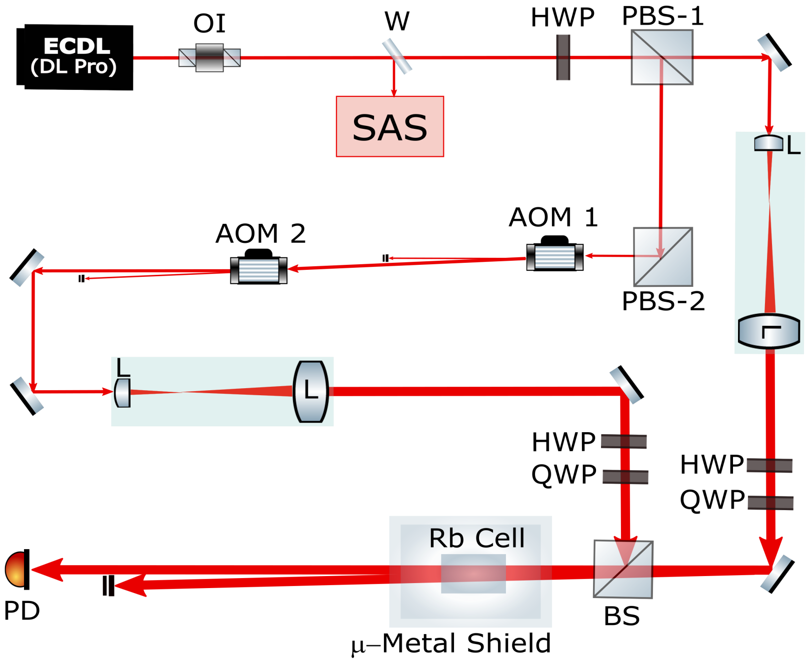

Figure 6.2: Schematic of the experimental setup. Component symbols: OI: optical isolator; W: window; SAS: saturation absorption spectroscopy; HWP: half-wave plate; PBS: polarizing beam splitter; QWP: quarter-wave plate; L: lens; PD: photodiode; AOM: acousto-optic modulator.

The experiments are performed at room temperature with ^{87}Rb and ^{85}Rb atoms confined in a reference vapor cell with the natural isotope ratio of Rb, which is 27.85% ^{87}Rb and 72.15% ^{85}Rb. The vapor cell is shielded with five layers of μ-metal sheets to remove the effect of stray and earth's magnetic fields inside the cell.

6.4 Results and Discussion

Spectrally resolved group of $F_g = 2 \rightarrow F_e = 1,2,3$ and $F_g = 3 \rightarrow F_e = 2,3,4$ transitions of ^{87}Rb and ^{85}Rb D2 lines respectively are measured and calculated with respect to coupling and probe polarizations in low coupling-probe (50 μW-15 μW) power ratio regime. Henceforth, simplified notations are used for the transitions: i.e. $F_g = 2 \rightarrow F_e = 3$ transition is expressed as $2 \rightarrow 3'$ were primed (unprimed) integer represents the angular quantum number of ground (excited) state. The results are analyzed according to the polarization configuration of coupling and probe fields presented in four subsections: i.e. (A) linear orthogonal ($\pi \perp \pi$), (B) linear Parallel ($\pi \| \pi$), (C) circular orthogonal ($\sigma \perp \sigma$), and (D) circular parallel ($\sigma \| \sigma$) case for ^{87}Rb and ^{85}Rb D2 lines, respectively in Figs. 6.3 to 6.6.

In each of the Figs. 6.3 to 6.6, top traces presented horizontally as (a-c) are for spectra at $2 \rightarrow 1'$, $2 \rightarrow 2'$, and $2' \rightarrow 3'$ transitions of ^{87}Rb D2 lines. While, bottom traces presented as (d-f) are for spectra at $3 \rightarrow 2'$, $3 \rightarrow 3'$ and $3 \rightarrow 4'$ transitions of ^{85}Rb D2 lines. Comparison of the theoretical calculation considering only resonant transitions are presented vertically in Figs. (a,d), calculation considering resonant transition with inclusion of all neighboring transitions are presented in (b,e), and the measured experimental results are presented in (c,f).

6.4.1 Linear Orthogonal ($\pi \perp \pi$)

Comparison of calculated and measured spectra of ^{87}Rb D2 lines in linear orthogonal ($\pi \perp \pi$) configuration of coupling and probe laser fields is shown in top traces of Fig. 6.3 considering: (a) pure DTLS with resonant transitions on i.e. $2 \rightarrow 1'$, $2 \rightarrow 2'$ and $2 \rightarrow 3'$, (b) considering transition resonant on $2 \rightarrow 1'$ with neighboring hyperfine transitions of $2 \rightarrow 2'$ and $3'$, transition resonant on $2 \rightarrow 2'$ with neighboring transitions of $2 \rightarrow 1'$ and $3'$, and transition resonant on $2 \rightarrow 3'$ with neighboring transitions of $2 \rightarrow 1'$ and $2'$, and (c) experimentally measured spectra for the resonant transitions $2 \rightarrow 1'$, $2 \rightarrow 2'$ and $2 \rightarrow 3'$.

Relatively strong EIA amplitude with ultra narrow linewidth resolution of 45 kHz is obtained at $2 \rightarrow 3'$ closed transition considering pure DTLS calculation that satisfies all necessary EIA conditions [2] as shown in the top trace of Fig. 6.3(a). In the case of closed transitions $2 \rightarrow 1'$ and $2 \rightarrow 2'$ weak amplitude EITs with the linewidths 54 kHz and 70 kHz, respectively are obtained. Spectra obtained by considering all neighboring states near the resonant $2 \rightarrow 1'$, $2 \rightarrow 2'$ and $2 \rightarrow 3'$ show EIAs due to the dominant $2 \rightarrow 3'$ closed transition as shown in Fig.

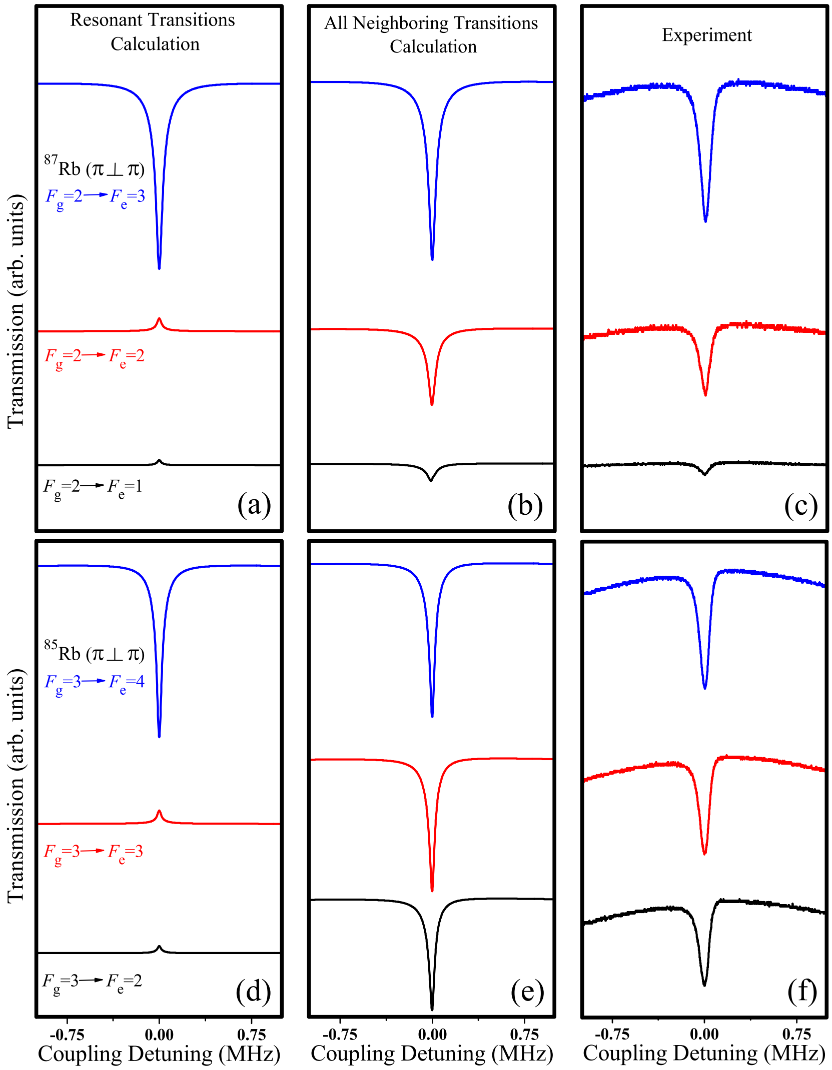

Figure 6.3: Comparison of calculated and measured spectra in case of linear orthogonal configuration of coupling and probe laser fields. Spectra resolved for $F_g = 2 \rightarrow F_e = 1,2,3$ of ^{87}Rb are shown in top traces (a-c) and spectra resolved for $F_g = 3 \rightarrow F_e = 2,3,4$ of^{85}Rb D2 lines are shown in bottom traces (d-f). Calculation considering a pure DTLS with resonant transitions only e.g $2 \rightarrow 3'$ and $3 \rightarrow 4'$ shown vertically in (a,d), respectively, calculation considering all neighboring hyperfine transitions near the resonant transition e.g transition resonant on $2 \rightarrow 3'$ with neighboring transitions of $2 \rightarrow 1'$ and $2'$ (b,e), and experimentally measured spectra for the resonant transitions only e.g $2 \rightarrow 3'$ and $3 \rightarrow 4'$ (c,f).

6.3(b), which strikingly show similar trends with the experimentally measured spectra shown in Fig. 6.3(c).

Relative amplitude of EIAs show a decreasing trend with decreasing excited state angular quantum number F_e both in calculation considering all neighboring states and the experiment. The observed difference in amplitude is due to energy difference between $2 \rightarrow 1'$ and $2 \rightarrow 2'$ excited state hyperfine levels that are 426.59 MHz and 266.65 MHz apart $2 \rightarrow 3'$ closed transition. The linewidths obtained are 77 kHz, 80 kHz, and 90 kHz (84 kHz, 91 kHz, and 96 kHz) at $2 \rightarrow 1'$, $2 \rightarrow 2'$ and $2 \rightarrow 3'$ transitions in case of all neighboring calculation (Fig. 6.3(b)) and experiment (Fig. 6.3(c)), respectively

Comparison of calculated and measured spectra of ^{85}Rb D2 lines in linear orthogonal configuration of coupling and probe laser fields is shown in bottom traces of Fig. 6.3 considering: (d) pure DTLS with resonant transitions on i.e. $3 \rightarrow 2'$, $3 \rightarrow 3'$ and $3 \rightarrow 4'$, (e) considering transition resonant on $3 \rightarrow 2'$ with neighboring hyperfine transitions of $3 \rightarrow 3'$ and $4'$, transition resonant on $3 \rightarrow 3'$ with neighboring transitions of $3 \rightarrow 2'$ and $4'$, transition resonant on $3 \rightarrow 4'$ with neighboring transitions of $3 \rightarrow 2'$ and $3'$, and (f) experimentally measured spectra for the resonant transitions $3 \rightarrow 2'$, $3 \rightarrow 3'$ and $3 \rightarrow 4'$.

Similar trends are obtained in analogy to the compared spectra at $2 \rightarrow 1'$, $2'$, and $3'$ of ^{87}Rb D2 lines shown in Fig. 6.3 (a-c). Figure 6.3(d) shows pure DTLS calculation, as expected strong amplitude EIA at $3 \rightarrow 4'$ closed transition and EITs at $3 \rightarrow 2'$ and $3 \rightarrow 3'$ open transitions are resolved with linewidth of 59 kHz, 48 kHz and 42 kHz, respectively. However, calculated spectra considering all neighboring states near the resonant transitions $3 \rightarrow 2'$, $3'$, and $4'$ of ^{85}Rb D2 lines and experiment show relatively similar trends in amplitudes of EIAs as shown in Figs. 6.3(e) and 6.3(f). Small decrease in amplitude is obtained with decreasing angular quantum number of excited states compared to the case of $2 \rightarrow 1'$, $2'$, and $3'$ of ^{87}Rb D2 lines given in Figs. 6.3(b) and 6.3(c) . This can be explained due to higher transition strength at $3 \rightarrow 4'$ closed transition in case of ^{85}Rb D2 lines and smaller energy difference between excited-state hyperfine levels $3 \rightarrow 2'$ and $3'$ that are 184 MHz and 120.6 MHz apart $3 \rightarrow 4'$ closed transition, respectively.

6.4.2 Linear Parallel ($\pi||\pi$)

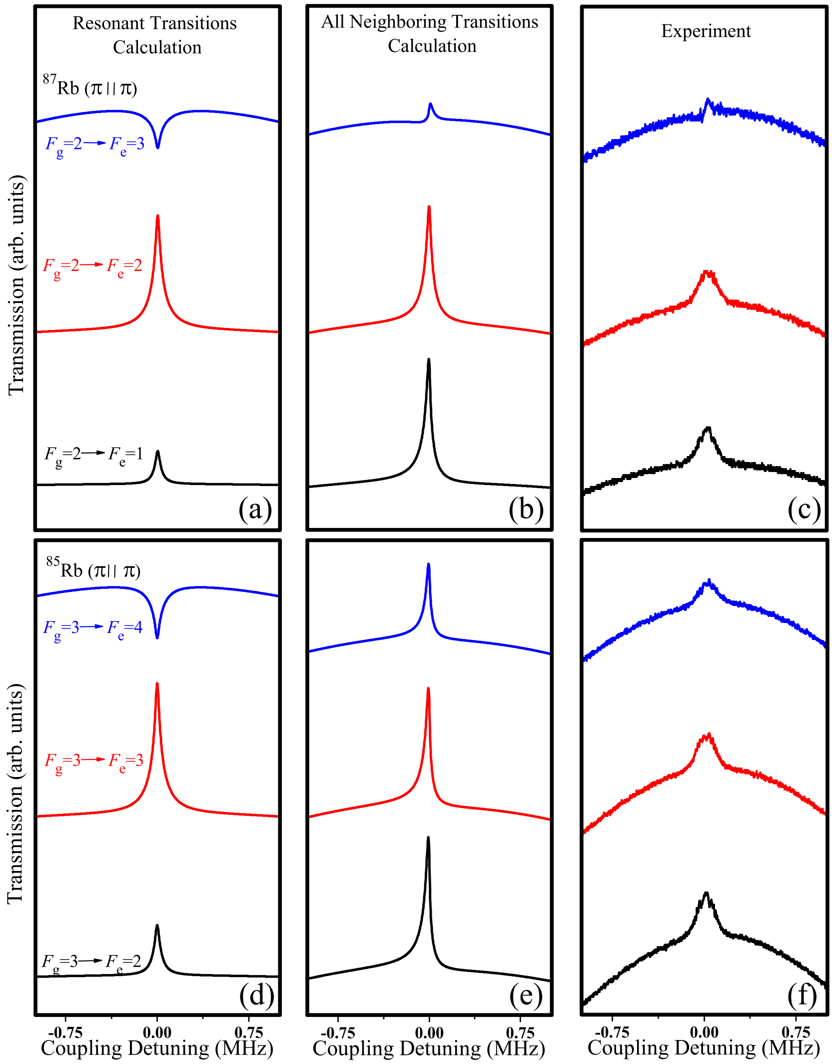

Figure 6.4: Comparison of calculated and measured spectra in case of linear parallel ($\pi||\pi$) configuration of coupling and probe laser fields. Spectra resolved for $F_g = 2 \rightarrow F_e = 1,2,3$ of ^{87}Rb are shown in top traces (a-c) and spectra resolved for $F_g = 3 \rightarrow F_e = 2,3,4$ of^{85}Rb D2 lines are shown in bottom traces (d-f). Calculation considering a pure DTLS with resonant transitions only e.g $2 \rightarrow 3'$ and $3 \rightarrow 4'$ shown vertically in (a,d), respectively, calculation considering all neighboring hyperfine transitions near the resonant transition e.g transition resonant on $2 \rightarrow 3'$ with neighboring transitions of $2 \rightarrow 1'$ and $2'$ (b,e), and experimentally measured spectra for the resonant transitions only e.g $2 \rightarrow 3'$ and $3 \rightarrow 4'$ (c,f).

Comparison of calculated and measured spectra of ^{87}Rb D2 lines with linear parallel coupling and probe configuration is shown in Fig. 6.4 considering: (a) pure DTLS with resonant transitions on i.e. $2 \to 1'$, $2 \to 2'$ and $2 \to 3'$, (b) considering transition resonant on $2 \to 1'$ with neighboring hyperfine transitions of $2 \to 2'$ and $3'$, transition resonant on $2 \to 2'$ with neighboring transitions of $2 \to 1'$ and $3'$, transition resonant on $2 \to 3'$ with neighboring transitions of $2 \to 1'$ and $2'$, and (c) experimentally measured spectra for the resonant transitions $2 \to 1'$, $2 \to 2'$ and $2 \to 3'$.

Allowed transitions in the linear parallel configuration of coupling and probe laser fields result in separate two-levels systems that effectively decouple necessary N-type coherences. In addition, $m = \pm 3$ hyperfine states are transparent to coupling and probe fields. Thus, spectra obtained considering a pure DTLS predicts a weak amplitude of EIA with 80 kHz linewidth at $2 \to 3'$ closed transition compared to a strong EIT peak with 79 kHz linewidth at $2 \to 2'$ open transition as shown in the top and the middle trace of Fig. 6.4(a), respectively. This strong amplitude EIT at $2 \to 2'$ open transition dominates the spectra obtained considering all neighboring states calculation and resonant measurements in the experiment at $2 \to 1'$, $2 \to 2'$ and $2 \to 3'$ transitions shown in Figs. 6.4(b) and 6.4(c). Weak and asymmetric EIT peak with linewidth resolution of 50 kHz (75 kHz) at $2 \to 3'$ closed transition, while strong amplitude EITs with linewidths of 58 kHz and 68 kHz (171 kHz and 188 kHz) at $2 \to 1'$ and $2 \to 2'$ open transitions are obtained considering all neighboring states calculation (experiment).

Spectra calculated considering all neighboring states model predicts the strongest EIT amplitude at $2 \to 1'$ transition although in pure DTLS calculation EIT at $2 \to 2'$ open transition is dominant as shown in bottom and middle trace of Figs. 6.4(b) and 6.4(a), respectively. This increase in amplitude of EIT at $2 \to 1'$ open transition can be explained as a result of strong influence of EIT at $2 \to 2'$ open transition, while EIA at neighboring $2 \to 3'$ closed transition weakly contributes to obtained EIT at $2 \to 2'$ open transition.

Comparison of calculated and measured spectra of ^{85}Rb D2 lines with linear parallel coupling and probe configuration is shown in Fig. 6.4 considering: (d) pure DTLS with resonant transitions on i.e. $3 \rightarrow 2$, $3 \rightarrow 3'$ and $3 \rightarrow 4'$), (e) considering transition resonant on $3 \rightarrow 2'$ with neighboring hyperfine transitions of $3 \rightarrow 3'$ and $4'$, transition resonant on $3 \rightarrow 3'$ with neighboring transitions of $3 \rightarrow 2'$ and $4'$, transition resonant on $3 \rightarrow 4'$ with neighboring transitions of $3 \rightarrow 2'$ and $3'$, and (f) experimentally measured spectra for the resonant transitions $3 \rightarrow 2'$, $3 \rightarrow 3'$ and $3 \rightarrow 4'$.

Trends in the spectra obtained at $3 \rightarrow 2'$, $3 \rightarrow 3'$ and $3 \rightarrow 4'$ transitions of ^{85}Rb D2 lines as shown in bottom traces (d-f) of Fig. 6.4 are quite similar to the ^{87}Rb D2 lines presented in top traces (a-c) of Fig. 6.4. However, an increase in the amplitude of EIT at $3 \rightarrow 4'$ closed transition is observed due to small energy splitting between excited-states hyperfine levels. Considering pure DTLS calculation EIA spectra at $3 \rightarrow 4'$ closed transition is resolved with linewidth of 84 kHz, while EITs at $3 \rightarrow 3'$ and $3 \rightarrow 2'$ are resolved with 74 kHz and 67 kHz linewidths, respectively as shown in Fig. 6.4(d). Spectra obtained considering all neighboring states calculation (experiment) are resolved with a linewidth of 59 kHz, 61 kHz, and 50 kHz (180 kHz, 192 kHz, and 167 kHz) EITs. Comparatively, small amplitudes and large linewidths of the EITs are measured in the experimental spectra due to possible leakage of coupling laser at the detector and polarization impurity of the fields.

6.4.3 Circular Orthogonal ($\sigma \perp \sigma$)

Comparison of calculated and measured spectra of ^{87}Rb D2 lines with circular orthogonal coupling and probe configuration is shown in top traces of Fig. 6.5 considering: (a) pure DTLS with resonant transitions on i.e. $2 \rightarrow 1'$, $2 \rightarrow 2'$ and $2 \rightarrow 3'$, (b) considering transition resonant on $2 \rightarrow 1'$ with neighboring hyperfine transitions of $2 \rightarrow 2'$ and $3'$, transition resonant on $2 \rightarrow 2'$ with neighboring transitions of $2 \rightarrow 1'$ and $3'$, transition resonant on $2 \rightarrow 3'$ with neighboring transitions of $2 \rightarrow 1'$ and $2'$, and (c) experimentally measured spectra for the resonant transitions $2 \rightarrow 1'$, $2 \rightarrow 2'$ and $2 \rightarrow 3'$.

In a pure DTLS calculation, obtained spectra at $2 \rightarrow 3'$ closed transition shows

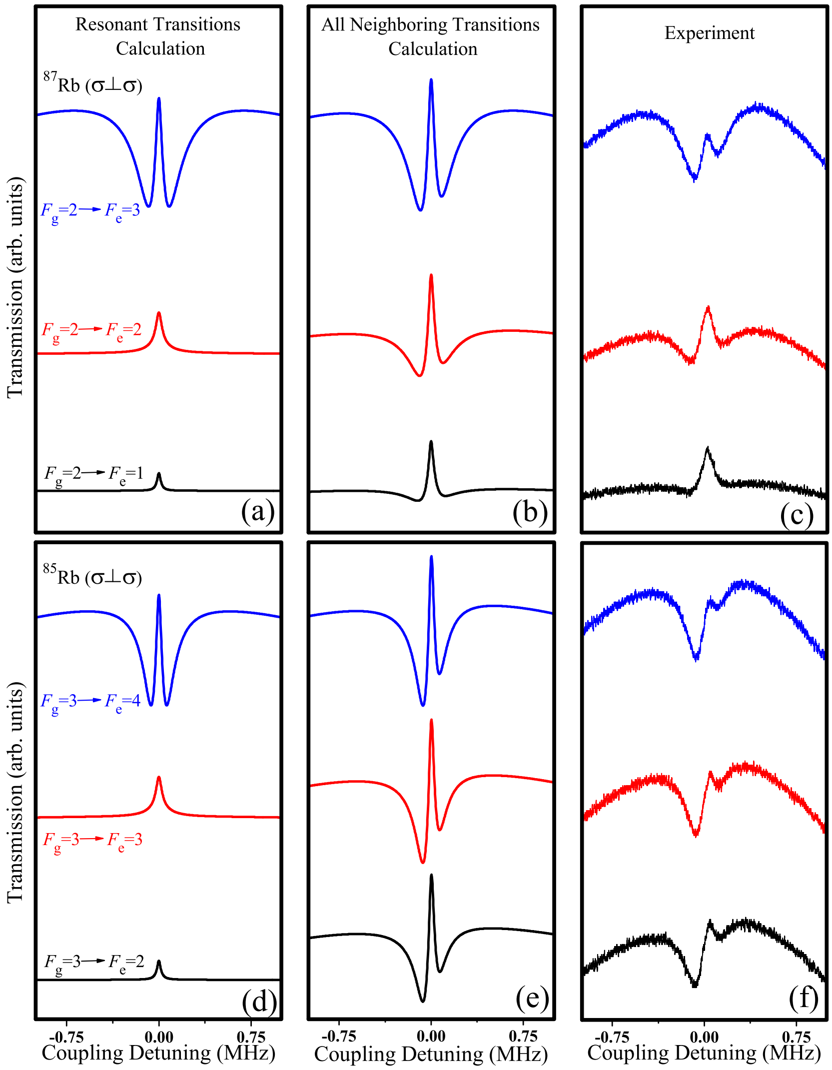

Figure 6.5: Comparison of calculated and measured spectra in case of circular orthogonal ($\sigma \perp \sigma$) configuration of coupling and probe laser fields. Spectra resolved for $F_g = 2 \rightarrow F_e = 1,2,3$ of ^{87}Rb are shown in top traces (a-c) and spectra resolved for $F_g = 3 \rightarrow F_e = 2,3,4$ of^{85}Rb D2 lines are shown in bottom traces (d-f). Calculation considering a pure DTLS with resonant transitions only e.g $2 \rightarrow 3'$ and $3 \rightarrow 4'$ shown vertically in (a,d), respectively, calculation considering all neighboring hyperfine transitions near the resonant transition e.g transition resonant on $2 \rightarrow 3'$ with neighboring transitions of $2 \rightarrow 1'$ and $2'$ (b,e), and experimentally measured spectra for the resonant transitions only e.g $2 \rightarrow 3'$ and $3 \rightarrow 4'$ (c,f).

a strong EIA amplitude with a broad linewidth of 406 kHz, which splits at the center into two broad dips resulting in a narrow EIT like the peak of 58 kHz linewidth as shown in Fig. 6.5(a). The contribution of negative and positive atomic velocities in the case of orthogonal polarizations results in two identically separated EIA signals at the center of the spectra after Doppler averaging [28]. However, the split in the case of circular orthogonal polarization is observed at low coupling power due to transfer of coherence that is different from the linear orthogonal polarization case where splitting appears near the saturation of excited state due to power broadening [73]. Relatively weak amplitude EITs with linewidths 66 kHz and 42 kHz are obtained at $2 \rightarrow 1'$ and $2 \rightarrow 2'$ open transitions respectively as shown in the lower traces of Fig. 6.5(a). While spectra calculated considering all neighboring states and experimentally measured show split and asymmetric EIAs at $2 \rightarrow 2'$ open transition, due to the strong influence of the dominant $2 \rightarrow 3'$ closed transition shown in the top and middle traces of Figs. 6.5(b) and 6.5(c), respectively. However, spectra at $2 \rightarrow 1'$ open transition show weak EIA amplitude asymmetrically split at center with linewidth resolutions of 53 kHz (103 kHz) considering all neighboring calculations (experiments) shown in bottom traces of Figs. 6.5(b) and 6.5(c).

Comparison of calculated and measured spectra of ^{85}Rb D2 lines with circular orthogonal coupling and probe configuration is shown in botom traces of Fig. 6.5 considering: (d) pure DTLS with resonant transitions on i.e. $3 \rightarrow 2'$, $3 \rightarrow 3'$ and $3 \rightarrow 4'$, (e) considering transition resonant on $3 \rightarrow 2'$ with neighboring hyperfine transitions of $3 \rightarrow 3'$ and $4'$, transition resonant on $3 \rightarrow 3'$ with neighboring transitions of $3 \rightarrow 2'$ and $4'$, transition resonant on $3 \rightarrow 4'$ with neighboring transitions of $3 \rightarrow 2'$ and $3'$, and (f) experimentally measured spectra for the resonant transitions $3 \rightarrow 2'$, $3 \rightarrow 3'$ and $3 \rightarrow 4'$.

Obtained spectral profiles at ^{85}Rb D2 lines shown in Fig. 6.5 (d-f) are similar to presented case of ^{87}Rb D2 lines in Fig. 6.5 (a-c), symmetric spectra with relatively strong amplitude of EIA profile at $3 \rightarrow 4'$ closed transition of ^{85}Rb D2 line and EITs at $3 \rightarrow 2'$ and $3 \rightarrow 3'$ open transitions are obtained as shown in Fig. 6.5(d), considering pure DTLS calculation. Linewidth resolution of the broad EIA is 293 kHz with the resolved center split of 41 kHz in linewidth at $3 \rightarrow 4'$ closed transition. While, EITs at $3 \rightarrow 2'$ and $3 \rightarrow 3'$ open transitions are resolved with 65 kHz and 39 kHz linewidth. Spectra obtained considering all neighboring states calculation and experiment show similar asymmetric and splitted EIA profiles at all resonant $3 \rightarrow 2'$, $3 \rightarrow 3'$ and $3 \rightarrow 4'$ hyperfine transitions as shown in Figs. 6.5(e) and 6.5(f), respectively. However, amplitudes of the EIAs obtained in case of ^{85}Rb D2 lines shown in Figs. 6.5(e) and 6.5(f) are approximately equal due to close excited state hyperfine levels in comparison to ^{87}Rb D2 lines as presented in Figs. 6.5(b) and 6.5(c) considering all neighboring calculation and experiment, respectively.

6.4.4 Circular Parallel ($\sigma \| \sigma$)

Comparison of calculated and measured spectra of ^{87}Rb D2 lines with circular parallel coupling and probe configuration is shown in Fig. 6.6 considering: (a) pure DTLS with resonant transitions on i.e. $2 \rightarrow 1'$, $2 \rightarrow 2'$ and $2 \rightarrow 3'$, (b) considering transition resonant on $2 \rightarrow 1'$ with neighboring hyperfine transitions of $2 \rightarrow 2'$ and 3, transition resonant on $2 \rightarrow 2'$ with neighboring transitions of $2 \rightarrow 1'$ and $3'$, transition resonant on $2 \rightarrow 3'$ with neighboring transitions of $2 \rightarrow 1'$ and $2'$, and (c) experimentally measured spectra for the resonant transitions $2 \rightarrow 1'$, $2 \rightarrow 2'$ and $2 \rightarrow 3'$.

Relatively strong EIA amplitude with narrow linewidth resolution of 58 kHz at $2 \rightarrow 3'$ closed transition and weak EITs with linewidths of 57 kHz and 73 kHz at $2 \rightarrow 1'$ and $2 \rightarrow$ ‘2 open transitions are obtained considering pure DTLS calculation as shown in Fig. 6.6(a). However, spectra obtained considering all neighboring transitions and experiment show striking similarity in the trends presented in Figs. 6.6(b) and 6.6(c). EIT at $2 \rightarrow 1'$ open transition while EIAs at $2 \rightarrow 2'$ open and $2 \rightarrow 3'$ closed transitions are resolved with linewidths of 69 kHz, 47 kHz, and 54 kHz (91 kHz, 41 kHz, and 117 kHz) considering all neighboring transitions calculation (experiment), respectively. Strong EIA amplitude due to same polarizations between coupling and probe fields result from transfer of population [29] producing coherences between the same magnetic sublevels at $2 \rightarrow 3'$ closed transition which dominates the near neighboring $2 \rightarrow 2'$ open tran-

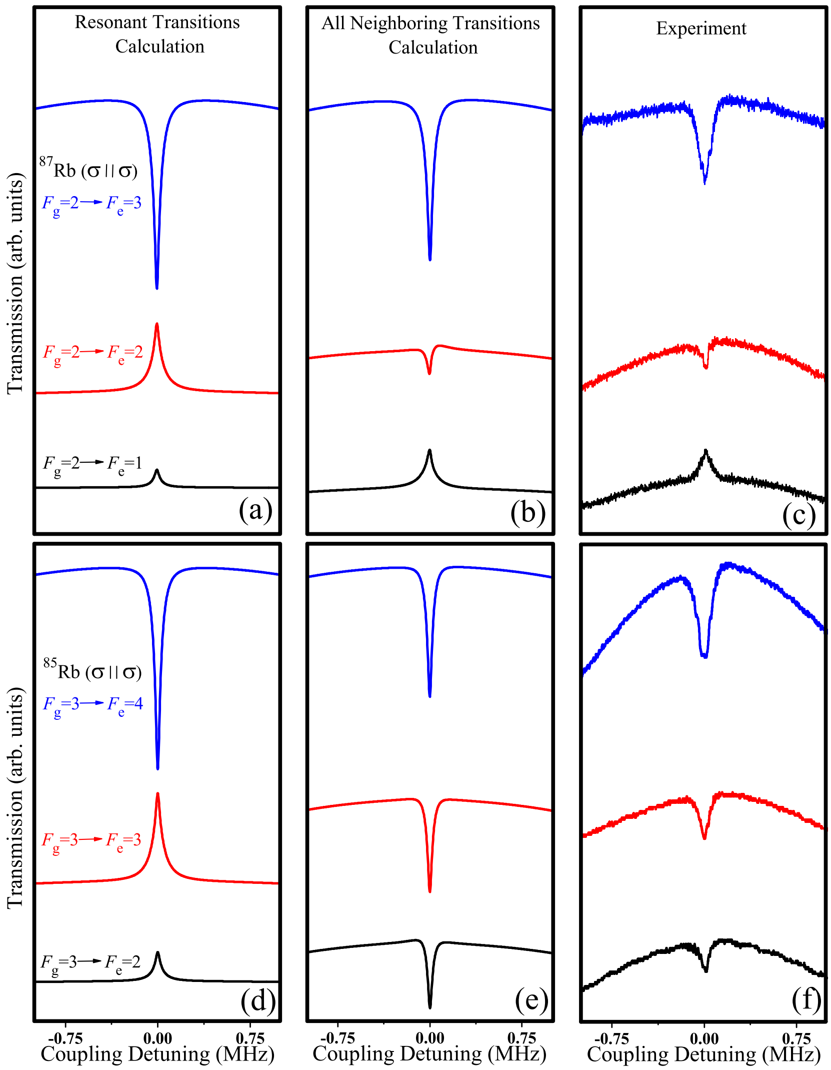

Figure 6.6: Comparison of calculated and measured spectra in case of circular parallel ($\sigma \| \sigma$) configuration of coupling and probe laser fields. Spectra resolved for $F_g = 2 \rightarrow F_e = 1,2,3$ of ^{87}Rb are shown in top traces (a-c) and spectra resolved for $F_g = 3 \rightarrow F_e = 2,3,4$ of^{85}Rb D2 lines are shown in bottom traces (d-f). Calculation considering a pure DTLS with resonant transitions only e.g $2 \rightarrow 3'$ and $3 \rightarrow 4'$ shown vertically in (a,d), respectively, calculation considering all neighboring hyperfine transitions near the resonant transition e.g transition resonant on $2 \rightarrow 3'$ with neighboring transitions of $2 \rightarrow 1'$ and $2'$ (b,e), and experimentally measured spectra for the resonant transitions only e.g $2 \rightarrow 3'$ and $3 \rightarrow 4'$ (c,f).

sition to transform into EIA shown in middle traces of Figs. 6.6(b) and 6.6(c), while $2 \rightarrow 1'$ open transition is effectively influenced by near neighboring $2 \rightarrow 2'$

open transition resulting in relatively strong amplitude of EIT as shown in bottom traces of Figs. 6.6(b) and 6.6(c) in comparison to the amplitude obtained considering pure DTLS as shown in bottom trace of Fig. 6.6(a).

Comparison of calculated and measured spectra of ^{85}Rb D2 lines with circular parallel coupling and probe configuration is shown in Fig. 6.6 considering: (d) pure DTLS with resonant transitions on i.e. $3 \rightarrow 2'$, $3 \rightarrow 3'$ and $3 \rightarrow 4'$, (e) considering transition resonant on $3 \rightarrow 2'$ with neighboring hyperfine transitions of $3 \rightarrow 3'$ and $4'$, transition resonant on $3 \rightarrow 3'$ with neighboring transitions of $3 \rightarrow 2'$ and $4'$, transition resonant on $3 \rightarrow 4'$ with neighboring transitions of $3 \rightarrow 2'$ and $3'$, and (f) experimentally measured spectra for the resonant transitions $3 \rightarrow 2'$, $3 \rightarrow 3'$ and $3 \rightarrow 4'$.

In pure DTLS calculation shown in Fig. 6.6(d), strong amplitude EIA dip with 59 kHz linewidth at $3 \rightarrow 4'$ transition and EITs at $3 \rightarrow 2'$ and $3 \rightarrow 3'$ transition with 79 kHz and 69 kHz linewidths are well resolved as expected. Spectral features at $3 \rightarrow 2'$, $3 \rightarrow 3'$ and $3 \rightarrow 4'$ transitions of 85Rb D2 lines show similar trends to those calculated for ^{87}Rb D2 lines presented in Fig. 6.6(a). However, in comparison to obtained spectra at ^{87}Rb D2 lines calculation considering all neighboring states and experiment show EIAs at all the resonant $3 \rightarrow 2'$, $3 \rightarrow 3'$ and $3 \rightarrow 4'$ transitions of ^{85}Rb atoms due to strong Doppler overlapping between excited states hyperfine levels as shown in Figs. 6.6(e) and (f), respectively. EIAs are resolved with 49 kHz, 49 kHz, and 50 kHz (62 kHz, 85 kHz, 137 kHz) linewidths considering all neighboring states calculation (experiment) at $3 \rightarrow 2$, $3 \rightarrow 3$ and $3 \rightarrow 4$ transitions, respectively.

Dominating upper ground states closed transitions $2 \rightarrow 3'$ and $3 \rightarrow 4'$ of ^{87}Rb and ^{85}Rb D2 lines effectively control the sign of observed EIA or EIT resonance. Spectra calculated and measured for lower ground states hyperfine transitions i.e. open transitions $1 \rightarrow 0'$, $1'$, $2'$ and $2 \rightarrow 1'$, $2'$, $3'$ of ^{87}Rb and ^{85}Rb D2 lines (not presented in this report) show relatively similar amplitudes of EITs considering all neighboring transitions calculation and experiment. However, no evident change in signs of the EIT resonances are noted at $1 \rightarrow 0'$, $1'$, $2'$ and $2 \rightarrow 1'$, $2'$, $3'$ of ^{87}Rb and ^{85}Rb D2 lines due to openness of these transitions utilizing the experimental parameters and polarization configurations of the coupling and probe fields presented in this report.

In comparison between spectra obtained at ^{87}Rb and ^{85}Rb D2 lines, the model predicts the spectral profile differences due to the difference between excited states energy level splitting, which in the case of ^{87}Rb D2 lines is relatively large, although it does not exceed the effective Doppler overlapping in practical test systems. However, the weak amplitude of the experimentally measured spectra mainly results in the linewidth difference compared to all neighboring transitions calculations. Factors such as the small overlapping angle between coupling and probe fields, considerable maintained distance (~ 20 m) of the detector to separate the fields at detection, and polarization impurity of the fields may be the reason for the loss in the amplitude of the probe field signal.

6.5 Outlook

Observed EIAs at both closed and open transitions can be transformed to EITs and vice versa by controlling the polarization of coupling and probe beams. Effect of neighboring hyperfine levels with the inclusion of Doppler broadening effects in coupling-probe spectroscopy configuration dominates the calculated spectra using Optical Bloch equations for ^{87}Rb and ^{85}Rb atomic systems that are unresolved under Doppler broadening effects. Closed transitions $2 \rightarrow 3$ and $3 \rightarrow 4$ effectively control the sign of observed EIA or EIT resonance at $2 \rightarrow 1$, 2 and $3 \rightarrow 2$, 3 of ^{87}Rb and ^{85}Rb D2 lines.

Spectral trends such as asymmetry and sign of the EIT/EIA resonances obtained experimentally and calculated considering all neighboring hyperfine levels match quite well in all the presented polarization configurations of coupling and probe fields. Observed EIAs at all transitions of $2 \rightarrow 1, 2, 3$ and $3 \rightarrow 2, 3, 4$ of ^{87}Rb and ^{85}Rb D2 lines respectively transform to EITs utilizing linear parallel polarization of coupling and probe laser beams in low power ratio regime.

Strongly coupled degenerate states forming N-type systems at closed dominant transitions $2 \rightarrow 3$ and $3 \rightarrow 4$ in orthogonal linear, and in both orthogonal and parallel circular configurations of coupling-probe fields effectively enhance the EIA strengths influencing the neighboring open transitions 2 → 1, 2 and 3 → 2, 3 of ^{87}Rb and ^{85}Rb D2 lines, respectively. However, in linear parallel configuration separated two-level systems at 2 → 3 and 3 → 4 closed transitions and decoupled $m = \pm 3$ and ± 4 degenerate states effectively reduce the coherence strength effectively reducing EIAs. Although, open transitions 2 → 1, 2 and 3 → 2, 3 remain strongly coupled thus resulting in higher strength of EITs influencing the expected EIAs at neighboring closed transitions 2 → 3 and 3 → 4 to transform into EITs.

Chapter 7

Project Outlook

7.1 Overview

In this chapter, we highlight some of the conclusions drawn based on the results analysis, limitations of our proposed works, and future directions.

7.2 Conclusions

This thesis investigated degenerate two-level atomic systems (DTLS) utilizing coupling-probe spectroscopy configuration. Specifically, we focused on sub-natural width electromagnetically induced absorption (EIA) and electromagnetically induced transparency (EIT) resonances associated with the coherent interaction of coupling and probe light fields. The main results concern the experimental measurement of rubidium (Rb) D2 transition lines confined in an atomic vapor cell at room temperature ($20^{\circ}C$). Essential spectroscopic features depending on physical observables such as probe absorption, three-photon interaction (3PI), five-photon interaction (5PI), Doppler broadening, and effects due to neighboring hyperfine states are analyzed theoretically as a function of physical parameters such as external magnetic field, coupling and probe power ratio, polarization, and atomic level characteristics to obtain the coherent control of these resonances in the realistic test systems.

We present experimental and theoretical verification of the higher-order multiphoton oscillation frequency mixing dependence on the choice of quantum axis selected as the propagation direction of co-propagating coupling and probe laser beams and coupling powers. Distinct calculated spectral differences between 3PI and 5PI owing to variations in the magnetic field and coupling power are confirmed for the first time. Experimentally observed coherent EIA spectra at the $F_g = 3 \rightarrow F_e = 4$ transition of ^{85}Rb atoms using two orthogonal linear polarizations of intense coupling and weak probe beams as a function of static longitudinal magnetic field and coupling powers match very well with those calculated by considering 5PI in Optical Bloch equations (OBEs). Subsequently, asymmetries in the observed spectra are explained due to close neighboring hyperfine transitions calculated from five-photon interactions considering the off-resonant $F_g = 3 \rightarrow F_e = 2, 3$ transitions.

Furthermore, we show that in unresolved real atomic systems such as ^{85,87}Rb neighboring hyperfine states play an inevitable role in enhancement or reduction of the coherent effects due to Doppler broadening, which results in the transformation between EIA and EIT. Optical Bloch equations (OBEs) in the challenging case of ^{85}Rb D2 transition that involves the Doppler broadening effects are solved with and without considering neighboring hyperfine states near the degenerate two-level system (DLTS). Comparisons based on the calculated absorption profiles of a DTLS with and without considering neighboring states depending on the coupling and probe power ratios clearly verify the experimentally measured EIA(EIT) at the open $F_g = 3 \rightarrow F_e = 2$ and 3 transitions (open $F_g = 2 \rightarrow F_e = 2$ and 3 transitions) due to the strong closed $F_g = 3 \rightarrow F_e = 4$ transition line (strong closed $F_g = 2 \rightarrow F_e = 1$ transition line).

Finally, we present theoretical and experimental verification of a simple method to coherently control the EIA and EIT resonances in unresolved ^{85,87}Rb atomic systems by controlling the polarization of coupling and probe laser fields in coupling-probe spectroscopy configuration. Observed EIAs at both closed and open transitions of ^{87}Rb and ^{85}Rb D2 lines atomic systems can be transformed to EITs and vice versa by controlling the polarization of coupling and probe beams in the low coupling-probe power regime. The transformations are determined to be the effect of neighboring hyperfine levels by comparing the measured and theoretically calculated spectra considering Doppler broadening effects with the inclusion of neighboring hyperfine levels in Optical Bloch equations.

Genuine, coherent spectral shapes are observed with a single external cavity diode laser combined with two acousto-optic modulators. The spectral resolution is limited because of the decoherence rate between Zeeman sublevels in the ground state from transit-time relaxation.

7.3 Limitations

Limitations of the presented study are as follow::

1. In theory, we assume overlapping between copropagating coupling and probe beams to be collinear. However, an intersection angle of ~ 0.1 mrad between coupling and probe beams in the experiment is imperative to eliminate the coupling beam at the detector. Consequently, considerable distance with the detector is maintained to separate the probe, resulting in loss of probe amplitude.

2. In the experiment, scanning AOM determines the coupling-probe spectral resolution and is therefore limited to the center frequency bandwidth of AOM, which in our setup has a typical value of 30 kHz.

3. The dynamics of atom-light interactions presented here exhibit new features specific to the interaction schemes of a degenerate multilevel atomic system.

7.4 Future directions

In the future, we would like to enhance the existing study in the following directions.

1. We will pursue the study of detailed higher photon interaction effects exceeding 5PI on the coherent EIA spectra concerning the intensity of the coupling laser field.

2. Recently, it is shown in [78] that laser phase noise due to the independent coupling-probe laser sources hinders in observation of narrow spectral lines of polarization rotation spectra. An experiment is planned to observe such narrow signals using an AOM and laser with a narrow linewidth. Additionally, density matrix equations considering neighboring hyperfine states can clarify the observed spectra due to Doppler broadening effects.

Bibliography

[1] A. M. Akulshin, S. Barreiro, and A. Lezama. Electromagnetically induced absorption and transparency due to resonant two-field excitation of quasidegenerate levels in rb vapor. *Phys. Rev. A*, 57:2996–3002, Apr 1998. doi: 10.1103/PhysRevA.57.2996. URL https://link.aps.org/doi/10.1103/PhysRevA.57.2996.

[2] A. Lezama, S. Barreiro, and A. M. Akulshin. Electromagnetically induced absorption. *Phys. Rev. A*, 59:4732–4735, Jun 1999. doi: 10.1103/PhysRevA.59.4732. URL https://link.aps.org/doi/10.1103/PhysRevA.59.4732.

[3] S. E. Harris, J. E. Field, and A. Imamoğlu. Nonlinear optical processes using electromagnetically induced transparency. *Phys. Rev. Lett.*, 64:1107–1110, Mar 1990. doi: 10.1103/PhysRevLett.64.1107. URL https://link.aps.org/doi/10.1103/PhysRevLett.64.1107.

[4] K.J. Boller, A. Imamoğlu, and S. E. Harris. Observation of electromagnetically induced transparency. *Phys. Rev. Lett.*, 66:2593–2596, May 1991. doi: 10.1103/PhysRevLett.66.2593. URL https://link.aps.org/doi/10.1103/PhysRevLett.66.2593.

[5] Paul Mandel. Lasing without inversion: A useful concept? *Contemporary Physics*, 34(5):235–246, 1993. doi: 10.1080/00107519308222084. URL https://doi.org/10.1080/00107519308222084.

[6] M. D. Lukin, S. F. Yelin, M. Fleischhauer, and M. O. Scully. Quantum interference effects induced by interacting dark resonances. *Phys. Rev. A*, 60:3225–3228, Oct 1999. doi: 10.1103/PhysRevA.60.3225. URL https://link.aps.org/doi/10.1103/PhysRevA.60.3225.

[7] Marlan O. Scully and Michael Fleischhauer. High-sensitivity magnetometer based on index-enhanced media. *Phys. Rev. Lett.*, 69:1360–1363, Aug 1992. doi: 10.1103/PhysRevLett.69.1360. URL https://link.aps.org/doi/10.1103/PhysRevLett.69.1360.

[8] Michael Fleischhauer and Marlan O. Scully. Quantum sensitivity limits of an optical magnetometer based on atomic phase coherence. *Phys. Rev. A*, 49:1973–1986, Mar 1994. doi: 10.1103/PhysRevA.49.1973. URL `https://link.aps.org/doi/10.1103/PhysRevA.49.1973`.

[9] Dmitry Budker and Michael Romalis. Optical magnetometry. *Nature Physics*, 3:227–234, April 2007. doi: 10.1038/nphys566. URL `https://doi.org/10.1038/nphys566`.

[10] M. Fleischhauer, C. H. Keitel, M. O. Scully, Chang Su, B. T. Ulrich, and Shi-Yao Zhu. Resonantly enhanced refractive index without absorption via atomic coherence. *Phys. Rev. A*, 46:1468–1487, Aug 1992. doi: 10.1103/PhysRevA.46.1468. URL `https://link.aps.org/doi/10.1103/PhysRevA.46.1468`.

[11] S. E. Harris and Y. Yamamoto. Photon switching by quantum interference. *Phys. Rev. Lett.*, 81:3611–3614, Oct 1998. doi: 10.1103/PhysRevLett.81.3611. URL `https://link.aps.org/doi/10.1103/PhysRevLett.81.3611`.

[12] Lene Vestergaard Hau, S. E. Harris, Zachary Dutton, and Cyrus H. Behroozi. Light speed reduction to 17 metres per second in an ultracold atomic gas. *Nature*, 397:594–598, Feb 1999. doi: 10.1038/17561. URL `https://doi.org/10.1038/17561`.

[13] Byoung S. Ham and Philip R. Hemmer. Coherence switching in a four-level system: Quantum switching. *Phys. Rev. Lett.*, 84:4080–4083, May 2000. doi: 10.1103/PhysRevLett.84.4080. URL `https://link.aps.org/doi/10.1103/PhysRevLett.84.4080`.

[14] M. Fleischhauer and M. D. Lukin. Dark-state polaritons in electromagnetically induced transparency. *Phys. Rev. Lett.*, 84:5094–5097, May 2000. doi: 10.1103/PhysRevLett.84.5094. URL `https://link.aps.org/doi/10.1103/PhysRevLett.84.5094`.

[15] Chien Liu, Zachary Dutton, Cyrus H. Behroozi, and Lene Vestergaard Hau. Dark-state polaritons in electromagnetically induced transparency. *Nature*, 409:490–493, Jan 2001. doi: 10.1038/35054017. URL `https://doi.org/10.1038/35054017`.

[16] D. F. Phillips, A. Fleischhauer, A. Mair, R. L. Walsworth, and M. D. Lukin. Storage of light in atomic vapor. *Phys. Rev. Lett.*, 86:783–786, Jan 2001. doi: 10.1103/PhysRevLett.86.783. URL `https://link.aps.org/doi/10.1103/PhysRevLett.86.783`.

[17] A. S. Zibrov, A. B. Matsko, O. Kocharovskaya, Y. V. Rostovtsev, G. R. Welch, and M. O. Scully. Transporting and time reversing light via atomic coherence. *Phys. Rev. Lett.*, 88:103601, Feb 2002. doi: 10.1103/PhysRevLett.88.103601. URL `https://link.aps.org/doi/10.1103/PhysRevLett.88.103601`.

[18] C. H. van der Wal, M. D. Eisaman, A. André, R. L. Walsworth, D. F. Phillips, A. S. Zibrov, and M. D. Lukin. Atomic memory for correlated photon states. *Science*, 301(5630):196–200, 2003. ISSN 0036-8075. doi: 10.1126/science.1085946. URL `https://science.sciencemag.org/content/301/5630/196`.

[19] R. G. Beausoleil, W. J. Munro, D. A. Rodrigues, and T. P. Spiller. Applications of electromagnetically induced transparency to quantum information processing. *Journal of Modern Optics*, 51(16-18):2441–2448, 2004. doi: 10.1080/09500340408231802. URL `https://doi.org/10.1080/09500340408231802`.

[20] Dong Ya-Bin, Gao Jiang-Rui, and Dong You-Er. Quantum coherent effects in multi-zeeman-sublevel atomic systems. 17(9):3306–3312, sep 2008. doi: 10.1088/1674-1056/17/9/027. URL `https://doi.org/10.1088/1674-1056/17/9/027`.

[21] Gyeong-Won Choi and Heung-Ryoul Noh. Sub-doppler DAVLL spectra of the D1 line of rubidium: a theoretical and experimental study. *Journal of Physics B: Atomic, Molecular and Optical Physics*, 48(11):115008, may 2015. doi: 10.1088/0953-4075/48/11/115008. URL `https://doi.org/10.1088/0953-4075/48/11/115008`.

[22] Yun-Wen Chen, Chung-Wei Lin, Ying-Cheng Chen, and Ite A. Yu. Quantization axes in coherent two-field spectroscopy. *J. Opt. Soc. Am. B*, 19(8):1917–1921, Aug 2002. doi: 10.1364/JOSAB.19.001917. URL `http://www.osapublishing.org/josab/abstract.cfm?URI=josab-19-8-1917`.

[23] A. D. Wilson-Gordon and H. Friedmann. Ultranarrow extraresonant antiholes in pump–probe spectroscopy induced by inelastic collisions. *Opt. Lett.*, 14(8):390–392, Apr 1989. doi: 10.1364/OL.14.000390. URL `http://www.osapublishing.org/ol/abstract.cfm?URI=ol-14-8-390`.

[24] L. Margalit, M. Rosenbluh, and A. D. Wilson-Gordon. Degenerate two-level system in the presence of a transverse magnetic field. *Phys. Rev. A*, 87:033808, Mar 2013. doi: 10.1103/PhysRevA.87.033808. URL `https://link.aps.org/doi/10.1103/PhysRevA.87.033808`.

[25] A. Lezama, S. Barreiro, A. Lipsich, and A. M. Akulshin. Coherent two-field spectroscopy of degenerate two-level systems. *Phys. Rev. A*, 61:013801, Dec 1999. doi: 10.1103/PhysRevA.61.013801. URL `https://link.aps.org/doi/10.1103/PhysRevA.61.013801`.

[26] C. Goren, A. D. Wilson-Gordon, M. Rosenbluh, and H. Friedmann. Electromagnetically induced absorption due to transfer of coherence and to transfer of population. *Phys. Rev. A*, 67:033807, Mar 2003. doi: 10.1103/PhysRevA.67.033807. URL `https://link.aps.org/doi/10.1103/PhysRevA.67.033807`.

[27] C. Goren, A. D. Wilson-Gordon, M. Rosenbluh, and H. Friedmann. Switching from positive to negative dispersion in transparent degenerate and near-degenerate systems. *Phys. Rev. A*, 68:043818, Oct 2003. doi: 10.1103/PhysRevA.68.043818. URL https://link.aps.org/doi/10.1103/PhysRevA.68.043818.

[28] Hafeez-Ur Rehman, Muhammad Adnan, Heung-Ryoul Noh, and Jin-Tae Kim. Spectral features of electromagnetically induced absorption in ^{85}Rb atoms. *Journal of Physics B: Atomic, Molecular and Optical Physics*, 48(11):115502, apr 2015. doi: 10.1088/0953-4075/48/11/115502. URL https://doi.org/10.1088/0953-4075/48/11/115502.

[29] C. Goren, A. D. Wilson-Gordon, M. Rosenbluh, and H. Friedmann. Atomic four-level N systems. *Phys. Rev. A*, 69:053818, May 2004. doi: 10.1103/PhysRevA.69.053818. URL https://link.aps.org/doi/10.1103/PhysRevA.69.053818.

[30] Ying Gu, Qingqing Sun, and Qihuang Gong. Quantum coherence in a degenerate two-level atomic ensemble for a transition $F_e = 0 \leftrightarrow F_g = 1$. *Phys. Rev. A*, 67:063809, Jun 2003. doi: 10.1103/PhysRevA.67.063809. URL https://link.aps.org/doi/10.1103/PhysRevA.67.063809.

[31] Asaf Eilam and A. D. Wilson-Gordon. Temporal optical memory based on coherent population and two-photon coherence oscillations. *Phys. Rev. A*, 98:013808, Jul 2018. doi: 10.1103/PhysRevA.98.013808. URL https://link.aps.org/doi/10.1103/PhysRevA.98.013808.

[32] Hafeez Ur Rehman, Muhammad Qureshi Mohsin, Heung-Ryoul Noh, and Jin-Tae Kim. Electromagnetically induced absorption due to transfer of coherence and coherence population oscillation for the $F_g = 3 \rightarrow F_e = 4$ transition in ^{85}Rb atoms. *Optics Communications*, 381(C):127–134, 2016. doi: 10.1016/j.optcom.2016.06.063.

URL https://www.sciencedirect.com/science/article/abs/pii/S0030401816305594.

[33] Gyeong-Won Choi and Heung-Ryoul Noh. Line shapes in sub-doppler davll in the ^{87}Rb-D2 line. *Optics Communications*, 367:312–315, 2016. ISSN 0030-4018. doi: https://doi.org/10.1016/j.optcom.2016.01.073. URL https://www.sciencedirect.com/science/article/pii/S0030401816300736.

[34] A. Lipsich, S. Barreiro, A. M. Akulshin, and A. Lezama. Absorption spectra of driven degenerate two-level atomic systems. *Phys. Rev. A*, 61:053803, Apr 2000. doi: 10.1103/PhysRevA.61.053803. URL https://link.aps.org/doi/10.1103/PhysRevA.61.053803.

[35] J Fuchs, G J Duffy, W J Rowlands, A Lezama, P Hannaford, and A M Akulshin. Electromagnetically induced transparency and absorption due to optical and ground-state coherences in ^{6}Li. 40(6):1117–1129, mar 2007. doi: 10.1088/0953-4075/40/6/003. URL https://doi.org/10.1088/0953-4075/40/6/003.

[36] T. Zigdon, A. D. Wilson-Gordon, and H. Friedmann. Pump-probe spectroscopy in degenerate two-level atoms with arbitrarily strong fields. *Phys. Rev. A*, 77:033836, Mar 2008. doi: 10.1103/PhysRevA.77.033836. URL https://link.aps.org/doi/10.1103/PhysRevA.77.033836.

[37] T. Zigdon, A. D. Wilson-Gordon, and H. Friedmann. Absorption spectra for strong pump and probe in atomic beam of cesium atoms. *Phys. Rev. A*, 80:033825, Sep 2009. doi: 10.1103/PhysRevA.80.033825. URL https://link.aps.org/doi/10.1103/PhysRevA.80.033825.

[38] Heung-Ryoul Noh and Han Seb Moon. Calculated hanle transmission and absorption spectra of the ^{87}Rb D_1 line with residual magnetic field for arbitrarily polarized light. *Phys. Rev. A*, 82:033407, Sep 2010. doi:

10.1103/PhysRevA.82.033407. URL https://link.aps.org/doi/10.1103/PhysRevA.82.033407.

[39] Hong Cheng, Han-Mu Wang, Shan-Shan Zhang, Pei-Pei Xin, Jun Luo, and Hong-Ping Liu. Electromagnetically induced transparency of ^{87}Rb in a buffer gas cell with magnetic field. 50(9):095401, apr 2017. doi: 10.1088/1361-6455/aa6824. URL https://doi.org/10.1088/1361-6455/aa6824.

[40] A Sargsyan, D. Sarkisyan, Y. Pashayan-Leroy, C. Leroy, S. Cartaleva, A. D. Wilson-Gordon, and M. Auzinsh. Electromagnetically induced transparency resonances inverted in magnetic field. *Journal of Experimental and Theoretical Physics*, 121:966–975, Dec 2015. doi: 10.1134/S1063776115130142. URL https://doi.org/10.1134/S1063776115130142.

[41] R. Mirzoyan, A. Sargsyan, D. Sarkisyan, A. Wojciechowski, A. Stabrawa, and W. Gawlik. Eit resonance features in strong magnetic fields in rubidium atomic columns with length varying by 4 orders. *Optics and Spectroscopy*, 120:864–870, Jun 2016. doi: 10.1134/S0030400X16060151. URL https://doi.org/10.1134/S0030400X16060151.

[42] A. Sargsyan, D. Sarkisyan, L. Margalit, and A. D. Wilson-Gordon. Eit resonance features in strong magnetic fields in rubidium atomic columns with length varying by 4 orders. *Journal of Experimental and Theoretical Physics*, 122:1002–1007, Jun 2016. doi: 10.1134/S1063776116060194. URL https://doi.org/10.1134/S1063776116060194.

[43] Indra Hang Subba and Ajay Tripathi. Observation of electromagnetically induced absorption in ^{87}Rb D2 line in strong transverse magnetic field. 51(15):155001, jul 2018. doi: 10.1088/1361-6455/aacb6f. URL https://doi.org/10.1088/1361-6455/aacb6f.

[44] S. M. Iftiquar and Vasant Natarajan. Line narrowing of electromagnetically induced transparency in Rb with a longitudinal magnetic field. *Phys. Rev. A*, 79:013808, Jan 2009. doi: 10.1103/PhysRevA.79.013808. URL `https://link.aps.org/doi/10.1103/PhysRevA.79.013808`.

[45] L. Margalit, M. Rosenbluh, and A. D. Wilson-Gordon. Coherent-population-trapping transients induced by a modulated transverse magnetic field. *Phys. Rev. A*, 88:023827, Aug 2013. doi: 10.1103/PhysRevA.88.023827. URL `https://link.aps.org/doi/10.1103/PhysRevA.88.023827`.

[46] Y Dancheva, G Alzetta, S Cartaleva, M Taslakov, and Ch Andreeva. Coherent effects on the zeeman sublevels of hyperfine states in optical pumping of Rb by monomode diode laser. *Optics Communications*, 178(1):103–110, 2000. ISSN 0030-4018. doi: https://doi.org/10.1016/S0030-4018(00)00643-X. URL `https://www.sciencedirect.com/science/article/pii/S003040180000643X`.

[47] G Alzetta, S Cartaleva, Y Dancheva, Ch Andreeva, S Gozzini, L Botti, and A Rossi. Coherent effects on the zeeman sublevels of hyperfine states at the D_1 and D_2 lines of Rb. *Journal of Optics B: Quantum and Semiclassical Optics*, 3(3):181–188, may 2001. doi: 10.1088/1464-4266/3/3/317. URL `https://doi.org/10.1088/1464-4266/3/3/317`.

[48] H. Failache, P. Valente, G. Ban, V. Lorent, and A. Lezama. Inhibition of electromagnetically induced absorption due to excited-state decoherence in Rb vapor. *Phys. Rev. A*, 67:043810, Apr 2003. doi: 10.1103/PhysRevA.67.043810. URL `https://link.aps.org/doi/10.1103/PhysRevA.67.043810`.

[49] A.V. Papoyan, M. Auzinsh, and K. Bergmann. Nonlinear hanle effect in Cs vapor under strong laser excitation. *The European Physical Journal D - Atomic, Molecular, Optical and Plasma Physics*, 21:63–71, Oct

2002. ISSN 1434-6079. doi: 10.1140/epjd/e2002-00178-y. URL https://doi.org/10.1140/epjd/e2002-00178-y.

[50] Soo Kyoung Kim, Han Seb Moon, Kyoungdae Kim, and Jung Bog Kim. Observation of electromagnetically induced absorption in open systems regardless of angular momentum. *Phys. Rev. A*, 68:063813, Dec 2003. doi: 10.1103/PhysRevA.68.063813. URL https://link.aps.org/doi/10.1103/PhysRevA.68.063813.

[51] D. V. Brazhnikov, A. V. Taichenachev, A. M. Tumaikin, V. I. Yudin, I. I. Ryabtsev, and V. M. Entin. Effect of the polarization of counterpropagating light waves on nonlinear resonances of the electromagnetically induced transparency and absorption in the hanle configuration. *JETP Letters*, 91: 625–629, Jun 2010. ISSN 1090-6487. doi: 10.1134/S0021364010120039. URL https://doi.org/10.1134/S0021364010120039.

[52] E. G. Saprykin, A. A. Chernenko, and A. M. Shalagin. Polarization phenomena in the transparency and adsorption effects induced by the field of counterpropagating waves. *Journal of Experimental and Theoretical Physics*, 119:196–205, Aug 2014. ISSN 1090-6509. doi: 10.1134/S1063776114070140. URL https://doi.org/10.1134/S1063776114070140.

[53] Hsiang-Shun Chou and Jörg Evers. Dressed-atom multiphoton analysis of anomalous electromagnetically induced absorption. *Phys. Rev. Lett.*, 104: 213602, May 2010. doi: 10.1103/PhysRevLett.104.213602. URL https://link.aps.org/doi/10.1103/PhysRevLett.104.213602.

[54] A. S. Zibrov and A. B. Matsko. Induced absorption resonance on the open$F_g = 1 \rightarrow F_e = 2$ transition of the D_1 line of the ^{87}Rb atom. *Journal of Experimental and Theoretical Physics Letters*, 82:472–476, Oct 2005. ISSN 1090-6487. doi: 10.1134/1.2150864. URL https://doi.org/10.1134/1.2150864.

[55] Zhao Jian-Ming, Zhao Yan-Ting, Huang Tao, Xiao Lian-Tuan, and Jia Suo-Tang. Observation of EIA in closed and open caesium atomic system. *Chinese Physics*, 14(4):725–728, mar 2005. doi: 10.1088/1009-1963/14/4/015. URL `https://doi.org/10.1088/1009-1963/14/4/015`.

[56] M. Auzinsh, R. Ferber, F. Gahbauer, A. Jarmola, and L. Kalvans. F-resolved magneto-optical resonances in the D_1 excitation of cesium: Experiment and theory. *Phys. Rev. A*, 78:013417, Jul 2008. doi: 10.1103/PhysRevA.78.013417. URL `https://link.aps.org/doi/10.1103/PhysRevA.78.013417`.

[57] M. Auzinsh, R. Ferber, F. Gahbauer, A. Jarmola, and L. Kalvans. Nonlinear magneto-optical resonances at D_1 excitation of ^{85}Rb and ^{87}Rb for partially resolved hyperfine F levels. *Phys. Rev. A*, 79:053404, May 2009. doi: 10.1103/PhysRevA.79.053404. URL `https://link.aps.org/doi/10.1103/PhysRevA.79.053404`.

[58] M. Auzinsh, R. Ferber, F. Gahbauer, A. Jarmola, L. Kalvans, A. Papoyan, and D. Sarkisyan. Nonlinear magneto-optical resonances at D_1 excitation of ^{85}Rb and ^{87}Rb in an extremely thin cell. *Phys. Rev. A*, 81:033408, Mar 2010. doi: 10.1103/PhysRevA.81.033408. URL `https://link.aps.org/doi/10.1103/PhysRevA.81.033408`.

[59] M. Auzinsh, A. Berzins, R. Ferber, F. Gahbauer, L. Kalvans, A. Mozers, and D. Opalevs. Conversion of bright magneto-optical resonances into dark resonances at fixed laser frequency for D_2 excitation of atomic rubidium. *Phys. Rev. A*, 85:033418, Mar 2012. doi: 10.1103/PhysRevA.85.033418. URL `https://link.aps.org/doi/10.1103/PhysRevA.85.033418`.

[60] Raghwinder Singh Grewal and M Pattabiraman. Hanle electromagnetically induced absorption in open $F_g \rightarrow F_e F_g$ transitions of the ^{87}Rb D_2 line. *Journal of Physics B: Atomic, Molecular and Optical Physics*, 48(8):

085501, Mar 2015. doi: 10.1088/0953-4075/48/8/085501. URL https://doi.org/10.1088/0953-4075/48/8/085501.

[61] C. Andreeva, S. Cartaleva, Y. Dancheva, V. Biancalana, A. Burchianti, C. Marinelli, E. Mariotti, L. Moi, and K. Nasyrov. Coherent spectroscopy of degenerate two-level systems in Cs. *Phys. Rev. A*, 66:012502, Jul 2002. doi: 10.1103/PhysRevA.66.012502. URL https://link.aps.org/doi/10.1103/PhysRevA.66.012502.

[62] Michael Fleischhauer, Atac Imamoglu, and Jonathan P. Marangos. Electromagnetically induced transparency: Optics in coherent media. *Rev. Mod. Phys.*, 77:633–673, Jul 2005. doi: 10.1103/RevModPhys.77.633. URL https://link.aps.org/doi/10.1103/RevModPhys.77.633.

[63] Nibedita Ram, M. Pattabiraman, and C. Vijayan. Effect of ellipticity on hanle electromagnetically induced absorption and transparency resonances with longitudinal and transverse magnetic fields. *Phys. Rev. A*, 82:033417, Sep 2010. doi: 10.1103/PhysRevA.82.033417. URL https://link.aps.org/doi/10.1103/PhysRevA.82.033417.

[64] Ye Jin Yu, Hyun Jun Lee, In-Ho Bae, Heung-Ryoul Noh, and Han Seb Moon. Level-crossing absorption with narrow spectral width in Rb vapor with buffer gas. *Phys. Rev. A*, 81:023416, Feb 2010. doi: 10.1103/PhysRevA.81.023416. URL https://link.aps.org/doi/10.1103/PhysRevA.81.023416.

[65] Ravi, Harish, Bhattarai, Mangesh, Bharti, Vineet, and Natarajan, Vasant. Polarization-dependent tuning of the hanle effect in the ground state of Cs. *EPL*, 117(6):63002, 2017. doi: 10.1209/0295-5075/117/63002. URL https://doi.org/10.1209/0295-5075/117/63002.

[66] Z. D. Grujić, M. Mijailović, D. Arsenović, A. Kovačević, M. Nikolić, and B. M. Jelenković. Dark raman resonances due to ramsey interfer-

ence in vacuum vapor cells. *Phys. Rev. A*, 78:063816, Dec 2008. doi: 10.1103/PhysRevA.78.063816. URL `https://link.aps.org/doi/10.1103/PhysRevA.78.063816`.

[67] A. A. Zhukov, S. A. Zibrov, G. V. Romanov, Y. O. Dudin, V. V. Vassiliev, V. L. Velichansky, and V. P. Yakovlev. Electromagnetically induced absorption in a bichromatic laser field. *Phys. Rev. A*, 80:033830, Sep 2009. doi: 10.1103/PhysRevA.80.033830. URL `https://link.aps.org/doi/10.1103/PhysRevA.80.033830`.

[68] Nibedita Ram and M Pattabiraman. Sign reversal of hanle electromagnetically induced absorption with orthogonal circularly polarized optical fields. 43(24):245503, Nov 2010. doi: 10.1088/0953-4075/43/24/245503. URL `https://doi.org/10.1088/0953-4075/43/24/245503`.

[69] D. V. Brazhnikov, A. V. Taichenachev, and V. I. Yudin. Polarization method for controlling a sign of electromagnetically-induced transparency/absorption resonances. *Phys. Rev. A*, 63:315–325, Aug 2011. doi: 10.1140/epjd/e2011-20112-6. URL `https://doi.org/10.1140/epjd/e2011-20112-6`.

[70] Mangesh Bhattarai, Vineet Bharti, and Vasant Natarajan. Tuning of the hanle effect from EIT to EIA using spatially separated probe and control beams. *Scientific Reports*, 8:7525, May 2018. doi: 10.1038/s41598-018-25832-8. URL `https://doi.org/10.1038/s41598-018-25832-8`.

[71] K Kim, M Kwon, H D Park, H S Moon, H S Rawat, K An, and J B Kim. Electromagnetically induced absorption spectra depending on intensities and detunings of the coupling field in Cs vapour. 34(23):4801–4808, Nov 2001. doi: 10.1088/0953-4075/34/23/322. URL `https://doi.org/10.1088/0953-4075/34/23/322`.

[72] Silvia Gozzini, Andrea Fioretti, Alessandro Lucchesini, Luca Marmugi, Carmela Marinelli, Stoyan Tsvetkov, Sanka Gateva, and Stefka Cartaleva. Tunable and polarization-controlled high-contrast bright and dark coherent resonances in potassium. *Opt. Lett.*, 42(15):2930–2933, Aug 2017. doi: 10.1364/OL.42.002930. URL `http://www.osapublishing.org/ol/abstract.cfm?URI=ol-42-15-2930`.

[73] Zeeshan Ali Safdar Jadoon, Heung-Ryoul Noh, and Jin-Tae Kim. Multi-photon nonlinear frequency mixing effects on the coherent electromagnetically induced absorption spectra of ^{85}Rb atoms under a longitudinal magnetic field: Theory and experiment. *Phys. Rev. A*, 102:063714, Dec 2020. doi: 10.1103/PhysRevA.102.063714. URL `https://link.aps.org/doi/10.1103/PhysRevA.102.063714`.

[74] Heung-Ryoul Noh. Susceptibility for doppler-broadened two-level atoms in pump–probe spectroscopy: analytical solutions revisited. *J. Opt. Soc. Am. B*, 33(3):308–312, Mar 2016. doi: 10.1364/JOSAB.33.000308. URL `http://www.osapublishing.org/josab/abstract.cfm?URI=josab-33-3-308`.

[75] A. V. Taichenachev, A. M. Tumaikin, and V. I. Yudin. Electromagnetically induced absorption in a four-state system. *Phys. Rev. A*, 61:011802, Dec 1999. doi: 10.1103/PhysRevA.61.011802. URL `https://link.aps.org/doi/10.1103/PhysRevA.61.011802`.

[76] Boyd R. W. *Nonlinear Optics*. International series of monographs on physics. Academic, Noston, 1992.

[77] M. Fleischhauer and M. D. Lukin. Dark-state polaritons in electromagnetically induced transparency. *Phys. Rev. Lett.*, 84:5094–5097, May 2000. doi: 10.1103/PhysRevLett.84.5094. URL `https://link.aps.org/doi/10.1103/PhysRevLett.84.5094`.

[78] Geol Moon, Seung-Chul Yang, Jin-Tae Kim, and Heung-Ryoul Noh. Polarization rotation spectral profiles for the D2 line of ^{87}Rb atoms: theory and experiment. *Journal of Physics B: Atomic, Molecular and Optical Physics*, 52(22):225004, oct 2019. doi: 10.1088/1361-6455/ab4709. URL `https://doi.org/10.1088/1361-6455/ab4709`.

Acknowledgments

This thesis has been carried out at the Department of Photonic Engineering, Chosun University Korea(South), since spring 2017. Several people deserve thanks for their support and help. Therefore, it is my greatest pleasure to express my gratitude to them all in this acknowledgment.

First and foremost, my deepest gratitude to my supervisor, Prof. Jin-Tae Kim, without whom this thesis would not have been possible. I have been amazingly fortunate to have an advisor who taught me how to question thoughts and express ideas. His guidance and insight have been invaluable over the past few years. I am also grateful to Prof. Heung-Ryoul Noh for his valuable contributions to the project, innumerable enlightening discussions about physics, and proofreading this thesis. Indeed, without his collaboration, this thesis would not be what it is today.

Thanks to my office mates Aisar Ul Hassan and Jae-Gon Lee. Their friendship and banter have made the days spent in the office more enjoyable, particularly in the last few months while writing up. I would like to extend my thanks to the rest of Photonic Engineering Department. I am sure that the department's friendly atmosphere and genuine camaraderie directly influence its success.

My acknowledgments would not be complete without thanking the most important people in my life. To my late parents, immediate family—thank you for helping me achieve as much as I have done and for your constant encouragement in everything I do. Thank you for all of your love and support. I couldn't have done it without you.